Laboratory Studies of Atmospherically Important Gas-Phase Peroxy Radical Reactions

Thesis by

Lance E. Christensen

In partial fulfillment of the requirements

for the Degree of Doctor of Philosophy

California Institute of Technology

2002

Abstract

Peroxy radicals (HO_2, RO_2) are important intermediates in Earth's atmosphere. They are intermediates in the oxidation of alkanes and CO in combustion and atmospheric chemical processes. In earth's atmosphere, the rates of their self and cross reactions are often the dominant loss processes when NO_x concentrations fall below tens of pptv. These reactions have proven difficult to study in laboratory experiments, due to complex secondary chemistry and ambiguities in radical detection.

This thesis describes a new laser-photolysis apparatus to measure the rates of peroxy radical reactions under atmospheric conditions that employs simultaneous UV direct absorption and IR wavelength-modulation spectroscopy to detect the peroxy radicals. Prior kinetic measurements of gas-phase peroxy radical reactions have typically employed flash-photolysis methods coupled with detection of the radicals only by UV absorption spectroscopy. However, uncertainties can arise because several different species often contribute to the absorption signal. The IR channel provides an independent means of monitoring HO_2 radicals by detection of specific rovibrational transitions.

With this apparatus, the rates of the reactions $HO_2 + NO_2$, $HO_2 + CH_3O_2$, $CH_3O_2 + CH_3O_2$, and $HO_2 + HO_2$ were studied at temperatures from 219 K to 300 K. Our measurements have, in some cases, led to significant revision of previously accepted rate constants, mechanisms, or product yields, especially at conditions relevant to the upper atmosphere. The new rate coefficients for the $HO_2 + HO_2$ reaction are shown to account

for a long-standing discrepancy in modeled vs. observed hydrogen peroxide in the stratosphere.

A key finding has been the observation that many previous measurements of HO_2 reactions at low temperatures have suffered from problems due to complexation between HO_2 and methanol, a precursor used to generate HO_2. Direct kinetic evidence is presented for the formation of the $HO_2 \cdot CH_3OH$ complex; the rate coefficients, equilibrium constant, and enthalpy of reaction for $HO_2 + CH_3OH, \leftrightarrow HO_2 \cdot CH_3OH$ were measured. These results are the first direct study of the chaperone effect proposed to explain the enhancement of the observed rates of the HO_2 self-reaction by hydrogen-bonding species.

The effects of methanol enhancement on the $HO_2 + NO_2$, $HO_2 + CH_3O_2$, $CH_3O_2 + CH_3O_2$, and $HO_2 + HO_2$ reaction rates were measured. For the $HO_2 + NO_2$ reaction, overlapping, time-dependent signals in the UV due to the equilibrium between NO_2 and N_2O_4 were observed that may not have been properly accounted for in previous measurements. Other studies of NO_2 reactions conducted at temperatures below 250 K may be subject to similar errors. In the $CH_3O_2 + CH_3O_2$ reaction, detection of HO_2 products has raised questions concerning the product yields and reaction mechanisms.

Table of contents

List of Tables

List of Figures

Chapter 1: Measurements of the Rate Constant for $HO_2 + NO_2 + N_2 \rightarrow HO_2NO_2 + N_2$ Using Infrared Wavelength-Modulation Spectroscopy and UV-Visible Absorption Spectroscopy

1.1 Introduction

The reaction between HO_2 and NO_2 has been the subject of numerous laboratory studies[1-10] and proceeds as

$$HO_2 + NO_2 \xrightarrow{M} HO_2NO_2 \qquad (1)$$

From the upper troposphere through the middle stratosphere, the thermal lifetime of HO_2NO_2 is sufficiently long that reaction with OH is a significant loss process for HO_2NO_2. This establishes a NO_2 driven catalytic cycle that is an important sink for HO_x.[11]

$$HO_2 + NO_2 \xrightarrow{M} HO_2NO_2 \qquad (1)$$

$$OH + HO_2NO_2 \longrightarrow H_2O + NO_2 + O_2 \qquad (2)$$

$$OH + HO_2 \longrightarrow H_2O + O_2 \qquad (3)$$

Measurements of HO_2NO_2 from space[12] and balloon-borne[13] platforms have enabled researchers to test our understanding of atmospheric processes involving HO_2NO_2. Accurate measurements of k_1 are thus necessary to correctly describe the chemistry of this region of the atmosphere.

The most comprehensive studies of reaction (1) measured the time dependence of $[HO_2]$ with UV spectroscopy and utilized CH_3OH as a precursor for HO_2.[8-10] These studies have had the greatest influence on current recommendations.[14,15] In these previous studies, the rate of reaction (1) was measured under conditions where an appreciable fraction of HO_2 would be hydrogen-bonded to CH_3OH, namely low temperatures (< 273 K) and/or high $[CH_3OH]$. It has been shown[16,17] that CH_3OH can significantly enhance the observed rate of the reaction

$$HO_2 + HO_2 \xrightarrow[\text{ter-molecular}]{\text{bi-molecular}} H_2O_2 + O_2 \qquad (4)$$

under these conditions. A similar enhancement for reaction (1) might also be expected. This would suggest that the NASA recommended rates are too high at low temperatures.

This paper details kinetic studies of reaction (1) using simultaneous UV and IR detection. The effect of CH_3OH on reaction (1) was measured. Detection of HO_2 in the IR provided a method of measuring k_1 that avoided overlapping absorptions from several species, a problem associated with measurements in the UV. In addition, the use of heterodyne detection for the IR channel resulted in considerably improved signal-to-noise compared with the UV channel.

1.2 Experimental

1.2.1 Apparatus

Figure 1.1 is a schematic diagram of the experimental apparatus. A XeCl pulsed excimer laser (308 nm) was used to photolyze either F_2 or Cl_2, which reacted with other reagents to form the species of interest. The concentrations of the species of interest were monitored with simultaneous IR heterodyne and UV-visible direct absorption spectroscopy.

The reaction cell was a 175 cm long, 5 cm diameter Pyrex cylinder supported at each end by aluminum chambers. An insulated jacket surrounded the reaction cell through which flowed methanol chilled by a liquid-nitrogen cooled heat exchanger. Thermocouples located inside the reaction cell allowed the temperature to be measured to within ± 1 K. Reagent gases were cooled in a meter-long mixing tube prior to entering the main reaction cell. They entered from the middle of the main reaction cell and flowed towards the outlet ports. N_2 confinement gas flowing from both aluminum chambers restricted the reactants to a region 135 ± 1 cm long between the outlet ports. Tests were performed to ensure the extent of confinement by flowing gas mixtures containing known amounts of Cl_2 and NO_2 through the reagent entrance port. In these tests, the Cl_2 absorbance at 330 nm and NO_2 absorbance at 369.50 nm was measured. The effective path length was calculated using a Beer's Law analysis and tabulated absorption cross sections.[18] These tests were conducted over the range of pressures and flow rates utilized in the experiment. They confirmed that the reagent gases were contained between the two

exit ports with an effective path length matching the separation between the middle of the two ports to within 1 cm.

The excimer photolysis pulse entered the cell through a CaF_2 window on one of the aluminum chambers. The 20 ns pulses had a 2 cm by 1 cm rectangular cross section. The pulse energy ranged from 60 mJ to 150 mJ. The pulses passed through the middle of the cell, creating a 2 cm by 1 cm by 138 cm photolysis region. An unstable optical resonator configuration was used in the excimer laser to ensure good collimation of the photolysis beam.

Light from a deuterium (D_2) lamp and an IR diode laser entered the apparatus through a 30′ wedged CaF_2 window on the other aluminum chamber. Light from the D_2 lamp made one pass through the photolysis volume and was focused onto the entrance slit of a monochromater (Acton SpectraPro 300i). A PMT was mounted at the exit slit. Baffles in both aluminum chambers ensured that only UV light that had sampled the photolysis volume entered the monochromater.

For the present experiment, several species were formed which absorb in the UV. The detectable species were HO_2, NO_2, N_2O_4, H_2O_2, HO_2NO_2, $ClNO_2$, and ClONO. Their cross sections at various wavelengths are given in Table 1.1. The monochromater was set to 369.50 nm for experiments conducted at temperatures of 230 K and higher and 381.875 nm for experiments at 219 K. The 369.50 nm NO_2 cross section at 298 K was 5.23×10^{-19} cm^2 with a temperature dependence of -1.1×10^{-22} cm^2 K^{-1}.[19,20] The 381.875 nm NO_2 cross section at 298 K was taken to be 5.62×10^{-19} cm^2 with a temperature dependence of -8.7×10^{-23} cm^2 K^{-1}.[19,20] The reason for the change in UV wavelengths was to minimize absorbance by N_2O_4 at low temperature.

The IR source was a 3 mW distributed-feedback (DFB), continuous wave tunable diode laser manufactured by the JPL Microdevices Laboratory. The laser current was modulated at 6.80 MHz through an external bias tee. The beam passed through a small opening in a gold-coated mirror with a 2032 mm radius of curvature located in one aluminum chamber and impinged on a similar mirror in the other chamber positioned 1820 mm from the input mirror. These two mirrors formed a Herriott cell[21,22] that folded the IR beam, resulting in 30 passes through the photolysis volume. The beam was inside the photolysis volume for approximately 1/2 the length of a single pass between mirrors. The effective path length of the IR beam was approximately 2000 cm as determined by visual inspection of where overlap occurred. This was maximized by placing the Herriott mirrors as close to the path of the excimer beam as possible. The signal from the InGaAs photodiode detector was demodulated at 13.6 MHz (2f detection) and low-pass filtered. The filter frequency was determined by the timescale of the reaction. Typically, bandwidths greater than a factor of 5 over the pseudo-first-order HO_2 loss rate were employed. Minor adjustments of the amplitude of modulation were required to optimize the signal when the pressure and temperature of the cell was varied.

The diode laser emitted light in the region between 6620 cm^{-1} and 6645 cm^{-1}, depending on the injection current and temperature of the diode laser. The lower frequency limit was determined by the maximum temperature the diode laser chip could be held at. For emission at 6620 cm^{-1}, the temperature had to be set at around 60 ºC. At these temperatures, the lifetime of the laser is drastically reduced. Further, d(Power)/d(Current) becomes appreciably non-linear, introducing a significant amount of noise into the IR detection channel. The upper limit of the laser emission frequency was

to prevent condensation of ambient water when the diode laser was cooled below 5 ºC. The linewidth of the laser was approximately 20 MHz.[23] This was verified by deconvolving H_2O transitions at low pressure (< 200 mTorr). For the present study, an HO_2 transition at 6638.2 cm^{-1} was probed. This line is assigned to the $^qQ_2$ transition (a band head) of the first overtone of the O-H stretch.[24] Another diode laser that emitted near 7000 cm^{-1} (JPL Microdevices Laboratory) was also employed in the experiment but only for a limited number of experiments at room temperature. This diode laser probed transitions to the low-lying electronic state of HO_2 ($^2A' \leftarrow {}^2A''$). No differences in the measured kinetic parameters were observed between the two lasers. For HO_2, direct absorption measurements have suggested that the integrated band strength of the overtone transitions absorb are stronger than the electronic transitions.[25] The cross-section of the $^qQ_2$ line at 100 Torr, 298 K was estimated to be $(5 \pm 3) \times 10^{-20}$ cm^2. This was determined by observing that its signal was similar in strength to several of the strongest lines near 6627 cm^{-1}, which have been assigned to the P-branch of the $K'' = 0$ stack.[24] These lines have been observed to have cross sections between $(1 - 10) \times 10^{-20}$ cm^{-2} near 60 Torr.[26] The highest concentrations of HO_2 employed in the present experiment were around 1×10^{14} molecules cm^{-3}. The absorbance for a pathlength of 2000 cm is approximately 0.01. The difference between Beer's law analysis and simply correlating the IR signal with $[HO_2]$ is less than 1% at the maximum $[HO_2]$.

The IR and UV beams have different geometric paths, and consequently probe different regions of the photolysis volume. The IR beam probes the central half of the photolysis volume. The UV beam probes the whole length of the photolysis volume. A method of testing the agreement between the two probes was devised based on

simultaneous measurements of the HO_2 + HO_2 reaction under conditions where the concentrations of species that can hydrogen-bond with HO_2 is negligible. The formula

$$S(t) = -b + \left(\frac{1}{(S_o + b)} + 2 \cdot a \cdot t \right)^{-1} \quad (5)$$

was employed to study second-order reaction kinetics. $S(t)$ is the signal at either detector as a function of time, S_o represents the signal extrapolated to time = 0, b represents a constant baseline offset, and a represents the second-order rate constant in units of $S(t)^{-1}$ s^{-1}. For UV measurements, $S(t)$ was in units of absorbance. For IR measurements, $S(t)$ was in units of V. The product $a \cdot S_o$ for the UV and IR should be equivalent for each experiment and is units of s^{-1}. The value of a obtained from UV measurements was corrected for the contribution of H_2O_2 by multiplying its value by $1-\frac{\sigma_{H_2O_2}}{2 \cdot \sigma_{HO_2}}$, following the procedure outlined by Kircher and Sander.[27]

Simultaneous IR and UV rate measurements of reaction (4) were used to calibrate the IR signal. For rate measurements with the IR probe, calibration of the probe signal was necessary. This was accomplished by simultaneously measuring the time decay of HO_2 for HO_2 + HO_2 with the IR and UV probes, employing F_2-photolysis. The path length of the beam was 135 cm. Because the cross section and the path length were known, the UV measurement provided a second-order rate constant in units of cm^3 $molecule^{-1}$ s^{-1}. The IR probe measured a second-order rate constant in units of V^{-1} s^{-1}. The ratio of the rate constants gave the scaling factor used to translate the IR signal from

Volts to units of molecules cm^{-3}. This value ranged between $(1 - 6) \times 10^{17}$ molecules V^{-1} at the RF port of the demodulation mixer.

The photolysis volume was centrally located and wall reactions were not a concern. However, transport of reactive species from the photolysis volume into the surrounding gas by turbulent mixing was an important consideration. The reactions $C_2H_5O_2 + C_2H_5O_2$ (k_{EtO2}), and $HO_2 + HO_2$ were studied at $[C_2H_5O_2] < 1\times10^{13}$ molecules cm^{-3} and $[HO_2] < 5 \times 10^{11}$ molecules cm^{-3}, respectively. At these concentrations, $2\cdot k_{EtO2}\cdot[C_2H_5O_2]$ and $2\cdot k_4\cdot[HO_2] < 2\ s^{-1}$, and other loss processes, such as turbulent mixing, can compete with loss due to chemical reaction. The measured rates for these reactions were dependent on the residence time of the precursor gases, indicating that turbulent mixing affected measured kinetics. As the residence time was increased, the measured rates approached the predicted rates asymptotically. The measured first-order loss due to turbulent mixing was between $(2 - 5)\ s^{-1}$ for a residence time of 15 s at 298 K. Turbulent mixing affects decreased with decreasing temperature. The residence time was adjusted so turbulent mixing had less than a 5% effect on measured rates. The effect of diffusion was found to be negligible compared to turbulent mixing.

Calibrated flows of reagent gases were mixed prior to entering the cell. Flow conditions were adjusted so that the cell residence time was 3-10 s, approximately equal to the interval between photolysis laser pulses. HO_2 was formed from the reaction sequence

$$Cl_2 \xrightarrow{h\nu} 2\ Cl \qquad (6)$$

$$Cl + CH_3OH \longrightarrow HCl + CH_2OH \qquad (7)$$

$$CH_2OH + O_2 \longrightarrow HO_2 + CH_2O \qquad (8)$$

The concentrations (molecules cm^{-3}) of the reagents were Cl_2: $(2 - 6) \times 10^{15}$; He: $(2 - 5) \times 10^{16}$; CH_3OH: $(1 - 3) \times 10^{14}$; O_2: $(2 - 7) \times 10^{17}$; NO_2: $(6 - 50) \times 10^{14}$. The buffer gas was N_2 for all experiments. The Cl_2 and He came from a mixed cylinder of 10.0% Cl_2 (99.5% purity) in He (99.999%). N_2 (99.9993%) was bubbled through CH_3OH (A. C. S. Reagent Grade) in a temperature-controlled saturator to obtain the desired $[CH_3OH]$. NO_2 was prepared by mixing NO (99% purity) with a large excess of O_2 (99.996%) and allowing the mixture to stand for a day. All gases were acquired from Air Products and Chemicals, Inc. except NO, which was acquired from Matheson Tri-Gas, Inc. The maximum $[HO_2]$ formed in an individual experiment, denoted $[HO_2]_{max}$, was $(5 - 8) \times 10^{13}$ molecules cm^{-3}.

The reaction between HO_2 and NO_2 was studied under pseudo-first-order conditions with the value of $\frac{[NO_2]_o}{[HO_2]_{max}}$ between 60 and 500. The reaction was studied between 40 Torr and 200 Torr and 219 K to 295 K. Contributions to measured NO_2 absorbance at 369.50 nm and 381.875 nm from HO_2, H_2O_2, HO_2NO_2, and Cl_2 were less than 2% at all temperatures. At temperatures below 240 K for the concentrations of NO_2 employed in the present experiment, a significant fraction of NO_2 dimerized to N_2O_4. At 219 K, $\frac{[N_2O_4]}{[NO_2]}$ reached values as high as 0.8. In order to maintain $\frac{\sigma N_2O_4 \cdot [N_2O_4]}{\sigma NO_2 \cdot [NO_2]} <$ 0.05, NO_2 was monitored at 381.875 nm for experiments at 219 K.

The excimer laser photolyzed a fraction of NO_2 to produce NO + O. The fraction was determined to be 0.0028 ± 0.0002. This was measured by photolyzing NO_2 in the presence of O_2 and observing O_3 formation. Davidson et al.[20] has shown that at 219 K,

the NO_2 cross-section at 308 nm is only 2% higher than at room temperature, indicating that the fraction of NO_2 dissociated by photolysis was approximately the same at all temperatures. Knowledge of [NO] produced by photolysis of NO_2 was important because the reaction

$$HO_2 + NO \longrightarrow OH + NO_2 \qquad (9)$$

can affect the measured rate of decay of HO_2. The effect of reaction (9) was ascertained by employing the kinetics modeling program FACSIMILE[28] and the NASA recommended[18] values for the rate constants of reactions listed Table 1.2. At 50 Torr and 295 K, the ratio of the observed rate constant to the actual rate constant was calculated to be 1.06. As pressure increases and temperature decreases, the effect of reaction (9) diminishes, influencing the observed rate less than 1% at pressures greater than 100 Torr at 298 K. The observed rate was influenced by less than 3% at all other temperatures and pressures examined in the present experiment. All reported k_1 values have taken this correction into account.

1.2.2 Effect of reaction (4) on IR and UV signals

Because $\frac{[NO_2]_o}{[HO_2]_{max}} > 60$, the loss of HO_2 via reaction (1) was treated as first-order. To analyze the decay of IR and UV signals, the equation

$$s(t) = A_o \cdot \exp(-k' \cdot t) + b \qquad (10)$$

was used to fit the data, where s(t) was the absorbance signal (unitless) for the UV channel, and demodulated voltage signal (in V) for the IR channel. Reactions (1) and (4) are the major loss processes for HO_2. Since the loss by reaction (4) was second-order, fits to the data using equation 10 resulted in values of k' that were dependent on $\frac{[NO_2]_o}{[HO_2]_{max}}$, the time span in which the fitting procedure was employed, and $k_1([M],T)$. The effect of reaction (4) on measured k_1 was ascertained three different ways. First, as has been done in prior examinations[9] of k_1, kinetic modeling using FACSIMILE was used to determine the effect reaction (4) on the overall rate measurement of k_1. The largest correction to k_1 was a 5% decrease in the value observed at 50 Torr and 298 K. At 100 Torr, the correction was less than 3% for all temperatures. Second, measured k_1 values did not differ by more than 5% when $\frac{[NO_2]_o}{[HO_2]_{max}}$ was changed by an order of magnitude. Third, no significant difference in the value k_1 was observed when fits were conducted over differing time intervals. This procedure was adopted because as time proceeds, the influence of reaction (4) decreases.

A positive residual baseline signal was observed in many experiments. The magnitude of this residual was typically less than 2% of the maximum HO_2 signal. This residual showed negligible temporal dependence and was thus assumed to be constant for fitting purposes. The source of this residual was uncertain.

1.2.3 Effect of overlapping absorptions on UV signal

Table 1.1 lists several species and their cross sections at various UV wavelengths. Figure 1.2 shows the contribution of these species to the UV signal at 220 nm using the FACSIMILE kinetic modeling program and the kinetic model described in Table 1.2. The model was computed at 231 K, 100 Torr total pressure of N_2, $[NO_2] = 2 \times 10^{15}$ molecules cm^{-3}, $[CH_3OH] = 3 \times 10^{15}$ molecules cm^{-3}. H_2O_2 absorbance was negligible. Combined absorbances for ClONO and $ClNO_2$ are shown. The cross section of ClONO at 220 nm is not known and was assigned the value of 2.15×10^{-18} cm^2, a value measured by Molina and Molina[29] at 235 nm. This value was chosen because the cross section of ClONO appears to increase as wavelength decreases near 235 nm and thus would appear to be a lower limit to the actual value at 220 nm. These figures demonstrate that the acquired UV signal contains significant contributions from several species.

Despite overlapping absorptions, the HO_2 rate of decay is equivalent to the first-order rate of decay of the total UV signal if equation 10 is used to fit the data and if the concentration of all species that contribute to the signal are solely dependent on reaction (1) or are constant during the time of analysis.[30]

1.2.4 Secondary chemistry involving Cl + NO_2 recombination

Possible complications arising from the formation of ClONO and $ClNO_2$ were considered as part of the data analysis. In the present experiments, these species are formed by the reactions

$$Cl + NO_2 \xrightarrow{M} ClONO \qquad (11)$$

$$Cl + NO_2 \xrightarrow{M} ClNO_2 \qquad (12)$$

Buildup of these species can be significant depending on the relative concentrations of CH_3OH and NO_2. For example, with $[CH_3OH] = 2 \times 10^{15}$ molecules cm^{-3} and $[NO_2] = 4 \times 10^{15}$ molecules cm^{-3}, the fraction of Cl that reacts with NO_2 is 0.23 at 231 K and 100 Torr total pressure of N_2. At 298 K, the corresponding fraction is 0.13. These calculations are based on the rate constant recommendations of DeMore et al.[18] and assume that reactions (10), (11) and (12) are the only loss processes for Cl.

ClONO and $ClNO_2$ can affect the measured rate of k_1 by reacting with other species or by undergoing unimolecular processes such as decay or isomerization. Both species absorb strongly in the UV. In the present experiment, k_1 was measured in the IR for $[Cl]_{max}$ 20% of typical values. Poor signal-to-noise prevented similar measurements in the UV. No noticeable difference between these low $[Cl]_{max}$ and normal $[Cl]_{max}$ experiments was observed at 231 K and 298 K, indicating that the influence of $Cl + NO_2$ on measured kinetics was negligible.

1.2.5 Sources of uncertainty

The statistical uncertainty (1σ) in the measurement of k' due to noise in the IR signal was approximately 2%. For the UV signal, it was approximately 5%. Error in the photometric measurement of $[NO_2]$ due to changes in the flux of the NO_2 gas mixture from the NO_2 bulb, which was due to the chance in pressure of the bulb over the course of an experiment, was approximately 3%. Uncertainty in $[CH_3OH]$, which in turn was due to the fluctuations in measured gas flows and temperature of the bath surrounding the

methanol, was 3%. The uncertainty in the measured pressure was approximately 1% and in measured temperature was ± 1 K. The total uncertainty in the precision of the measurements of $k_1(T)$ ranged from approximately 5% to 10%. The observed fluctuations in measured $k_1(T)$ at 230 K and 219 K were observed to be somewhat higher, 8% to 15%, most likely due to the errors caused by imprecision in determining [CH_3OH]. The systematic uncertainty in the cross section of NO_2 at room temperature is approximately 10% at room temperature. The uncertainty in the accuracy of the vapor pressure of methanol was 5%. These systematic uncertainties are not reported in the uncertainties given for the measurements of any rate coefficients in the present work.

1.3 Results

It is demonstrated in Chapter 2 the Cl_2-CH_3OH-O_2 source of HO_2 can result in kinetic complications arising from reactions of the $HO_2 \cdot CH_3OH$ complex. Studies of reaction (1) were therefore carried out to determine both the pressure and temperature dependences of k_1 and to examine the possibility that complex formation enhances the observed reaction rate.

1.3.1 Effect of CH_3OH on reaction (1)

The effect of CH_3OH on the rate of reaction (1) was studied at 100 Torr for six different temperatures ranging from 231 K to 298 K. In addition, at 231 K, the reaction was studied at 50 Torr and 200 Torr. The observed first-order rate constant, k', for the decay of HO_2 was measured at each temperature at 16 to 25 different combinations of

[NO_2] and [CH_3OH]. Plots of [HO_2] versus time at 100 Torr, 231 K, and [NO_2] = 2.80 × 10^{15} molecules cm^{-3} are shown in Figure 1.3 for different [CH_3OH].

These experiments showed that there is a significant dependence on the apparent rate of reaction (1) with [CH_3OH]. The dependence of k' on [CH_3OH] for various [NO_2] is shown in Figure 1.4 at 100 Torr and 231 K. The dependence of k' on [CH_3OH] was well described by the equation

$$k' = k_o' + k'' \cdot [CH_3OH] \qquad (13)$$

Both k_o' and k'' were both observed to be dependent on [NO_2]. The value of k_o' represented the first-order rate constant at zero [CH_3OH]. The value of k'' represented the dependence of the measured first-order rate constant on [CH_3OH].

The trend of k_o' versus [NO_2] was observed to be linear at all temperatures and was analyzed with the equation

$$k_o' = k_{HO_2+HO_2} + k_1 \cdot [NO_2] \qquad (14)$$

where $k_{HO2+HO2}$ represents the contribution of the $HO_2 + HO_2$ reaction to the measurement of k'_o. The slope, k_1, is the rate constant for $HO_2 + NO_2$ in the limit of zero methanol. Figure 1.5 is a plot of k'_o versus [NO_2] at 100 Torr for 231 K, 250 K, and 298 K. The temperature dependence of k_1 at 100 Torr is shown in Figure 1.6. The values of k_1 are tabulated in Table 1.3. The measured values of k_1 in the present study were within 3% of

the NASA values at 298 K and 288 K and were approximately 14% lower than the NASA values at 231 K, as indicated by the last column of Table 1.3.

The trend of k'' versus $[NO_2]$ was more difficult to discern. Plots of k'' versus $[NO_2]$ are shown in Figure 1.7 for 100 Torr and the temperatures, 231 K, 250 K, and 298 K. In general, the trend appeared linear and was thus described by the equation

$$k'' = k_o'' + k^\dagger \cdot [NO_2] \qquad (15)$$

where $k^\dagger$ and k_o'' and represent the enhancement of k' of enhancement of reaction (1) and reaction (4) by CH_3OH respectively. The values of $k^\dagger$ and k_o'' are listed in Table 1.3. At 288 K and 298 K, the uncertainty in the fitted value for k_o'' was greater than the value itself. The temperature dependences of $k^\dagger$ and k_o'' were analyzed with the Arrhenius equation $k(T) = A_o \cdot \exp[(E_a/R)/T]$. Plots of $k^\dagger$ and k_o'' versus T^{-1} are shown in Figure 1.8. For $k^\dagger$, $A_o = (1.6 \pm 0.9) \times 10^{-36}$ cm^6 molecule^{-2} s^{-1} and $E_a/R = (-4360 \pm 140)$ K. For k_o'', they were $(1.9 \pm 3.0) \times 10^{-22}$ cm^3 molecule^{-1} s^{-1} and (-4760 ± 370) K, respectively.

Using the above relations, k' can be approximated at any $[NO_2]$ and $[CH_3OH]$ by the equation

$$k' = k_{HO_2+HO_2} + k_{(4.1)} \cdot [NO_2] + k_o'' \cdot [CH_3OH] + k^\dagger \cdot [NO_2] \cdot [CH_3OH] \qquad (16)$$

The effect of CH_3OH on the study of the $HO_2 + NO_2$ reaction was not accounted for in previous studies. In previous studies, the rate constant of reaction (1) was equated to the change in k' with respect to $[NO_2]$

$$\frac{dk'}{d[NO_2]} = k_1 + k^\dagger \cdot [CH_3OH] \quad (17)$$

A plot of $\frac{dk'}{d[NO_2]}$ versus temperature at $[CH_3OH] = 3 \times 10^{15}$ molecules cm^{-3} and 100 Torr is depicted in Figure 1.6. This $[CH_3OH]$ was chosen because it falls within the range used in previous experiments. As can be seen from Figure 1.6, at 231 K, 100 Torr, $\frac{dk'}{d[NO_2]}$ is a factor of 2.0 larger than k_1 measured in the present experiment and a factor of 1.7 larger than the NASA recommended values. The significant differences between $\frac{dk'}{d[NO_2]}$ from this experiment and the NASA recommended values, which were based on experiments where $[CH_3OH]$ ranged from (2 to 8) $\times 10^{15}$ molecules cm^{-3} suggests that measurements of k_1 in which HO_2 is monitored in the UV and IR differ at low temperatures.

At 231 K, the methanol enhancement of reaction (1) was investigated at 50 Torr, 100 Torr, and 200 Torr. Measurements of k_1 and $k^\dagger$ at 100 Torr and 200 Torr for 231 K are listed in Table 1.3. Three separate attempts were made at measuring k_1 and $k^\dagger$ at 50 Torr. For all three attempts, measured values of k' as a function of $[CH_3OH]$ were highly scattered and not well described by equation (13). It is unclear why this was so. The values measured at 50 Torr and 231 K are not included in our analysis.

The parameter governing the enhancement of reaction (1) by CH_3OH, $k^\dagger$, was increased slightly with pressure, from $(2.1 \pm 1.4) \times 10^{-29}$ cm^6 molecule^{-2} s^{-1} to (2.3 ± 1.9)

$\times 10^{-29}$ cm^6 molecule^{-2} s^{-1} but the difference was well within the error estimates. However, the uncertainties of the measurements make it unclear whether or not there is a pressure effect on $k^{\dagger}$. More studies over a larger range of pressures are needed. The increase in the value of k_1/k_{JPL} with pressure, noted in the last column of Table 1.4, suggests that $k^{\dagger}$ may be pressure dependent.

1.3.2 Comparison of IR and UV data

Comparisons of simultaneously acquired IR and UV signals at 100 Torr are shown in Figures 1.9.1 and 1.9.2 for 298 K and 231 K respectively. At 231 K, the IR signal indicates that HO_2 is no longer present after 3 ms; however, the UV signal is non-zero and time-dependent after 3 ms. This strongly suggests that the UV channel is sensitive to species which can interfere with the HO_2 absorption signal. Measurement of k' using 231 K UV data and equation (10) is complicated by the lack of a stable baseline UV signal after all the HO_2 has reacted (denoted post-HO_2 signal). Despite this, the data acquired at 231 K were analyzed with equation (10) over the time span of 3 ms. Plots of k' versus [NO_2] for both the IR and UV data are shown in Figure 1.10 for 298 K and 231 K. At 298 K, IR and UV measurements agree. At 231 K, there is significant disagreement.

At 231 K, a rise (from a negative absorbance towards zero absorbance) in the 400 nm post-HO_2 signal occurred simultaneously with the decrease in the 220 nm post-HO_2 signal. This suggested that NO_2 was generated from a temporary NO_2 reservoir. The 400 nm post-HO_2 signal, which has a negative absorbance value due to the consumption of NO_2 due to reaction (1), rose to a value between its most negative value and zero

absorbance and then became constant. The rate of increase in the 400 nm signal was similar to the rate of decrease in signal at 220 nm. These observations can be explained by the process

$$NO_2 + NO_2 \rightleftharpoons N_2O_4 \qquad (18)$$

Both N_2O_4, and NO_2, $\sigma_{220\,nm}^{NO_2} = (4.7 \pm 0.3) \times 10^{-19}$ cm^2 molecule^{-1},[19] contribute to the observed absorbance At 220 nm, the cross section of N_2O_4 is larger than the cross section for NO_2 (see Table 1.2) and the time-dependent signal is dominated by the loss of N_2O_2 via reaction (-18). At 400 nm, NO_2 absorbance dominates and the time-dependent signal is mainly due to the gain of NO_2 from reaction (-18).

To illustrate the absorbance change at 400 nm, consider a typical experiment in which $[NO_2]_{eq} = (1.9 \pm 0.1) \times 10^{15}$ molecules cm^{-3}. Under these conditions, $[N_2O_4]_{eq} = (5.8 \pm 0.4) \times 10^{14}$ molecules cm^{-3}.[15] Each photolysis pulse removed $(7.0 \pm 0.5) \times 10^{13}$ molecules cm^{-3} of NO_2, mainly due to reaction (1). In order for the system to reach equilibrium after the photolysis pulse, $[NO_2]$ increases by nearly 4×10^{13} molecules cm^{-3} from dissociation of N_2O_4. The change in absorbance in the 400 nm post-HO_2 signal is about 0.003 absorbance units, which is measurable in the present experiment.

The value of k_{-18} was measured to be (36 ± 10) s^{-1}. This compares favorably with previous measurements[31] of k_{-18} made at higher temperatures which predict values of k_{-18} between 20 s^{-1} and 180 s^{-1} at 231 K and 100 Torr.

Attempts were made to study reaction (1) in the absence of hydrogen-bonding species. A gas mixture of $F_2/H_2/O_2/N_2$ was flowed into the cell at concentrations (molecules cm^{-3}) of F_2: 5×10^{16}; H_2: 5×10^{16}; O_2: 5×10^{17} and balance N_2 at 100 Torr and 231 K. When NO_2 was added to the gas mixture, an unexpected explosion took place. This may have occurred as a result of a thermal, wall-catalyzed, reaction or from photolysis by ambient light. The reaction mixed was judged to be sufficiently unstable that no further studies were conducted using the F_2-H_2 system.

1.3.3 Measurements of k_1 at low [CH_3OH]

A second set of measurements of the rate of reaction (1) was obtained with [CH_3OH] = 2.0×10^{14} molecules cm^{-3}. These measurements were done between 50 Torr and 200 Torr, and between 219 K and 295 K. As stated above, complications from Cl + NO_2 were found to be insignificant. Results from the first set of experiments indicated that at 231 K, 200 Torr, and [CH_3OH] = 2.0×10^{14} molecules cm^{-3}, the calculated value of $\frac{dk'}{d[NO_2]}$ was approximately 5% greater than the measured value of k_1. At 219 K, the observed rates were calculated to be nearly 15% higher than k_1. The observed values from this second set of measurements, corrected for the presence of CH_3OH, are shown in Figure 1.11.

1.4 Discussion

1.4.1 Quantifying the results

To describe $k_1([M],T)$, a simplified version of a termolecular rate equation developed by Troe (cite) was employed. This equation, defined below,

$$k_1([\mathrm{M}],T) = \frac{k_o(T)\cdot[\mathrm{M}]}{1+\dfrac{k_o(T)\cdot[\mathrm{M}]}{k_\infty(T)}}\cdot F_c^{\left\{1+\left[\log\left(\frac{k_o(T)\cdot[\mathrm{M}]}{k_\infty(T)}\right)\right]^2\right\}^{-1}} \qquad (19)$$

has been adopted by the NASA and IUPAC data evaluation panels to describe the falloff behavior of association and unimolecular decomposition reactions. The parameters k_o(T) and k_∞(T) are the low and high pressure limiting rate constants, respectively with their temperature dependences given by

$$k_o(T) = k_o(300\mathrm{K})\cdot(T/300)^{-m} \qquad (20)$$

and

$$k_\infty(T) = k_\infty(300\mathrm{K})\cdot(T/300)^{-n} \qquad (21)$$

The parameter F_c was assigned the value 0.6 in accordance with the procedure adopted by the NASA data evaluation panel (ref). The parameters that were acquired in the fitting process were k_o(300K), k_∞(300K), m, and n. Two fitting trials are tabulated in Table 1.4. Trial 1 employed both sets of data from the present experiment. Trial 2 employed all the data of Trial 1 and also that acquired at T ≥ 277 in experiments by Sander and Peterson[8] and Kurylo and Ouellette.[9,10] Both trials were weighted by the stated uncertainties. As Table 1.4 shows, for each fitted value, the discrepancy between Trial 1 and Trial 2 is greater than the combined uncertainty.

The lack of agreement between the trials may result from insufficient parameterization of equation (19). Since one of the principal aims of this paper is to provide a description of reaction (1) that is useful for atmospheric modeling, and since the adopted procedure by the NASA data evaluation panel has adopted the use of the equation (19), further parameterization was not adopted.

As stated in the introduction, impact of reaction (1) on atmospheric chemistry is greatest from the upper troposphere to the middle stratosphere. An assessment of how each of the trials describes reaction (1) in this region of the atmosphere can be quantified by comparing the calculated rate from each of the trials to the current NASA recommended value at 231 K and 100 Torr. This has been done in Table 1.5. Both Trials calculate rates that are about 10% lower than the current recommendation. The measured value from data set 1 was 10% lower than currently recommended. Data set 1 is highlighted because was a direct measurement of k_1 at 231 K and 100 Torr.

The above analysis indicates that for modeling the chemistry of the upper troposphere to the middle stratosphere, there is little difference between Trial 1 and Trial 2 though the parameters acquired from Trial 2 best describe reaction (1) over the widest range of pressures and temperatures. Figure 1.12 depicts the difference between Trial 2 and the current recommended values.

1.4.2 Enhancement by CH_3OH

The observed enhancement of reaction (1) by CH_3OH can be explained by the reaction sequence

$$HO_2 + NO_2 \xrightarrow{M} HO_2NO_2 \quad (1)$$

$$CH_3OH + HO_2 \rightleftharpoons CH_3OH \cdot HO_2 \quad (22)$$

$$CH_3OH \cdot HO_2 + NO_2 \longrightarrow \text{Products} \quad (23)$$

If the steady-state approximation is used for $[CH_3OH \cdot HO_2]$,

$$\frac{dk'}{d[NO_2]} = k_1 + 2 \cdot k_{23} \cdot K_{22} \cdot [CH_3OH] \quad (24)$$

where $\frac{dk'}{d[NO_2]}$ is the observed rate constant discussed above and K_{22} describes the equilibrium between HO_2, CH_3OH, and $CH_3OH \cdot HO_2$. From the present experiment, the rate enhancement of reaction (1), $k^{\dagger}$, was measured to be $(1.6 \pm 0.9) \times 10^{-36} \times \exp((4360 \pm 140)/T)$ cm^6 molecule^{-2} s^{-1}. In a prior study, the enhancement of reaction (1) by CH_3OH was described in a similar fashion and measured to be $(2.5 \pm 2.4) \times 10^{-36} \times \exp(-4570 \pm 120)$ cm^6 molecule^{-2} s^{-1}.[17] If it is assumed that the rate of reaction (23) depends very little on temperature, then the temperature dependence of the enhancement can be shown result from the enthalpy change of K_{eq}. In the present study, the enthalpy change for reaction (1) was measured to be -(8.66 ± 0.28) kcal mol^{-1}. For reaction (4), the enthalpy change was measured to be -(9.1 ± 0.2) kcal mol^{-1}. Both these values correspond to strong hydrogen bonded complexes.

The similarity in enhancement between reactions (1) and (4) suggests that the process $HO_2 + CH_3OH \cdot X \rightarrow$ Products, where X = HO_2 or NO_2, may occur at near collision frequency as has been suggested by prior researchers.[16]

1.4.5 Conclusion

The effect of methanol on the observed rate of $HO_2 + NO_2$ was measured. This information was used to measure the rate constant of $HO_2 + NO_2$ in limit of zero methanol k_1. IR spectroscopy was employed, minimizing the influence of the equilibrium between NO_2 and N_2O_4 in determining the rate, a process not taken into account in prior studies. The results indicated that at temperatures lower than 250 K, k_1 was lower than the current NASA recommended values. At 231 K, 100 Torr, k_1 was nearly 10% lower. Parameterizations of the rate of k_1 using a simplified Troe termolecular equation was done using the present data in addition to that taken by prior researchers. Only data that in which the effect of CH_3OH was minimal was included. It was found that the simplified equation did not adequately describe all the data. However, it did describe the rate of reaction (1) in the pressure and temperature regime of importance to atmospheric chemistry.

The methanol effect was analyzed and found to be remarkable similar to that for the enhancement of the $HO_2 + HO_2$ system. This suggests that current models discussed in the literature approximate the process well.

Acknowledgements

This research was carried out by the Jet Propulsion Laboratory, California Institute of Technology, under contract with the National Aeronautics and Space Administration. Support is acknowledged from the NASA Upper Atmosphere Research and Tropospheric Chemistry Programs. This research has also been supported in part by a grant from the U.S. Environmental Protection Agency National Center for Environmental Research's Science to Achieve Results (STAR) program, through grant R826236-01-0. It has not been subjected to any EPA review and therefore does not necessarily reflect the views of the Agency, and no official endorsement should be inferred. We would like to acknowledge the technical support of Dave Natzic, Jürgen Linke, Siamak Forouhar, Dave Dougherty, and Sam Keo of JPL.

1.5 References

1. Simonaitis, R. and J. Heicklen J. Phys. Chem 78: 653 (1974).

2. Cox, R. A. and R. G. Derwent J. Photochem. 4: 139 (1975).

3. Simonaitis, R. and J. Heicklen J. Phys. Chem 80: 1 (1976).

4. Howard, C. J. "Kinetics of the reaction of HO_2 with NO_2." J. Chem. Phys. 67: 5258 (1977).

5. Niki, H., P. Maker, et al. "FTIR of PNA from HO_2 + NO_2." Chemical Physics Letters 45: 564 (1977).

6. Simonaitis, R. and J. Heicklen Int. J. Chem. Kinet. 10: 67-87 (1978).

7. Cox, R. A. and R. Patrick Int. J. Chem. Kinet. 11: 635 (1979).

8. Sander, S. P. and M. Peterson "HO_2 + NO_2." J. Phys. Chem. 88: 1566-1571 (1984).

9. Kurylo, M. J. and P. A. Ouellette "$HO_2 + NO_2$." J. Phys. Chem. 90: 441-444 (1986).

10. Kurylo, M. J. and P. A. Ouellette "Rate Constants for the Reaction $HO_2 + NO_2 + N_2 -> HO_2NO_2 + N_2$: The Temperature Dependence of the Falloff Parameters." J. Phys. Chem. 91: 3365-3368 (1987).

11. WMO (1983). *The Statosphere: 1981*, NASA.

12. Rinsland, C. P., R. Zander, et al. "Evidence for the Presence of the 802.7 cm^{-1} Band Q Branch of HO_2NO_2 in High Resolution Solar Absorption Spectra of the Stratosphere." Geophysical Research Letters 13: 761-764 (1986).

13. Sen, B., G. C. Toon, et al. "Measurements of Reactive Nitrogen in the Stratosphere." Journal of Geophysical Research-Atmospheres 103: 3571-3585 (1998).

14. Atkinson, R., D. L. Baulch, et al. "Summary of Evaluated Kinetic and Photochemical Data for Atmospheric Chemistry - Web Version December 2000." (2000).

15. Sander, S. P., R. R. Friedl, et al. (2000). Chemical Kinetics and Photochemical Data for Use in Stratospheric Modeling, Evaluation Number 13. Pasadena, CA, Jet Propulsion Laboratory, California Institute of Technology.

16. Andersson, B. Y., R. A. Cox, et al. "The Effect of Methanol on the Self Reaction of HO_2 Radicals." Int. J. Chem. Kinetics 20: 283-295 (1988).

17. Christensen, L. E., S. P. Sander, et al. "Kinetics of $HO_2 + HO_2 \rightarrow H_2O_2 + O_2$: Implications for Stratospheric H_2O_2." Geophysical Research Letters (2002).

18. DeMore, W. B., S. P. Sander, et al. (1997). Chemical Kinetics and Photochemical Data for Use in Stratospheric Modeling, Evaluation Number 12. Pasadena, CA, Jet Propulsion Laboratory, California Institute of Technology.

19. Bass, A. M., A. E. Ledford, et al. J. Res. NBS 80A: 143-166 (1976).

20. Davidson, J. A., C. A. Cantrell, et al. J. Geophys. Res. 93: 7105-7112 (1988).

21. Herriott, D. and H. Schulte "Folded Optical Delay Lines." Appl. Optics 4: 883-889 (1965).

22. Trutna, W. and R. Byer "Multiple-pass Raman gain cell." Appl. Optics 19: 301-312 (1980).

23. Monsour, J. (2001). Private communication.

24. Tuckett, R. P., P. A. Freedman, et al. "The emission bands of HO2 between 1.43 and 1.51 microns." Molecular Physics 37: 379-401 (1979).

25. Hunziker, H. E. and H. R. Wendt J. Chem. Phys. 60: 4622 (1974).

26. Johnson, T. J., F. G. Wienhold, et al. J. Phys. Chem 95: 6499-6502 (1991).

27. Kircher, C. C. and S. P. Sander "Kinetics and Mechanism of HO_2 and DO_2 Disproportionations." J. Phys. Chem. 88: 2082-91 (1984).

28. Curtis, A. R. and W. P. Sweetenham (1987). FACSIMILE/CHEKMAT, H015 ed. Harwell: Oxfordshire (UK).

29. Molina, L. T. and M. J. Molina Geophys. Res. Lett. 4: 83-86 (1977).

30. Sander, S. P. and R. T. Watson J. Phys. Chem. 84: 1664 (1980).

31. Markwalder, B., P. Gozel, et al. J. Chem. Phys. 97: 5472-5479 (1992).

Table 1.1. Cross sections for various species.

species	σ220nm [a]	σ225nm [a]	σ230nm [a]	σ400nm [a]	ref.
HO_2	3.41	2.88	2.30		18
NO_2	0.47	0.39	0.28	0.60	19
N_2O_4	6.68	4.11	2.55		19
HO_2NO_2	1.18	0.94	0.79		18
H_2O_2	0.26	0.22	0.18		18
Cl_2				0.02	18
$ClNO_2$	3.39	2.83	2.26		29

[a] units are 10^{-18} cm^2

Table 1.2. Relevant reactions.

Reaction	Reference
$Cl + CH_3OH \rightarrow HCl + CH_2OH$	NASA
$CH_2OH + O_2 \rightarrow HO_2 + CH_2O$	NASA
$HO_2 + HO_2 \rightarrow H_2O_2 + O_2$	My GRL
$NO + HO_2 \rightarrow NO_2 + OH$	NASA
$OH + NO_2 \rightarrow HNO_3$	NASA
$OH + HO_2 \rightarrow H_2O + O_2$	NASA
$Cl + HO_2 \rightarrow HCl + O_2$	NASA
$HO_2 + NO_2 + M \rightarrow HO_2NO_2 + M$	NASA
$Cl + NO_2 + M \rightarrow ClONO + M$	NASA
$Cl + NO_2 + M \rightarrow ClNO_2 + M$	NASA
$Cl + ClONO \rightarrow Cl_2 + NO_2$	NASA
$Cl + ClNO_2 \rightarrow Cl_2 + NO_2$	NASA
$NO_2 + NO_2 + M \rightarrow N_2O_4 + M$	This expt.
$N_2O_4 + M \rightarrow NO_2 + NO_2 + M$	This expt.

Table 1.3. Fitted values at different temperatures.

T (K)	P [a]	k_1 [b]	$k^{\dagger}$ [c]	k_o'' [d]	k_1/k_{JPL}
298	100	4.0±0.1	0.24±0.06	too noisy	1.00
288	100	4.4±0.1	0.58±0.09	0.9±2.0	0.98
273	100	5.1±0.1	1.5±0.2	4.5±3.2	0.93
250	100	6.7±0.1	6.3±0.2	41±2	0.92
240	100	6.9±0.1	13.8±0.4	80±5	0.83
231	100	8.5±0.3	20.7±1.4	160±10	0.90
231	200	9.4±0.4	23.0±1.9	200±60	0.66

[a] units are Torr

[b] units are 10^{-13} cm^3 $molecule^{-1}$ s^{-1}

[c] units are 10^{-29} cm^6 $molecule^{-2}$ s^{-1}

d units are 10^{-15} cm^3 $molecule^{-1}$ s^{-1}

Table 1.4. Fitted values for Troe equation.

Trial	k_o [a]	n	k_∞ [b]	m	fit/k_{NASA}
1	2.4 ± 0.1	2.1 ± 0.3	1.9 ± 0.1	4.2 ± 0.4	0.93
2	1.9 ± 0.1	3.7 ± 0.2	2.9 ± 0.1	1.1 ± 0.3	0.89

[a] units are 10^{-31} cm^6 $molecule^{-2}$ s^{-1}

[b] units are 10^{-12} cm^3 $molecule^{-1}$ s^{-1}

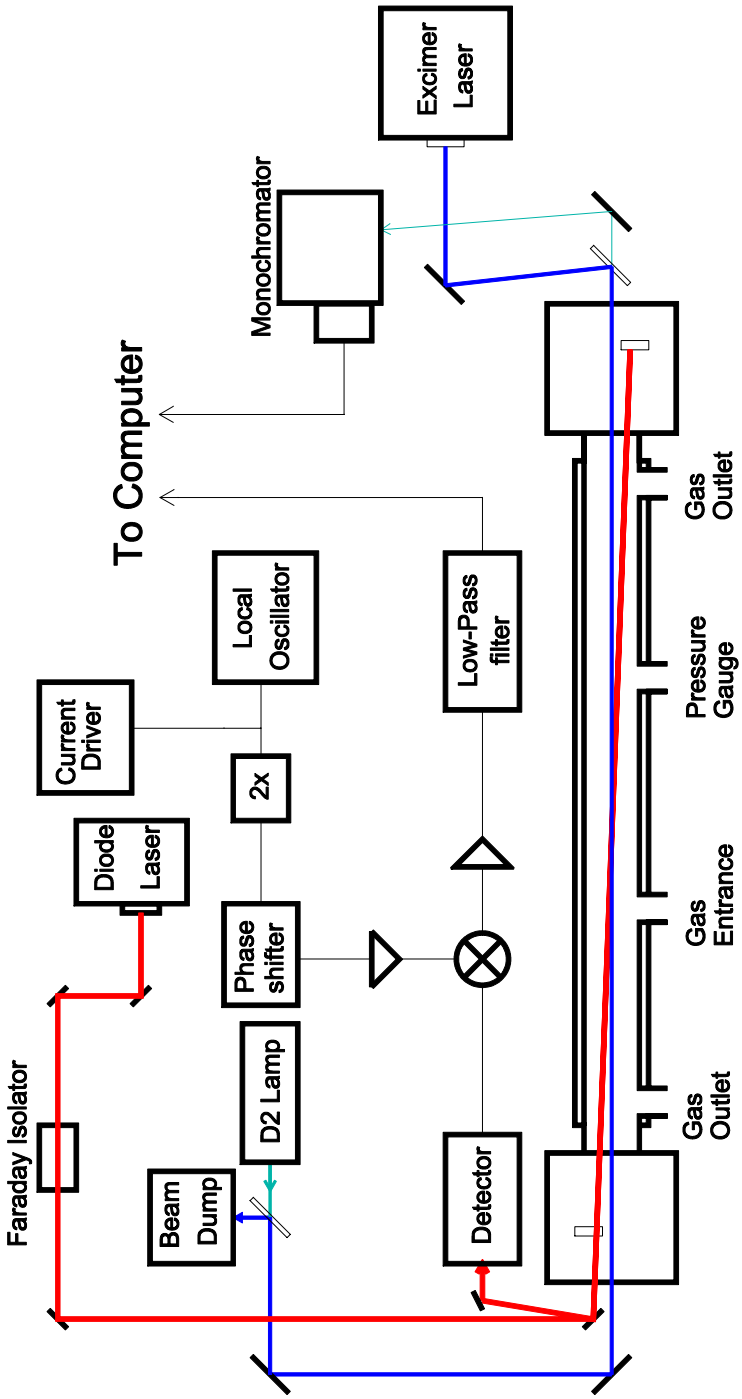

Figure 1.1. Experimental apparatus.

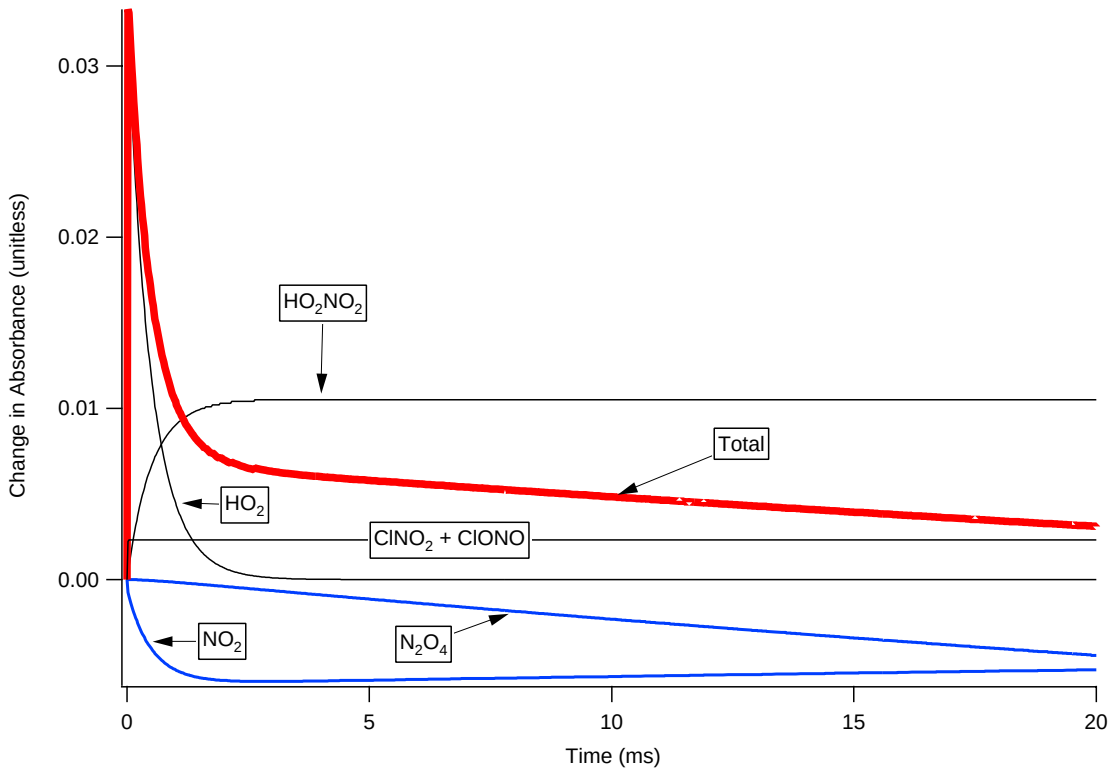

Figure 1.2. Simulated UV absorbances at 369.50 nm using FACSIMILE.

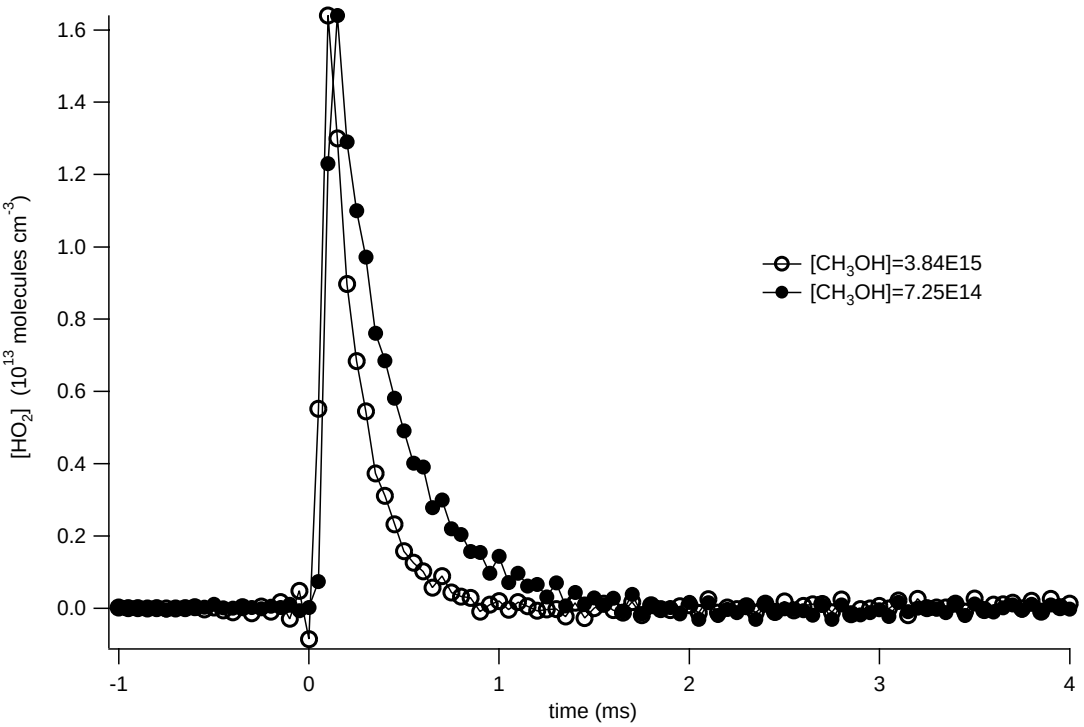

Figure 1.3. Decay of $[HO_2]$ due to the $HO_2 + NO_2$ reaction at different $[CH_3OH]$ at 231 K, 100 Torr.

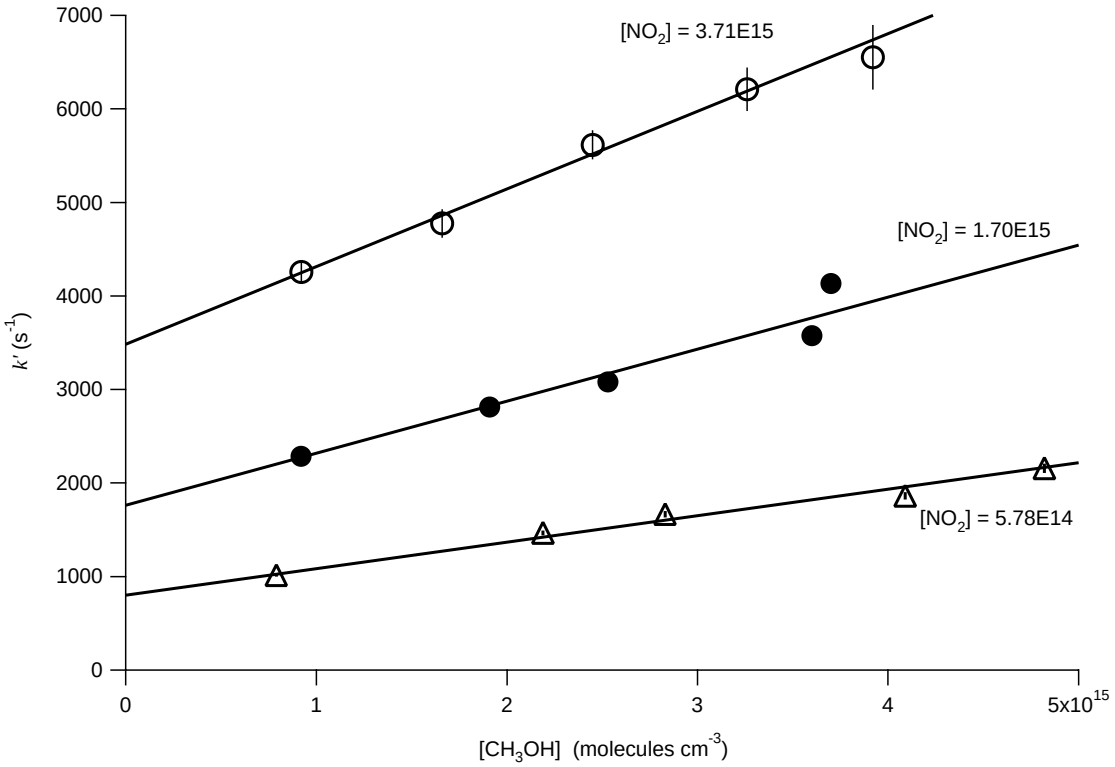

Figure 1.4. k' versus $[CH_3OH]$ for various $[NO_2]$ at 231 K, 100 Torr.

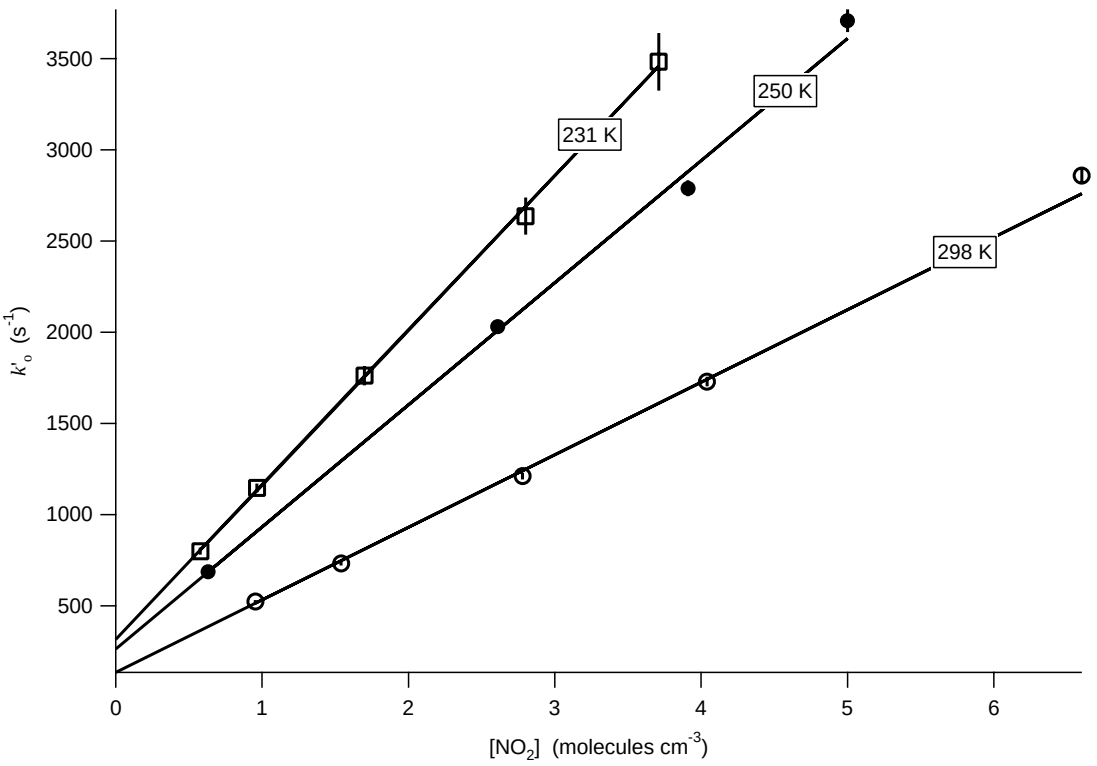

Figure 1.5. k'_o versus [NO_2]. The slope of the line is k_1, the rate coefficient for the HO_2 + NO_2 + M reaction in the absence of methanol.

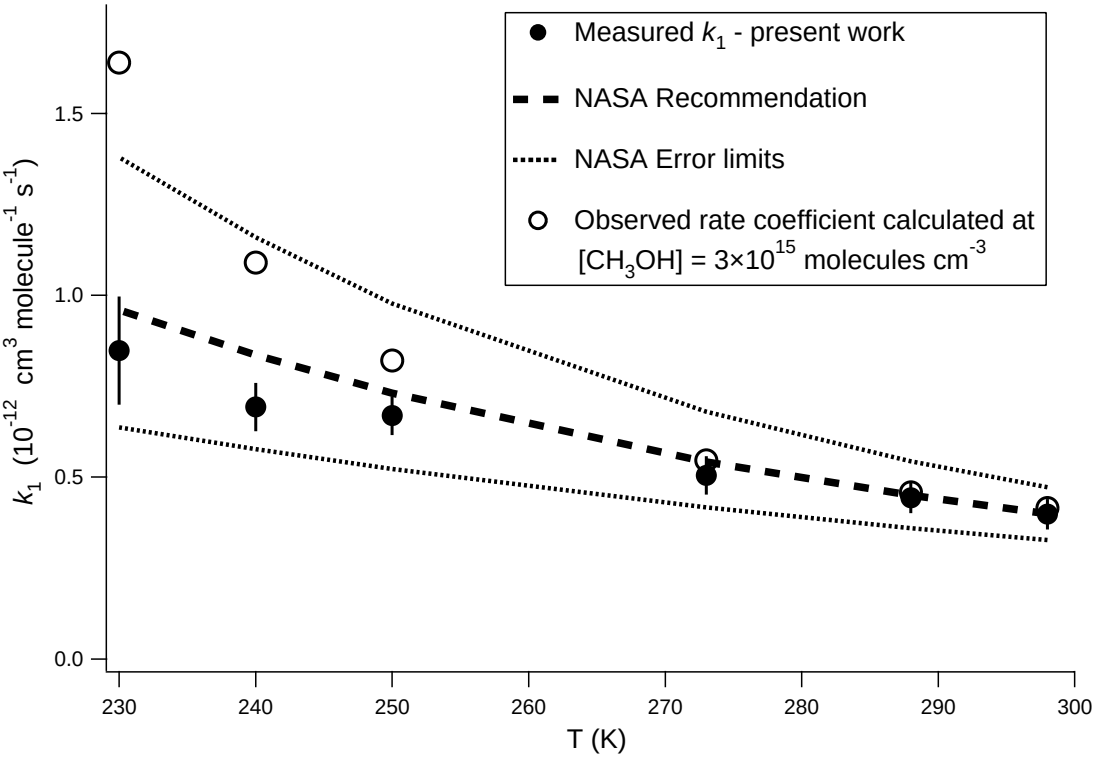

Figure 1.6. k_1 versus T compared with the NASA recommendation and expected rate if the $HO_2 + NO_2$ reaction were studied using $[CH_3OH] = 3 \times 10^{15}$ molecules cm^{-3}.

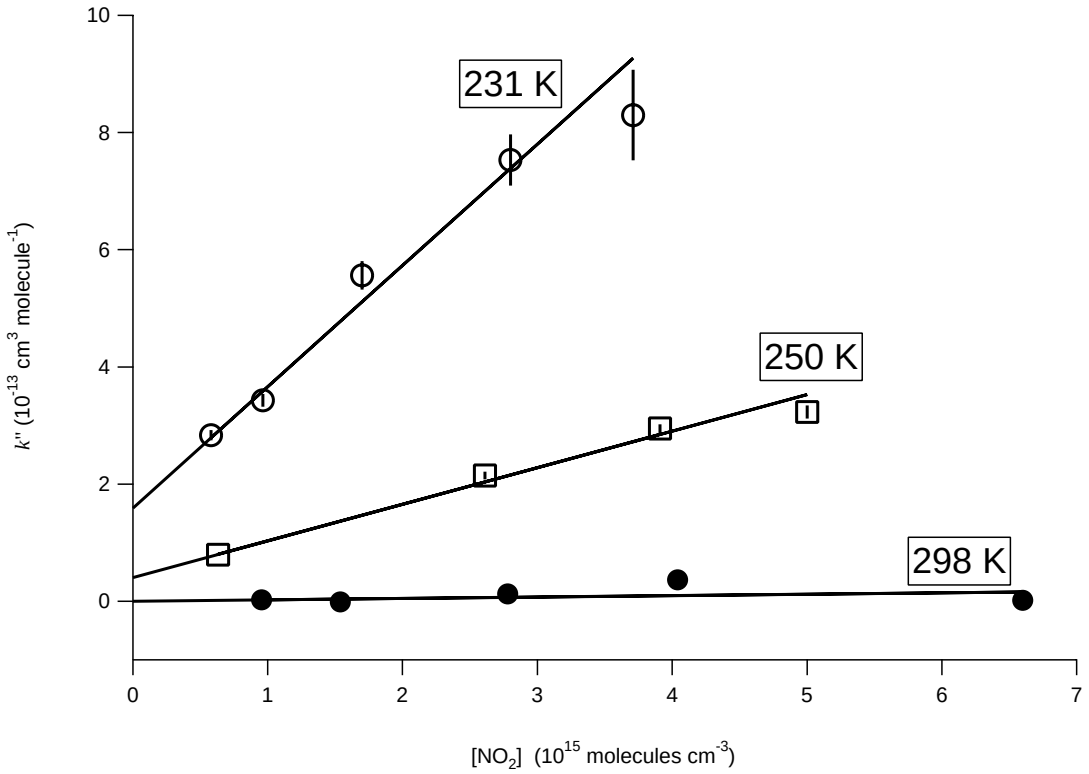

Figure 1.7. k'' versus $[NO_2]$. k'' represents the enhancement in the observed first-order rate due to methanol. The slope of the above plots represent the enhancement of the $HO_2 + NO_2 + M$ reaction due to methanol. The intercepts represent the enhancement of the $HO_2 + HO_2$ reaction due to methanol.

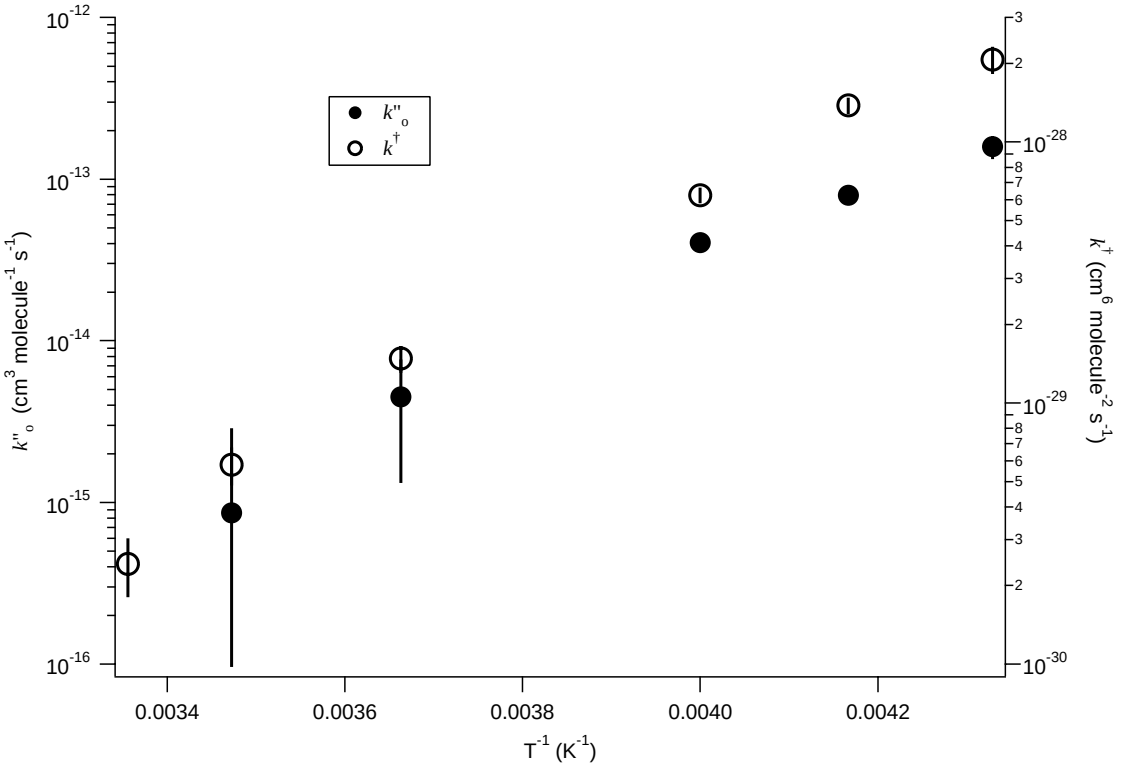

Figure 1.8. k''_o and $k^\dagger$ versus T^{-1}.

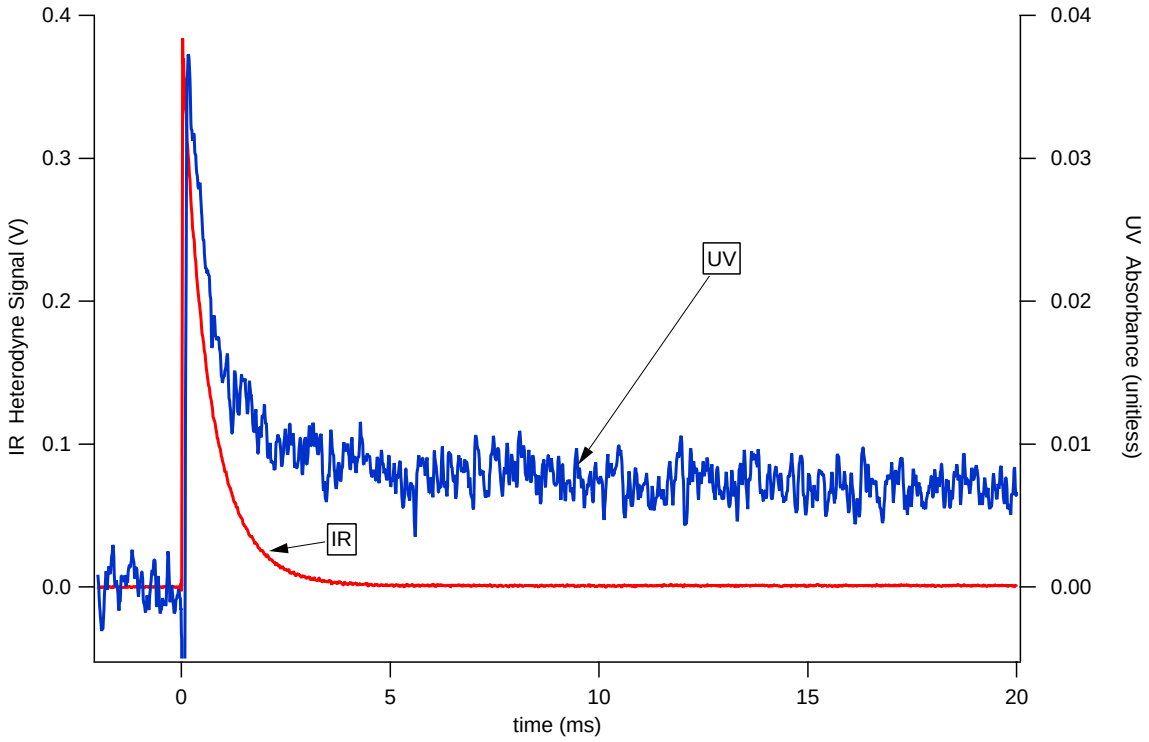

Figure 1.9.1. Comparison of UV and IR signals at 298 K. The UV signal was acquired at 220 nm.

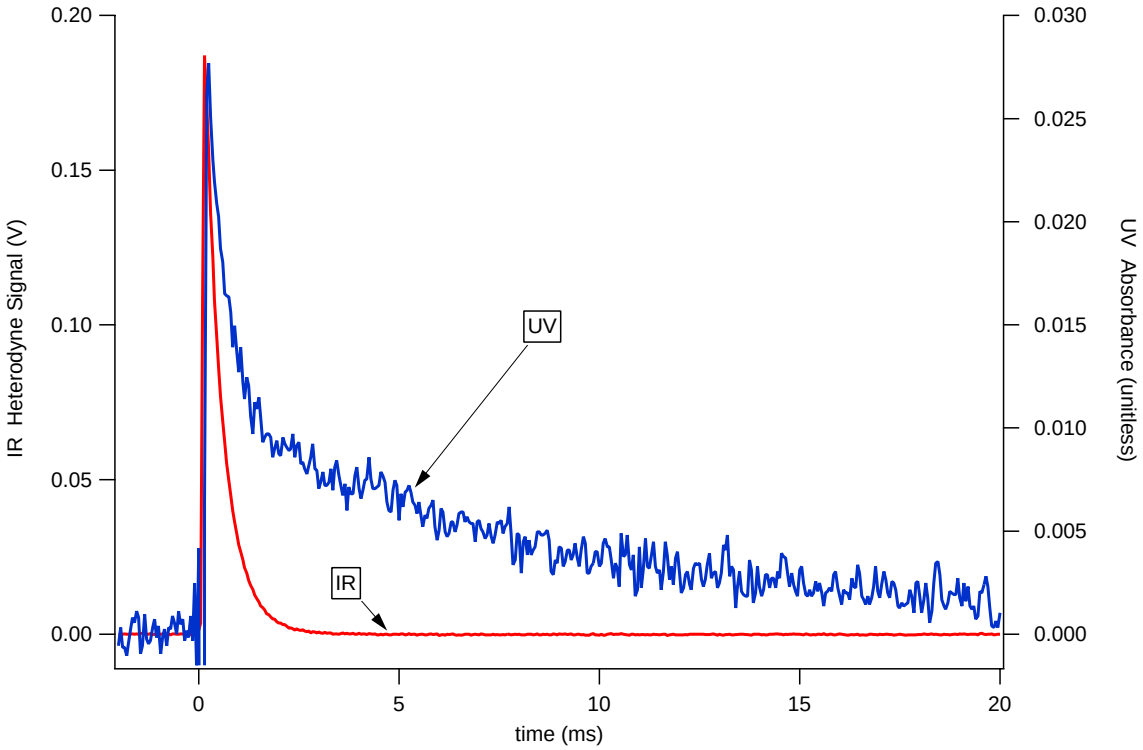

Figure 1.9.2. Comparison of UV and IR signals at 231 K. The UV signal was acquired at 220 nm.

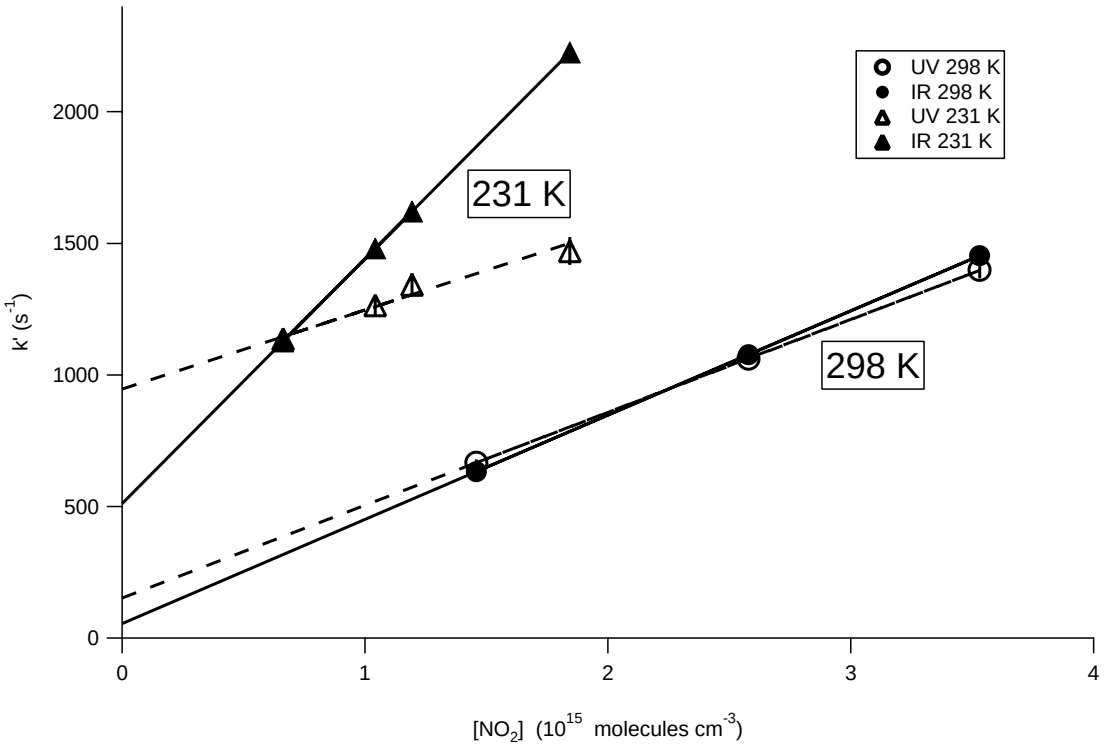

Figure 1.10. k' versus $[NO_2]$. Comparisons of IR and UV signals at 231 K and 298 K. The UV signals were acquired at 220 nm.

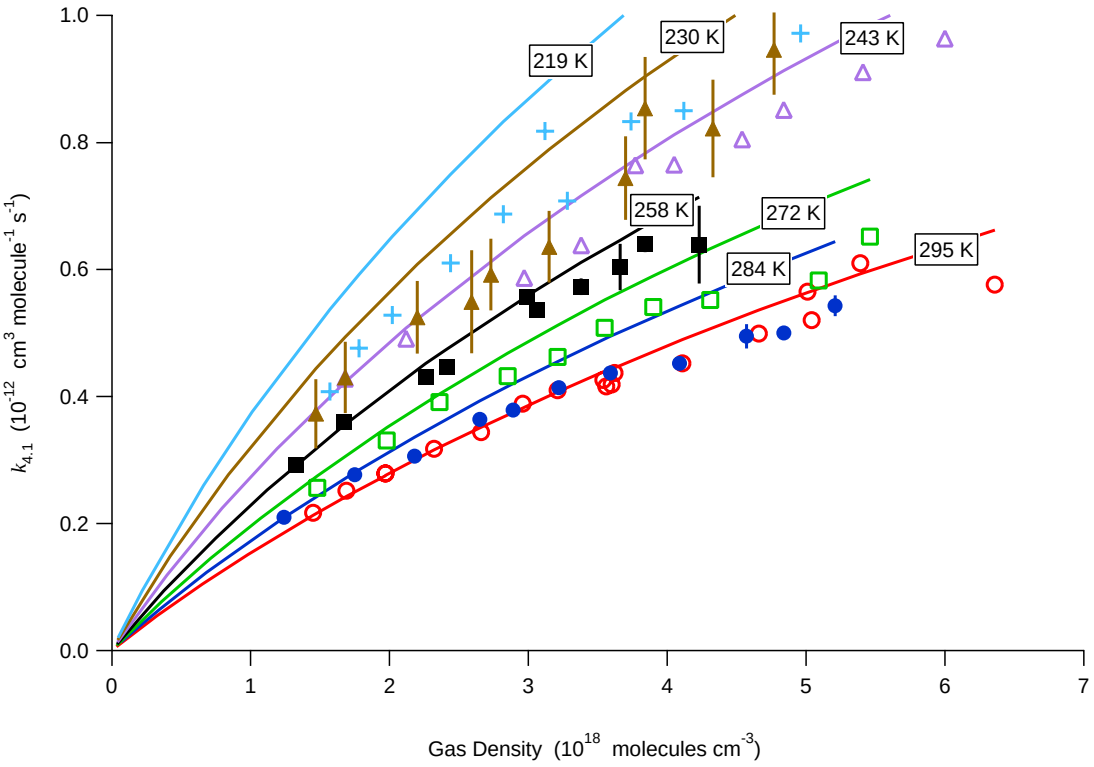

Figure 1.11. Measured rates of k_1 from the present work (individual points) using $[CH_3OH] = 4 \times 10^{14}$ molecules cm^{-3} compared with the NASA recommended values (lines).

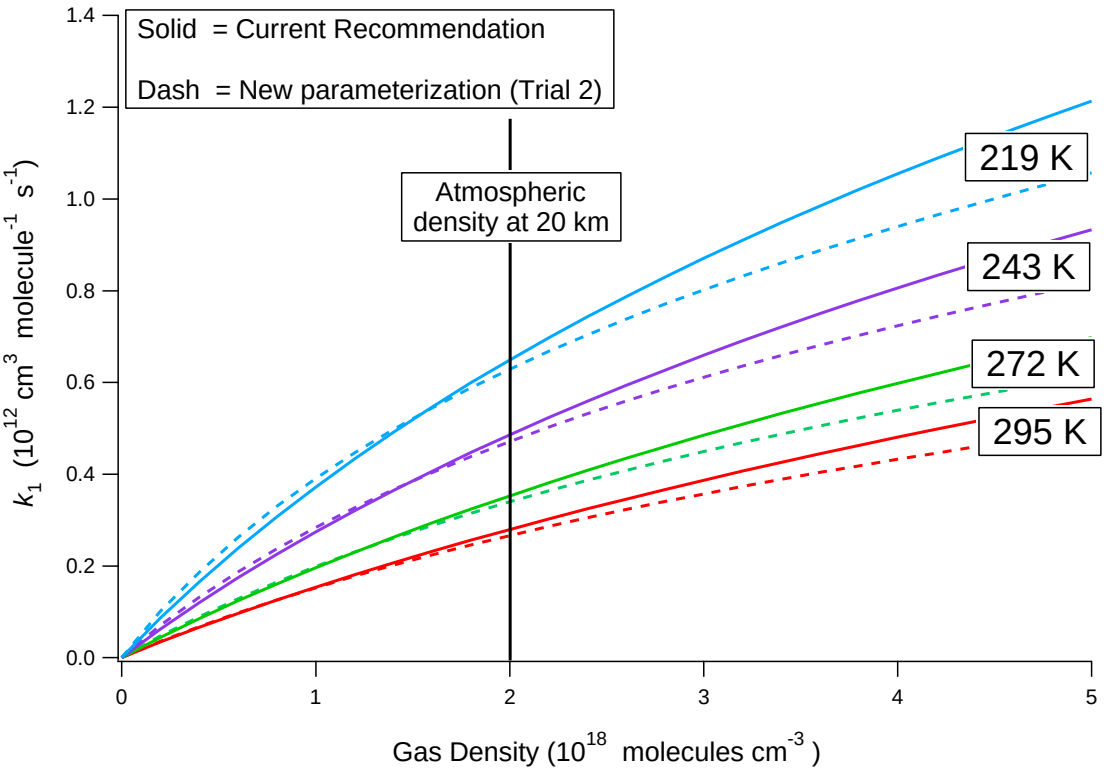

Figure 1.12. Comparison of NASA recommended k_1 versus k_1 from new parameterization employing the kinetic data from this work with previous studies in which only measurements in which the influence of methanol was insignificant were used.

Chapter 2: Kinetics of $HO_2 + HO_2 \rightarrow H_2O_2 + O_2$: Implications for Stratospheric H_2O_2

2.1 Introduction

The principal source of upper tropospheric and stratospheric H_2O_2 is the reaction

$$HO_2 + HO_2 \longrightarrow H_2O_2 + O_2 \qquad (1)$$

Reaction (1) is an important sink for HO_x in the troposphere because H_2O_2 is scavenged by aerosols and clouds. In the stratosphere, H_2O_2 serves as a temporary reservoir for HO_x.

Remote measurements of stratospheric [H_2O_2] have indicated that our understanding of the H_2O_2 budget is incomplete. Measurements, shown below, by the balloon-borne MkIV and FIRS-2 spectrometers indicate that photochemical models employing recommended rate constants significantly over-estimate [H_2O_2] in the lower to middle stratosphere. This has prompted researchers to explore previously unrecognized loss processes for H_2O_2 such as the $H_2O_2 + O_3$ reaction.[1] So far, laboratory studies have been unable to explain the discrepancy.

Reaction (1) has been widely studied (see references in *DeMore et al.*[2]). However, there are comparatively few studies below 273 K. The NASA[2] and IUPAC[3] recommendations at low temperatures have been influenced by studies that employed

CH_3OH as a precursor for HO_2. It has been demonstrated that the observed rate of reaction (1) is enhanced in the presence of CH_3OH, H_2O, and NH_3 and that this rate enhancement is more pronounced at low temperatures[4-6]. The effect of methanol has been the subject of only one study, at 278 K and 299 K.

In the present study, the effect of methanol on reaction (1) was examined over the temperature range 222 K to 295 K. We defined k_1 as the rate constant for reaction (1) in the limit of zero added methanol and derived $k_1(T)$ at 100 Torr of combined O_2 (40%) and N_2 (60%). The temperature dependence of the methanol enhancement effect was also measured. The new value of $k_1(T)$ was used to compare measured volume mixing ratio (VMR) profiles of stratospheric H_2O_2 with model calculations.

2.2 Experimental Details

The experiments were performed in a pulsed laser photolysis kinetic spectroscopy apparatus described in detail in Chapters 1 and 5. Briefly, HO_2 was generated in a 2-m long temperature-controlled flow cell by laser photolysis at 308 nm of either Cl_2 or F_2 in the gas mixtures $CH_3OH/O_2/N_2$ and $H_2/O_2/N_2$, respectively. The laser fluence was 120 mJ pulse^{-1}. HO_2 decay curves were monitored simultaneously by UV and near-IR diode laser spectroscopy. The measurements made in the UV are the subject of this paper. The near-IR measurements of $[HO_2]$, which did not contain any spectral interference from other species and supported the UV measurements, are discussed in Chapter 3. The concentrations and specifications of the gases and methanol are listed in Table 2.1.

The photolysis beam traveled coaxially through the reaction cell (5-cm diameter) resulting in a photolysis volume with a cross section of 1 cm by 2 cm. Reagent gases were mixed and cooled prior to entering the middle of the reaction cell. N_2 buffer gas was

flowed into both ends of the cell, constraining the reagent gases to an evenly mixed 134 cm long region. This was verified from measurements of gases with flow-meter calibrated concentrations and known cross sections and further verified by examinations of second-order reactions involving CH_3O_2 and $CH_3CH_2O_2$ which yielded results consistent with observations made by prior investigators. The residence time of the gas was 3 seconds, and a photolysis flash occurred every 3.5 seconds. Methanol was added to the cell by bubbling N_2 through liquid methanol that was situated in a temperature-controlled bath.

Light from a 150 W deuterium lamp was propagated collinearly with the photolysis beam and made a single pass of path length 134 cm. HO_2 was detected by UV absorbance at 220.00 nm. The rate of decay was corrected to account for the time-dependent absorbance by H_2O_2, a product of reaction (1) [5]. The value used for the cross-sections of HO_2 and H_2O_2 at 220.00 nm were $3.41 \cdot 10^{-18}$ cm^2 and $2.58 \cdot 10^{-19}$ cm^2, respectively.[2,7] Both cross sections were assumed to be independent of temperature and pressure.

We defined k_{obs} as the second-order rate constant, measured in the presence of methanol, and corrected for absorbance of H_2O_2. In each experiment, we measured the HO_2 decay over 38 milliseconds. At a given temperature and methanol concentration, k_{obs} was determined from the average of 3 individual experiments. At each temperature, k_{obs} was measured at 5 to 10 different methanol concentrations. As shown below, k_{obs} was linearly dependent on [CH_3OH]. We expressed the enhancement due to methanol as

$$k_{obs} = k_1 + k'' \cdot [CH_3OH] \qquad (2)$$

where k_1 is the rate constant of reaction (1) in the limit of zero methanol, k'' is the enhancement factor due to the presence of methanol. Equation (2) was fit to k_{obs} vs. $[CH_3OH]$. From the fit, k_1 was determined from the y-intercept and k'' was determined from the slope.

The uncertainty (2σ) in k_{obs} due to the statistical noise in the UV signal was 2% while the uncertainty in determining $[CH_3OH]$, which in turn was due to the fluctuations in measured gas flows and temperature of the bath surrounding the methanol, was 5%. The relationship between k_{obs} and $[CH_3OH]$ was not well described by equation (2) at 222 K. This was correlated with slight deviations from second-order rate behavior at high $[CH_3OH]$.

Seven different temperatures, from 222 K to 295 K, were investigated. The temperature dependences of k_1 and k'' were fit to the Arrhenius expression $k(T) = A \cdot \exp[-(E_a/R)/T]$ using weighted non-linear least-squares fitting. Weights were the uncertainties derived from the linear fitting of k_1 and k'' and the uncertainty in temperature (± 1 K).

The effects of secondary reactions were considered as a possible cause for the observed rate enhancement. At all temperatures, the maximum $[HO_2]$ did not change for $[CH_3OH] > 1 \cdot 10^{15}$ molecules cm^{-3}; at the lowest $[CH_3OH]$ employed, maximum $[HO_2]$ decreased by 10%. Competing secondary reactions such as $Cl + O_2$ and $Cl + HO_2$ would account for the decrease in maximum $[HO_2]$. The kinetics modeling program FACSIMILE[8] was employed to ascertain the effects of these secondary reactions. It was found that their effects were negligible. More than half of the experiments were done

with $[CH_3OH] > 1.0 \cdot 10^{15}$ molecules cm^{-3}. There was no discernable difference in the slope of k_{obs} versus $[CH_3OH]$ above and below this methanol concentration.

2.3 Laboratory Results and Discussion

The dramatic effect of methanol on the observed rate constant is demonstrated in Figure 2.1. At 295 K, there was very little change in k_{obs} when $[CH_3OH]$ was varied over the range $(1 \text{ to } 5) \cdot 10^{15}$ molecules cm^{-3}. At 231 K, k_{obs} more than doubled over the same range of $[CH_3OH]$.

Figure 2.2 compares the temperature dependence of k_1 with the JPL00-3 recommended values at 100 Torr. At 295 K, our results are within 7% of the current recommended values, but at 231 K, we find that the rate constant is only 59% of the current recommended value. Our measured values (2σ) of A and E_a/R for k_1 were $(8.8 \pm 0.9) \cdot 10^{-13}$ cm^3 $molecule^{-1}$ s^{-1} and (-210 ± 26) K, respectively.

In order to validate the approach used in the derivation of k_1, 308 nm photolysis of $F_2/H_2/O_2/N_2$ mixtures was used to produce HO_2. These experiments were conducted at two temperatures, 231 K and 295 K. The results, plotted in Figure 2.2, show that k_1 values obtained by extrapolating to zero methanol were statistically consistent with k_1 in the absence of methanol. Possible interferences from FO_2 were determined to be negligible.

Our measured temperature dependence leads to a negative E_a that is half that reported by prior investigators. The study by *Kircher and Sander*[5] (*KS*) is similar to the JPL and IUPAC recommendations and has influenced the recommendations for temperatures below 273 K. Their study was conducted between 240 K and 417 K and

employed $[CH_3OH] = (1 \text{ to } 5) \cdot 10^{15}$ molecules cm^{-3}. The discrepancy between our results and those of *KS* can be explained by taking into account the enhancement in k_{obs} by methanol. In Figure 2.2, we plot $k_{obs}(T)$, calculated for $[CH_3OH] = 3 \cdot 10^{15}$ molecules cm^{-3}, using the values for k_1 and k'' measured in the present experiment. The plot demonstrates that we obtain the same observed reaction rate as *KS* under the same experimental conditions. The plot also shows that at temperatures below 240 K, the calculated rate constant begins to diverge from the recommended values. At 220 K, the calculated values are 2 times larger.

To date, there are five published experimental studies of reaction (1) at temperatures below 273 K. Studies conducted by *KS*, *Lightfoot et al.*[9] and *Takacs and Howard*[10] employed methanol. A study by *Dobis and Benson*[11] inferred k_1 indirectly from reactions initiated by $Cl + C_2H_6$ and has not influenced current recommendations. *Maricq and Szente*[12] studied reaction (1) in the absence of methanol. They utilized $F_2/H_2/O_2/N_2$ gas mixtures at 200 Torr and reported results similar to the current recommendations but in disagreement with our results at low temperatures. At 222 K, their results agree with the current recommendations, and are 40% higher than our value of k_1 at zero-added methanol after extrapolating to 100 Torr using the JPL recommended pressure-dependence. They analyzed HO_2 decays over a shorter time period, when competing reactions are more important, and formed higher maximum $[HO_2]$ than in our experiment.

An Arrenhius plot for k'' is shown in Figure 2.3. The measured A and E_a/R values (2σ) for k'' were $(2.5 \pm 5.9) \cdot 10^{-36}$ cm^6 $molecule^{-2}$ s^{-1} and (-4570 ± 240) K, respectively. Also plotted in Figure 2.3 are measurements of k'' by *Andersson et al.*[6] which agree favorably with our results at the two temperatures they investigated, 278 K and 299 K.

The rate enhancement due to methanol can be explained in terms of a hydrogen-bonded complex. Prior investigators of the rate enhancement by CH_3OH, H_2O, and NH_3 on reaction (1) have postulated that the effect is due to a hydrogen-bonded complex that reacts with HO_2 faster than HO_2 reacts with itself.[4-6] For methanol, the scheme can be described as

$$CH_3OH + HO_2 \overset{M}{\rightleftharpoons} CH_3OH \cdot HO_2 \qquad (3)$$

$$CH_3OH \cdot HO_2 + HO_2 \longrightarrow H_2O_2 + O_2 + CH_3OH \qquad (4)$$

where $k_4 > k_1$. The temperature dependence of k'' can be shown to result from the enthalpy change due to equilibrium (3).[13] The measured E_a/R for k'' in our experiment was equivalent to (-9.08 ± 0.48) kcal mol^{-1}, which is consistent with the stabilization energy of a strongly hydrogen-bonded complex. This is discussed in Chapter 3.

Reaction (1) proceeds via a complex potential energy surface and displays pressure-dependent behavior. Both the NASA and IUPAC recommendations separate the expression for the overall rate constant into two terms, i.e.,

$$k_1 = k_o + k' \cdot [M] \qquad (0.5)$$

where k_o and k' are the bimolecular and termolecular components, respectively. For the model calculations discussed below, we obtained k_o from equation (0.5) using the JPL97-4 recommended $k' = 1.7 \cdot 10^{-33} \cdot [M] \cdot \exp[1000/T]$, where the suggested uncertainty factor is 1.3 and 2 at 298 K and 220 K, respectively (see *DeMore et al.*[2] for an explanation of

the uncertainty factor). The following best-fit Arrenhius parameters (2σ) were obtained for $k_o(T)$: $A = (1.5 \pm 0.2) \cdot 10^{-12}$ cm^3 molecule^{-1} s^{-1} and $E_a/R = (-19 \pm 31)$ K.

2.4 Atmospheric Implications

Measurements of H_2O_2 from space using infrared spectroscopy are potentially a powerful way to ascertain [HO_x] in the lower stratosphere and upper troposphere. In these regions of the atmosphere, loss of H_2O_2 by photolysis

$$H_2O_2 \xrightarrow{h\nu} 2\ OH \qquad (6)$$

is nearly an order of magnitude greater than other combined gas phase loss processes. Assuming reaction (1) is the dominant source of H_2O_2, the relationship

$$\left\{[HO_2]^2\right\}_{24\text{-hr ave}} = \frac{J_6 \cdot [H_2O_2]}{k_o + k' \cdot [M]} \qquad (7)$$

can be established between [HO_2] and [H_2O_2], where J_6 is the photolysis rate of H_2O_2. This relationship is sensitive to $k_o + k' \cdot [M]$, the rate coefficient of $HO_2 + HO_2$.

We tested our understanding of H_2O_2 – HO_x photochemistry by comparing calculations using a constrained photochemical steady state model with observed profiles of H_2O_2. Profiles of H_2O_2, shown in Figure 2.4, were obtained by two balloon-borne Fourier transform spectrometers: the Harvard-Smithsonian FIRS-2 instrument that senses H_2O_2 thermal emission from 80 cm^{-1} to 170 cm^{-1} [14] and the JPL MkIV instrument that uses mid-IR solar occultation.[15]

Three sets of model calculations are shown in Figure 2.4 to illustrate the sensitivity of calculated H_2O_2 to certain kinetic parameters that govern HO_x. The model calculations were constrained by measurements of temperature, O_3, H_2O, CH_4, NO_y, and Cl_y as well as profiles of sulfate aerosol surface area appropriate for the time of measurement[15] (K. W. Jucks et al., manuscript in preparation, 2002). One calculation, denoted JPL00-3, used the current recommended rate constants.[16] A second calculation, denoted Model A, used JPL00-3 rate coefficients and the rate of $HO_2 + HO_2$ from this study. A third calculation, denoted Model B, is identical to Model A except rate constants from the JPL97-4 evaluation were used for $O_3 + OH$ (denoted reaction (8)) and $O_3 + HO_2$ (denoted reaction (9)). From the upper troposphere to the middle stratosphere, the partitioning of HO_x is mainly controlled by reactions (8) and (9). These reactions affect calculated $[HO_2]$, and therefore $[H_2O_2]$ via the $HO_2 + HO_2$ reaction. We include reactions (8) and (9) in our sensitivity study because the recommended rates have recently changed. We note that at low temperatures, JPL97-4 rates for these reactions lead to lower calculated $[HO_2]$ and better agreement with measured $[HO_2]/[OH]$ in the lower stratosphere.[17]

Use of the new rate for $HO_2 + HO_2$ (Models A and B) in the photochemical simulation leads to significantly better agreement with measured H_2O_2 than is found using JPL00-3 kinetics (Figure 2.4). Changes to the rates of reactions (8) and (9) have a smaller effect on calculated H_2O_2 than the effect due to using the new rate of $HO_2 + HO_2$. Nonetheless, use of JPL97-4 rates for reactions (8) and (9) together with the new rate for $HO_2 + HO_2$ leads to slightly better overall agreement with measured H_2O_2 than is found using JPL00-3 rates for reactions (8) and (9). Because our new rate for $HO_2 + HO_2$ differs

from the current recommendation mainly at low temperatures, the impact on model calculations will be small for both the middle troposphere and the upper stratosphere. The comparisons in Figure 2.4 suggest that, using the new rate coefficient for $HO_2 + HO_2$, the kinetics governing the production and loss of H_2O_2 are well understood and that remote measurements of $[H_2O_2]$ can therefore be used to infer stratospheric $[HO_x]$ and place strong constraints on upper tropospheric $[HO_x]$.

Acknowledgements. This work was supported by the NASA Upper Atmosphere Research and Tropospheric Chemistry Programs and the NASA Graduate Student Researchers Program (GRSP). We wish to thank The National Scientific Balloon Facility (NSBF), Palestine, TX, for use of their facility and resources for the MkIV and FIRS-2 instruments. We also wish to thank D. J. Jacob and F. Ravetta for insight into the effect of k_1 on tropospheric chemistry, J. S. Francisco and J. C. Hansen for calculations regarding hydrogen-bonding between methanol and HO_2, and D. B. Natzic for his invaluable experimental contributions. This research was carried out at the Jet Propulsion Laboratory, California Institute of Technology, under contract with the National Aeronautics and Space Administration.

2.5 References

1. Wallington, T. J., K. W. Jucks, et al. "Upper Limits for the Gas-Phase Reaction of H_2O_2 with O_3 and NO. Atmospheric Implications." Int. J. Chem. Kinet. 30: 707-709 (1998).

2. DeMore, W. B., S. P. Sander, et al. (1997). Chemical Kinetics and Photochemical Data for Use in Stratospheric Modeling, Evaluation Number 12. Pasadena, CA, Jet Propulsion Laboratory, California Institute of Technology.

3. Atkinson, R., D. L. Baulch, et al. "Evaluated Kinetic and Photochemical Data for Atmospheric Chemistry, Organic Species: Supplement VII." J. Phys. Chem. Ref. Data 26: 1329-1499 (1997).

4. Lii, R.-R., R. A. Gorse, Jr. , et al. "Temperature Dependence of the Gas-Phase Self-Reaction of HO_2 in the Presence of NH_3." J. Phys. Chem. 84: 813-817 (1980).

5. Kircher, C. C. and S. P. Sander "Kinetics and Mechanism of HO_2 and DO_2 Disproportionations." J. Phys. Chem. 88: 2082-91 (1984).

6. Andersson, B. Y., R. A. Cox, et al. "The Effect of Methanol on the Self Reaction of HO_2 Radicals." Int. J. Chem. Kinetics 20: 283-295 (1988).

7. Tyndall, G. S., R. A. Cox, et al. "Atmospheric Chemistry of Small Organic Peroxy Radicals." J. Geophys. Res. 106: 12157-12182 (2001).

8. Curtis, A. R. and W. P. Sweetenham (1987). FACSIMILE/CHEKMAT, H015 ed. Harwell: Oxfordshire (UK).

9. Lightfoot, P. D., B. Veyret, et al. "Flash Photolysis Study of the $CH_3O_2 + HO_2$ Reaction between 248 and 573 K." J. Phys. Chem. 94: 708-714 (1990).

10. Takacs, G. A. and C. J. Howard "Temperature Dependence of the Reaction $HO_2 + HO_2$ at Low Pressures." J. Phys. Chem. 90: 687-690 (1986).

11. Dobis, O. and S. W. Benson "Reaction of the Ethyl Radical with Oxygen at Mmillitorr Pressures at 243-368 K and a Study of the $Cl + HO_2$, Ethyl + HO_2, and $HO_2 + HO_2$ reactions." J. Am. Chem. Soc. 115: 8798-8809 (1993).

12. Maricq, M. M. and J. J. Szente "A Kinetics Study of the Reaction Between Ethylperoxy Radicals and HO_2." J. Phys. Chem. 98: 2078-2082 (1994).

13. Mozurkewich, M. and S. W. Benson "Self-Reaction of HO_2 and DO_2: Negative Temperature Dependence and Pressure Effects." Int. J. Chem. Kinet. 17: 787-807 (1985).

14. Jucks, K. W., D. G. Johnson, et al. "Observations of OH, HO_2, H_2O, and O_3 in the Upper Stratosphere: Implications for HO_x photochemistry." Geophysical Research Letters 25: 3935-3938 (1998).

15. Sen, B., G. C. Toon, et al. "Measurements of Reactive Nitrogen in the Stratosphere." Journal of Geophysical Research-Atmospheres 103: 3571-3585 (1998).

16. Sander, S. P., R. R. Friedl, et al. (2000). Chemical Kinetics and Photochemical Data for Use in Stratospheric Modeling, Evaluation Number 13. Pasadena, CA, Jet Propulsion Laboratory, California Institute of Technology.

17. Lanzendorf, E. J., T. F. Hanisco, et al. "Establishing the Dependence of $[HO_2]/[OH]$ on Temperature, Halogen Loading, O_3, and NO_x Based on in Situ Measurements from the NASA ER-2." J. Phys. Chem. A 105: 1535-1542 (2001).

Table 2.1. Experimental Conditions.

HO_2 Source	$[Cl_2]$ 10^{15} cm^{-3}	$[F_2]$ 10^{16} cm^{-3}	$[CH_3OH]$ 10^{14} cm^{-3}	$[H_2]$ 10^{17} cm^{-3}	$[O_2]$ 10^{18} cm^{-3}	$[N_2]$ 10^{18} cm^{-3}
$Cl + CH_3OH \rightarrow HCl + CH_2OH$ $CH_2OH + O_2 \rightarrow HO_2 + CH_2O$	9-11		2-130		1.2-1.4	1.8-2
$F + H_2 \rightarrow HF + H$ $H + O_2 + M \rightarrow HO_2 + M$		7.5-8.5		3-20	0.3-2	0.5-1.5
Purities (All gases from AirProducts)	99.5%	97.0%	HPLC J.T. Baker	99.999%	99.996%	99.9993%

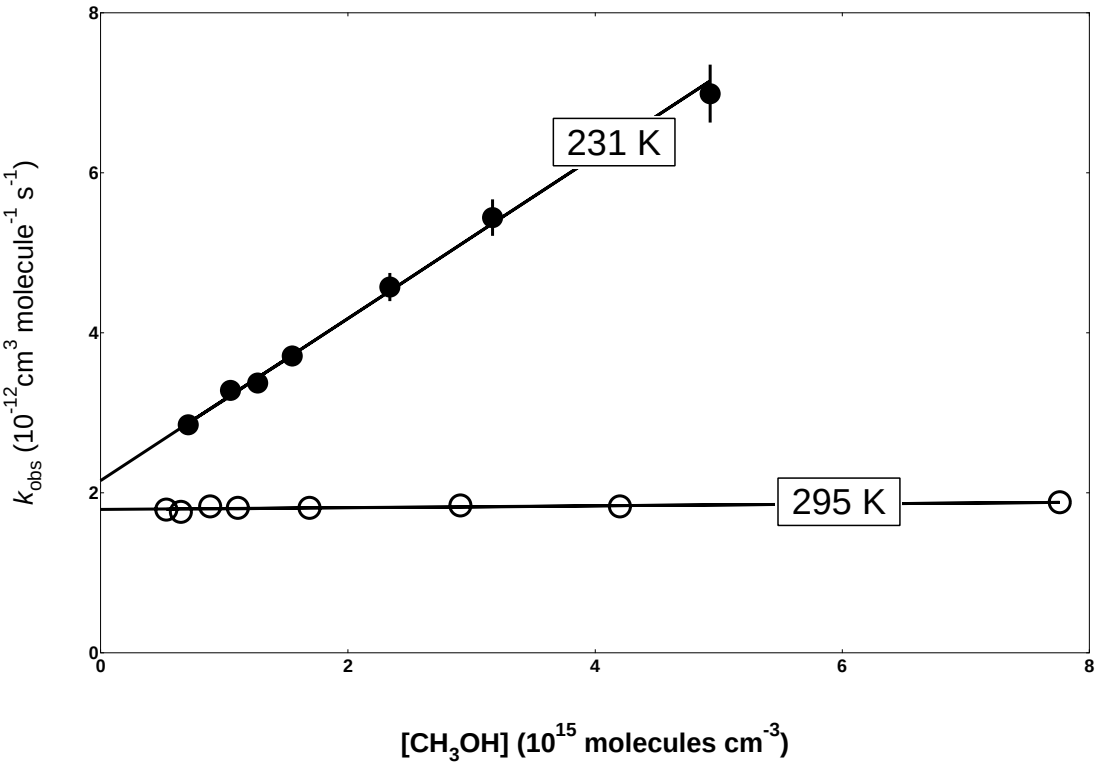

Figure 2.1. Plot of k_{obs} as a function of [CH_3OH] at 231 K (●) and 295 K (○). Error bars represent 2σ uncertainties in the measurement precision (see text).

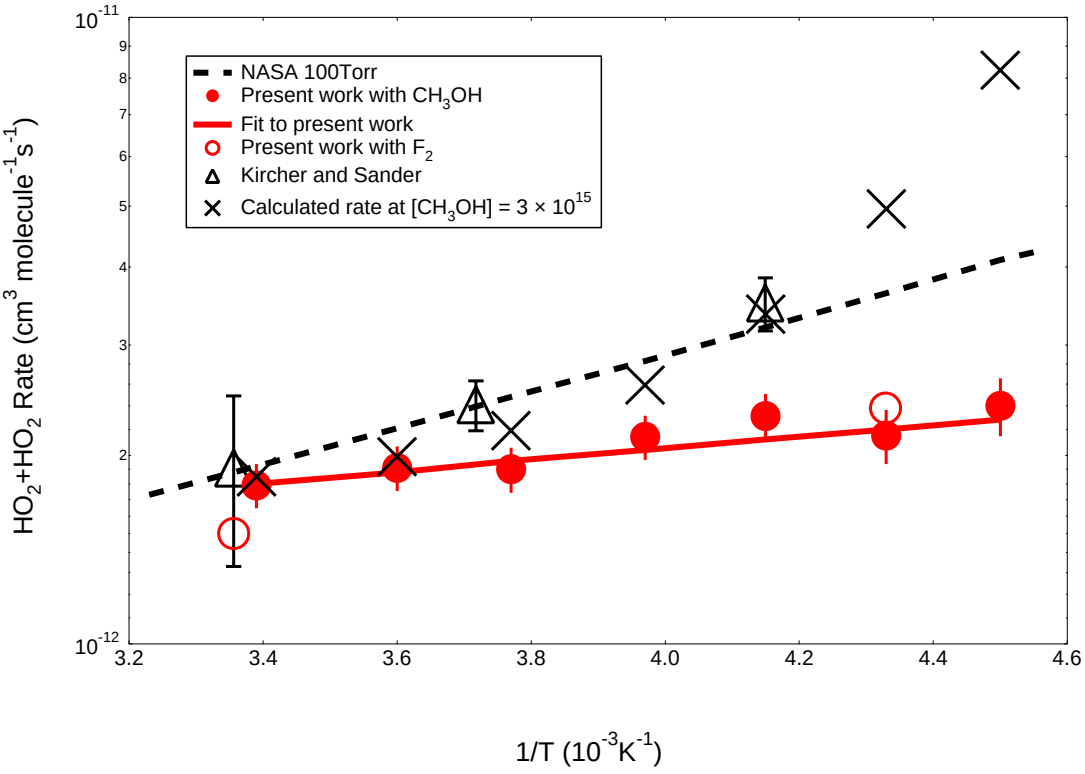

Figure 2.2. Plot of the rate constant of reaction (1) as a function of inverse temperature at 100 Torr. Filled circles are k_1 values from experiments using $Cl_2/CH_3OH/O_2/N_2$ at 100 Torr. The solid line is the fit to these values. Values of k_1 obtained using $F_2/H_2/O_2/N_2$ are denoted by open circles. The dashed line is the JPL00-3 recommendation for k_1 at 100 Torr. Also shown are calculated k_{obs} values using k_1 and k'' measured in the present study and $[CH_3OH] = 3 \cdot 10^{15}$ molecules cm^{-3} denoted by (×). The results of *Kircher and Sander* are represented by (Δ). Error bars (2σ) for *Kircher and Sander* are capped. Error bars for the present study are not capped.

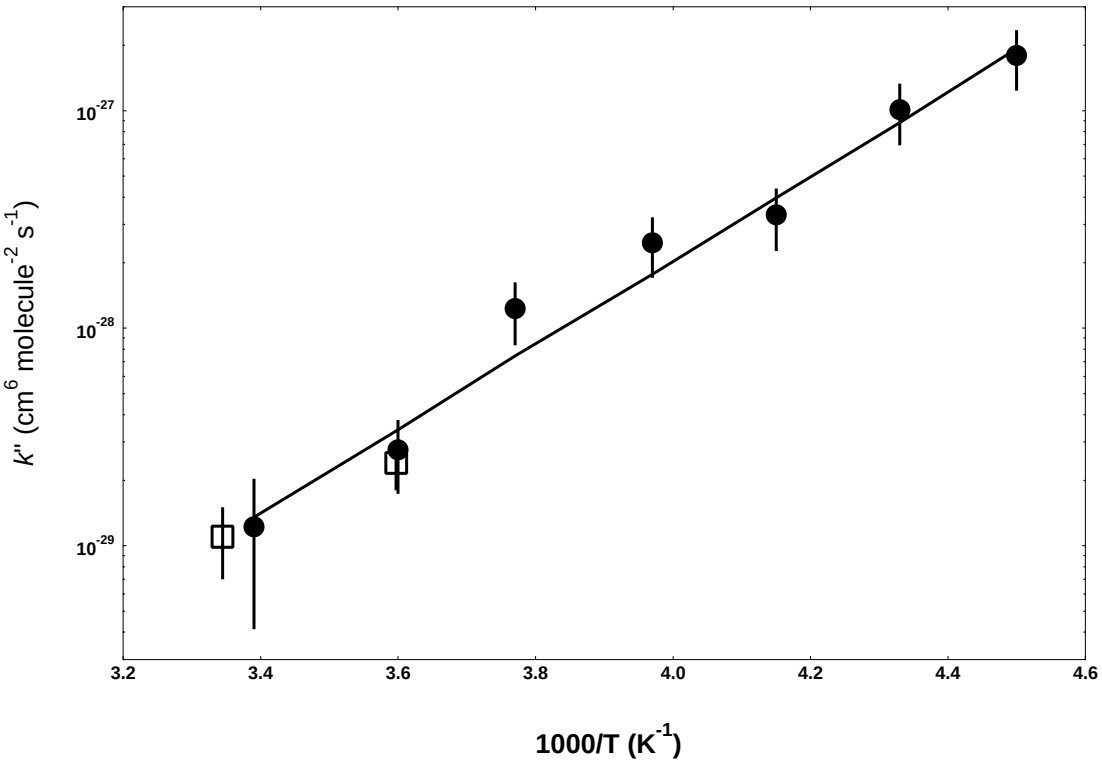

Figure 2.3. Plot of k'' as a function of inverse temperature from the present study at 100 Torr (●) and from the *Andersson et al.* study at 760 Torr (□). Error bars are 2σ.

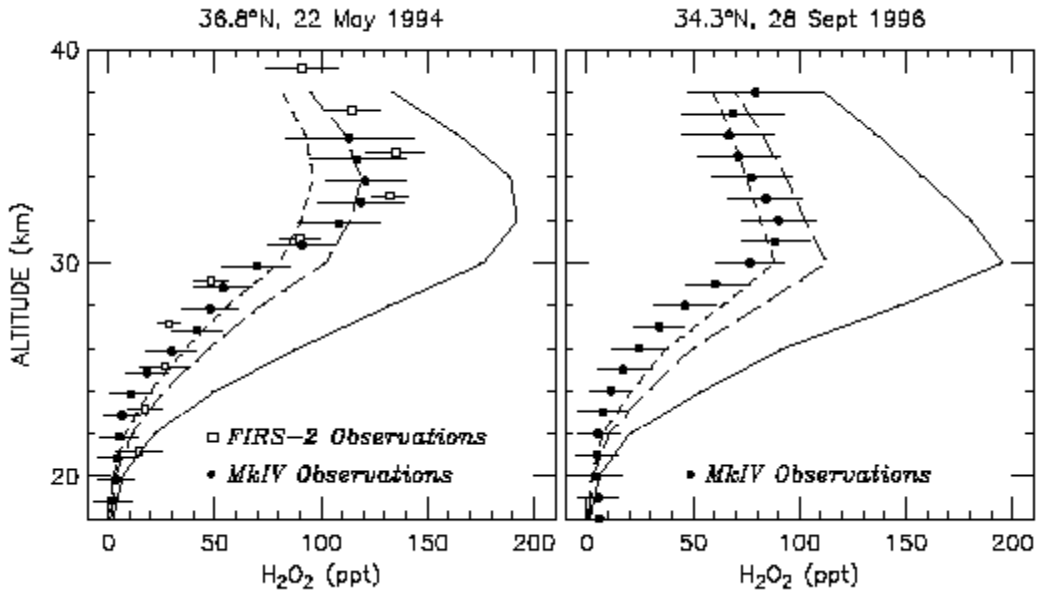

Figure 2.4. Measured and modeled profiles of H_2O_2 VMR for two seasons near Ft. Sumner, NM (34.5°N), as indicated at the top of each panel. Error bars represent 1σ uncertainty for the measured profiles. The solid lines show calculated [H_2O_2] profiles using JPL00-3 kinetics (Model JPL00-3). The long dashed lines show profiles found using the new rate coefficient for $HO_2 + HO_2$ and JPL00-3 kinetics for all other reactions (Model A). The short dashed lines show profiles using the new rate coefficient for $HO_2 + HO_2$, JPL97-4 coefficients for $OH + O_3$ and $HO_2 + O_3$, and JPL00-3 kinetics for all other reactions (Model B). The left and right panels depict results for spring and fall, respectively.

Chapter 3: The Methanol Chaperone Effect on HO_2 Reactions

3.1 Introduction

The $HO_2 + HO_2$ reaction plays an important role in combustion and atmospheric chemistry. HO_2 is an intermediate in the oxidation of hydrocarbons, and its self-reaction is the primary source of H_2O_2 in the stratosphere and upper troposphere.

Laboratory experiments have demonstrated that the observed rates of the $HO_2 + HO_2$ and $HO_2 + NO_2 + M$ reactions are enhanced in the presence of H_2O, NH_3, and CH_3OH.[1-6] This enhancement has been attributed to the formation of the hydrogen-bonded complex $HO_2 \cdot X$, where X = H_2O, NH_3, or CH_3OH. It is assumed that the $HO_2 \cdot X$ complex is more reactive towards other species, such as HO_2 and NO_2, than uncomplexed HO_2. Under typical laboratory conditions, the formation and dissociation of the complex is believed to be essentially instantaneous in comparison to the loss of HO_2 due to chemical reaction; therefore, equilibrium is established between HO_2, X, and $HO_2 \cdot X$. If the equilibrium assumption is made, then the ratio of $[HO_2 \cdot X]$ to $[HO_2]$ increases linearly with the concentration of X. In effect, by the formation of a hydrogen-bonded complex, X "chaperones" HO_2, making it more reactive towards other species. This is often termed the "chaperone effect."

This chapter presents experimental evidence for the formation of the $HO_2 \cdot CH_3OH$ complex. By measuring the time dependence of the HO_2 signal in a laser-photolysis

experiment, we directly observed the establishment of equilibrium between CH_3OH, HO_2 and $HO_2 \cdot CH_3OH$ and determined the equilibrium constant at temperatures between 231 K and 261 K and at 50 and 100 Torr. We measured the rate coefficient for the HO_2 + CH_3OH + M reaction and inferred the dissociation rate of the $HO_2 \cdot CH_3OH$ complex. The complex mechanism is further supported by comparisons of our experimental results with ab initio calculations for the binding energy and geometry of $HO_2 \cdot CH_3OH$ made at the MP2 and CCSD(T) levels of theory. Furthermore, we measured the observed rate coefficient for the HO_2 self-reaction as a function of methanol concentration simultaneously with UV an IR spectroscopy. From these measurements, we determined rate coefficients for the HO_2 + $HO_2 \cdot CH_3OH$ and $HO_2 \cdot CH_3OH$ self-reaction.

3.2 Experimental

The experimental apparatus is described in Chapters 1 and 5. Briefly, a 308 nm, 100 mJ/pulse excimer laser was used to photolyze either Cl_2 or F_2, initiating chemical reactions in a temperature controlled reaction cell. IR and UV light sources probed the temporal dependence of species within the reaction cell.

An IR beam emitted from a distributed feedback diode laser monitored the temporal behavior of HO_2 formed within the reaction cell. The diode laser probed a group of blended ro-vibrational HO_2 transitions near 6638.2 cm^{-1} associated with the OH overtone stretch ($2\nu_1$) and nominally assigned to the $^qQ_2$ band head. The diode laser was wavelength modulated, and 2f-Heterodyne detection was employed for the IR measurements. The signal was calibrated by simultaneously measuring the second-order rate coefficient of the HO_2 self-reaction with IR and UV probes, as described in Chapter

1. Briefly, photolysis of F_2-H_2-O_2-N_2 gas mixtures was used to generate HO_2. Using this method of HO_2 generation, problems from complex formation between HO_2 and other species present in the reaction cell were minimized. The measurement of the time-dependent UV signal at 220 nm, corrected to give the HO_2 concentration, provided a rate coefficient in units of cm^3 $molecule^{-1}$ s^{-1} while the IR measurement determined a rate coefficient in units of V^{-1} s^{-1}. The ratio of the rate constants provided the scaling factor that was used to convert the IR signal, in Volts, to molecules cm^{-3}.

The IR signal was sensitive only to HO_2. This was verified by studying the HO_2 self-reaction using three distinct ro-vibrational HO_2 transitions between 6625 cm^{-1} and 6638.2 cm^{-1}. No significant discrepancies in the temporal dependence of the HO_2 signal were observed. Also, direct measurements of HCl, H_2O_2, and CH_2O ruled out their contributions in this spectral region. Methanol does absorb in this spectral region, but its 2f signal was insignificant at 6632.8 cm^{-1}. We found no evidence for absorption by $HO_2 \cdot CH_3OH$ at 6638.2 cm^{-1}, nor was it expected. Ab initio calculations of the $HO_2 \cdot CH_3OH$ complex, indicated that most of the hydrogen-bonding occurred between the terminal H atom of HO_2 and the O atom of CH_3OH.[7] The effect of hydrogen bonding on overtone transitions is typically to decrease the intensity and shift the transition to lower frequency.[8] Ab initio calculations have indicated that for the $HO_2 \cdot H_2O$ complex, a red shift of around 300 cm^{-1} is expected for the O-H stretch.[9] Thus, the overtone band of the complex should be shifted completely out of the frequency range of the diode laser.

The UV beam from a D_2 lamp measured the change in absorbance at 220 nm, which was mainly due to HO_2 and H_2O_2. However, it is possible that the $HO_2 \cdot CH_3OH$ complex would also absorb at this wavelength. The UV light excited the $2\,^2A'' \leftarrow X\,^2A''$

transition of HO_2. Ab initio calculations have indicated that the analogous transition in the complex would be red-shifted by approximately 60 nm.[10] To date, the UV spectrum of the complex has not been experimentally observed. In previous studies of the methanol enhancement of the HO_2 self-reaction, it was noted that the dependence of the observed rate coefficient on methanol concentration was consistent with the assumption that HO_2 and the complex had similar UV cross sections at 220 nm. Similar arguments were made for the UV absorption of the $HO_2 \cdot NH_3$ and $HO_2 \cdot H_2O$ complexes as well. However, these inferences are indirect, and no quantitative data yet exists on the relative magnitudes of the UV cross sections of HO_2 and any $HO_2 \cdot X$ complex.

All kinetic modeling discussed in this paper utilized the FACSIMILE modeling program.[11] The FACSIMILE program was used to evaluate the impact of possible secondary reactions on the data analysis, rather than to determine any experimental parameters. It was also used to verify the analytical expressions derived for the time dependence of the HO_2 signal as well as the analytical expressions derived for the observed rate constant for the HO_2 self reaction for the IR and UV channels. The chemical reactions used in the kinetic modeling are listed in Table 3.1. The sources for the values of the rate coefficients are also listed in the table. Most of the rate coefficient values were taken from the 1997 NASA compendium.[12]

For this work, two different methods of HO_2 generation were employed. The methods differed in which halogen species was photolyzed and which reagents were employed for HO_2 formation.

In the first approach, photolysis of F_2-H_2-O_2-N_2 gas mixtures was used to calibrate the IR signal and to confirm the trend of the observed rate of $HO_2 + HO_2$ with methanol. The HO_2 formation chemistry is as follows:

$$F_2 \xrightarrow{h\nu} 2\,F \qquad (1)$$

$$F + H_2 \longrightarrow HF + H \qquad (2)$$

$$H + O_2 \xrightarrow{M} HO_2 \qquad (3)$$

Table 3.2 lists the gas concentrations employed. The effect of secondary formation of FO_2 via $F + O_2 + M$ on the UV signal was considered, because FO_2 absorbs strongly in the UV and the dissociation of FO_2 into $F + O_2$ is thought to be in the range of 40 s^{-1} to 80 s^{-1} at 300 K and 100 Torr.[12] Thus, FO_2 could contribute to a UV signal that decayed on the timescale of the HO_2 self-reaction in the present experiment. However, the effect of FO_2 could be neglected for three reasons. First, we found good agreement between the measured IR and UV rate coefficients for the HO_2 self-reaction. If there were spectral interference in the UV channel, the IR and UV measurements would differ. Second, the residual absorption in the UV was constant after the self-reaction had completed and consistent with the formation of H_2O_2 product from the HO_2 self-reaction. Finally, at the highest ratio of $[O_2]/[H_2]$ employed, $[O_2]/[H_2] = 3$, the maximum fraction of F atoms predicted to react with O_2 as opposed to H_2 (based on the rate coefficients in the 1997 NASA compendium for $F + O_2 + M$ and $F + H_2$) at $[O_2]/[H_2] = 3$, was approximately 0.2% at 300 K and 0.5% at 230 K. This amount of FO_2 would not contribute significantly

to the UV absorption, nor would it affect the time dependence of $[HO_2]$ through secondary chemistry.

F and H atom concentrations were high at early times. However, kinetic modeling determined that under typical conditions used in the fluorine chemistry, reactions of these atoms with HO_2 could be neglected. The time constant for HO_2 formation was in the μs regime and the time constant for F disappearance was in the 100 ns regime. Because $[H_2] >> [HO_2]$, possible complications arising from $F + HO_2$ were determined to be minimal. During the first 20 μs, H atoms co-exist with HO_2 due to the reaction $F + H_2 \rightarrow HF + H$. The pseudo-first-order rate of H consumption by O_2 was approximately 2×10^5 s^{-1} at 100 Torr. Kinetic modeling determined that the $H + HO_2$ reaction was unimportant.

For most of the experiments discussed in the present work, the second method for HO_2 generation, by photolysis of Cl_2-CH_3OH-O_2-N_2 gas mixtures, was employed. The reaction sequence is as follows:

HO_2 formation

$$Cl_2 \xrightarrow{h\nu} 2\,Cl \qquad (4)$$

$$Cl + CH_3OH \longrightarrow HCl + CH_2OH \qquad (5)$$

$$CH_2OH + O_2 \longrightarrow HO_2 + CH_2O \qquad (6)$$

Complex formation/ dissociation

$$CH_3OH + HO_2 \underset{M}{\overset{M}{\rightleftharpoons}} CH_3OH \cdot HO_2 \qquad (7,-7)$$

HO_2 and $HO_2 \cdot CH_3OH$ chemical loss

$$HO_2 + CH_3OH \cdot HO_2 \longrightarrow \text{Products} \qquad (8)$$

$$HO_2 \cdot CH_3OH + HO_2 \cdot CH_3OH \longrightarrow \text{Products} \qquad (9)$$

$$HO_2 + HO_2 \xrightarrow[\text{ter-molecular}]{\text{bi-molecular}} H_2O_2 + O_2 \qquad (10)$$

Table 3.2 lists the gas concentrations employed. The values of the rate coefficients for the reactions listed above are given in Table 3.2. The values for reactions (1) through (6) were taken from the 1997 NASA compendium[12] and the value for reaction (10) was taken from Chapter 2. The rate coefficient values for reactions (7) through (9) were measured in the present study. The concentrations of O_2 and CH_3OH were sufficiently high in comparison to other reactive species so that bi-molecular reactions involving either O_2 or CH_3OH could be considered as pseudo-first-order.

There are three main kinetic processes to consider in the above reaction scheme: HO_2 formation via reactions (5) and (6); complex formation and dissociation via reactions (7) and (-7); and total HO_2 and $HO_2 \cdot CH_3OH$ loss via reactions (8), (9) and (10).

Complications from reactions not listed in the scheme above were considered insignificant. The effect of the Cl + HO_2 reaction was negligible because of three reasons: first, most Cl atoms had reacted with CH_3OH before HO_2 concentrations became appreciable; second, $[CH_3OH] >> [HO_2]$, so virtually all Cl atoms reacted with CH_3OH; third, k_5 is within an order of magnitude of the collision limit. Kinetic modeling demonstrated that the Cl + HO_2 reaction accounted for less than 0.1% of the loss of Cl at $[CH_3OH] = 1 \times 10^{16}$ molecules cm^{-3} at all temperatures when the NASA recommend values[12] for the Cl + HO_2 reaction were used. Kinetic modeling also showed that the reaction between HO_2 + CH_2OH was insignificant, because the O_2 + CH_2OH rate coefficient is large and also $[O_2] >> [HO_2]$.

For both photolysis schemes, secondary products are formed that can potentially form a hydrogen-bond with HO_2. For F_2-photolysis, every F atom produced results in one

HF molecule formed. For Cl_2-photolysis, every Cl atom results in one CH_3OH lost, and one HCl and CH_2O gained. For both schemes, H_2O_2 is a product of the subsequent reactions of HO_2. If it is assumed that HF, HCl, CH_2O, and H_2O_2 have the same rate enhancing effect as CH_3OH, then the calculated enhancement due to secondary product formation, at 231 K, 100 Torr, and $[Cl]_o = [F]_o = 8 \times 10^{13}$ atoms cm^{-3}, is less than 8%, based on prior measurements of the rate enhancement due to methanol, explained in Chapter 2. This calculation assumed the value of $[H_2O_2]$ from the completed $HO_2 + HO_2$ reaction. No corrections were made to any measured parameters due to possible rate enhancement from secondary products in the present work.

This paper discusses three distinct sets of direct measurements: measurements of the equilibrium constant between HO_2, CH_3OH, and $HO_2 \cdot CH_3OH$, denoted K_c, where the subscript "c" refers to the fact that it is expressed in terms of concentration as opposed to pressure; measurements of k_7; and measurements of the observed rate coefficient for the HO_2 self-reaction as a function of methanol concentration, denoted k_{obs}. The term "observed" refers to that fact that $\frac{d[HO_2]}{dt}$ and $\frac{d\{[HO_2]+[HO_2 \cdot CH_3OH]\}}{dt}$, the loss rates for the IR and UV probes, respectively, are the aggregate of reactions (7) through (10).

Values for K_c were obtained by measuring the change in the equilibrium $[HO_2]$ as a function of $[CH_3OH]$ using IR detection. These measurements were conducted within the first 50 μs after photolysis. Measurements of k_7 were conducted at different temperatures and pressures using IR detection. These measurements were also conducted within the first 50 μs after photolysis. The values of k_7 and K_c where used to derive k_{-7}. The UV probe was not utilized for measurements of K_c and k_7 due to scattered light from

the excimer pulse, which saturated the PMT. The PMT signal was adversely affected until 200 μs to 400 μs after the photolysis event. Measurements of k_{obs} as a function of methanol concentration used simultaneous IR and UV spectroscopy. These measurements were conducted between 200 μs and 38 ms after photolysis. From these measurements, the rate coefficients k_8 and k_9 were indirectly obtained.

A SRS SR560 low-noise preamplifier with a low-pass filter was used to provide gain to the demodulated signal. The low-pass filters had maximum bandwidths of 1 MHz and were not utilized for measurements of K_c and k_7. It was observed experimentally that for a gain of 1000, which was the setting utilized for all experiments discussed in this paper, the inherent low-pass bandwidth of the preamplifier circuitry was approximately 2 MHz (3dB point). Further, there was a phase-shift that imposed a measured delay of approximately 500 ns upon the signal entering the preamplifier. For measurements of k_{obs}, the low-pass filters were set at the sampling rate of the data acquisition card housed inside the computer. The trigger came from a voltage drop induced by the excimer light impinging on a photodiode. The cable from the photodiode to the trigger input of the data acquisition card was approximately 2 meters. It was assumed that the time between the photolysis event and when the data acquisition card received the trigger signal was less than 50 ns.

After passing through the preamplifier, the signal was digitized at 16 bits of precision by a Gage Compuscope 1602 data acquisition card. The bandwidth of the sample and hold amplifier on the card was 1.25 MHz. For measurements of K_c and k_7, data were sampled at the highest rate possible, 2.5 MS s^{-1}, or a sampling interval of 400 ns. For measurements of k_{obs}, data were sampled between 20 kHz and 100 kHz.

3.3 Measurements of K_c

Measurements of K_c employed the Cl_2-CH_3OH-O_2-N_2 system for HO_2 generation. A typical example of the influence of methanol on the HO_2 signal is shown in Figure 3.1 for experiments conducted at 251 K at different CH_3OH concentrations. The figure demonstrates that the average signal between 20 μs and 50 μs, was greater at low [CH_3OH]. The decrease in the HO_2 signal upon addition of CH_3OH was due to a shift in the equilibrium concentrations of HO_2 and $HO_2 \cdot CH_3OH$. Addition of CH_3OH promotes the formation of $HO_2 \cdot CH_3OH$ at the expense of HO_2.

The change in [HO_2] between 20 μs and 50 μs was observed to be less than 5% under all conditions. This indicated that the loss of [HO_2] due to reactions (8), (9), and (10) was less than 5% during the first 50 μs after photolysis. Subsequent kinetic modeling of the system using the measured values for reactions (8) and (9), given below, verified that the loss of HO_2 was less than 5% during this time period. By 20 μs, HO_2 formation was observed to be complete under all experimental conditions. This was verified by calculating the time constant for HO_2 formation at the lowest [CH_3OH] employed. This calculation yielded $\{k_5(3 \times 10^{15} \text{ molecules cm}^{-3})\}^{-1} = 6$ μs. HO_2 was observed to be in equilibrium with CH_3OH and $HO_2 \cdot CH_3OH$ by 20 μs, based on the constant [HO_2] between 20 μs and 50 μs. The assumption that equilibrium was established by 20 μs was verified by measuring the rate coefficient for $HO_2 + CH_3OH + M$. It will be shown below that the first order rate constant for the establishment of equilibrium is approximately $\{k_7 \cdot [CH_3OH] + k_{-7}\}$. The rate constant can be re-written as $k_7\{[CH_3OH] + K_c^{-1}\}$. From measurements of K_c and k_7, discussed below, $\{[CH_3OH] + K_c^{-1}\} > 2 \times 10^{16}$ molecules

cm^{-3} and $k_7 \sim 4 \times 10^{-12}$ cm^3 $molecule^{-1}$ s^{-1}. Therefore $k_7\{[CH_3OH] + K_c^{-1}\}$, the rate at which equilibrium is established, was greater than 8×10^4 s^{-1}. This was equivaltent to a time constant of approximately 13 μs.

A simplified kinetic scheme can be written for the establishment of equilibrium during the first 50 μs after photolysis. Assuming the loss of $\{[HO_2] + [HO_2 \cdot CH_3OH]\}$ via reactions (8), (9), and (10) is negligible, the kinetics of HO_2 formation and subsequent kinetics of the formation and dissociation of $HO_2 \cdot CH_3OH$ can be simplified as follows:

$$Cl \xrightarrow{a} HO_2 \underset{-b}{\overset{b}{\rightleftharpoons}} HO_2 \cdot CH_3OH \qquad (11)$$

where $k_a \approx k_5 \cdot [CH_3OH]$ for $[CH_3OH] < 0.1 \times [O_2]$, which was true for all experiments, $k_b = k_7 \cdot [CH_3OH]$, and $k_{-b} = k_{-7}$. In effect, Cl atoms are transformed into $\{[HO_2] + [HO_2 \cdot CH_3OH]\}$ and the partitioning of $[HO_2]$ and $[HO_2 \cdot CH_3OH]$ is determined by K_c. The time dependence for $[HO_2]$ can be expressed as

$$[HO_2] = [Cl]_o \left(\frac{k_{-b}}{\lambda} + \frac{k_{-b} - k_a}{k_a - \lambda} e^{-k_a t} + \frac{k_a k_b}{\lambda(k_a - \lambda)} e^{-\lambda t} \right) \qquad (12)$$

where $\lambda = k_b + k_{-b}$. The condition $[HO_2]/dt = 0$ exists at $t = \ln[k_b/(k_a - k_{-b})]/(\lambda - k_a)$. This implies that in order for there to be an observable maximum HO_2 signal, $[CH_3OH] > k_{-7}/k_5$, that is, the concentration of methanol has to be sufficiently high. As can be seen in Figure 3.1, at sufficiently high $[CH_3OH]$, a non-equilibrium system was clearly

established within a few μs in which $[HO_2] > [HO_2]_{eq}$. The system then "relaxed" towards equilibrium on the timescale of several μs.

At a given temperature, $[HO_2]_{eq}$ was measured as a function of $[CH_3OH]$. Let $[HO_2]_{eq,o}$ represent $[HO_2]_{eq}$ in the limit of zero added methanol. The following formula can used to relate $[HO_2]_{eq,o}$ to $[CH_3OH]$, enabling the determination of $[HO_2]_o$:

$$\left\{[HO_2]_{eq}\right\}^{-1} = K_{eq} \cdot \left\{[HO_2]_{eq,o}\right\}^{-1} \cdot [CH_3OH] + \left\{[HO_2]_{eq,o}\right\}^{-1} \qquad (13)$$

From a linear fit, the value of $[HO_2]_{eq,o}$ is obtained. Equation (13) can be re-written as

$$\frac{[HO_2]_{eq,o}}{[HO_2]_{eq}} = 1 + K_{eq}[CH_3OH] \qquad (14)$$

The slope of equation (14) gives K_c. Plots of $[HO_2]_{eq,o}/[HO_2]_{eq}$ versus $[CH_3OH]$ are shown in Figure 3.2 for experiments done at 231 K and 261 K. The value of K_c was measured at 231 K, 240 K, 251 K, and 261 K. At each temperature, between 10 and 15 observations were used to infer K_c. The measured values for K_c (T) are listed in Table 3.3.

The van't Hoff equation was used to infer ΔH and ΔS from a weighted fit of $K_p(T)$ versus T using the equation $K_p(T) = A \cdot \exp(\Delta H/RT)$. $K_p(T) = K_c(T) \cdot (6.022 \times 10^{20}$ molecules L mol^{-1} cm$^{-3}) \cdot (RT)^{-1}$, where $R = 0.0821$ L atm mol^{-1} K^{-1}. From the fit, the obtained values were $A = (1.0 \pm 1.0) \times 10^{-5}$ L mol^{-1} and $\Delta H = (-36 \pm 3)$ kJ mol^{-1}. The value of A translates to $\Delta S = (-96 \pm 96)$ J mol^{-1} K^{-1}.

The uncertainty (1σ) in determining $[HO_2]_o$ ranged from 3% at 231 K to approximately 20% at 261 K. Error due to inaccurate calibration of the IR signal was insignificant because the calibration factor is ratioed out of equations (13) and (14). The combined uncertainty in the knowledge of the vapor pressure of CH_3OH, the flow of gas through the bubbler, and the temperature of the liquid bath in which the bubbler was placed was approximately 5% at all temperatures. The uncertainty in determining $[HO_2]_{eq}$ due to noise in the IR signal was approximately 3-5% of $[HO_2]_{eq,o}$. Uncertainty in the accuracy of K_c due to temperature was 8% at 231 K, and 6% at 261 K. When added in quadrature, the final uncertainty for $K_c(T)$ was between 10% and 20%.

3.4 Measurements of k_7 and k_{-7}

The values of k_7 and k_{-7} were derived from a subset of the experimental data used to determine K_c. Only experiments in which the decrease in the HO_2 signal due to reaction (7) was more than five times greater than the standard deviation of $[HO_2]_{eq}$ were analyzed. Of the 57 individual observations, only 15 met this criterion.

As stated in the Experimental section, the preamplifier introduced a delay in signal digitization relative to the photolysis event that resulted in uncertainty in the knowledge of when the photolysis event occurred. Also, the resolution of the signal with respect to time was 400 ns. The expected rise times of HO_2 were on the order of 100 ns to several μs, which meant that attempts to fit the HO_2 time dependence with a kinetic model were subject to an error due to a lack of time resolution. Further, the first 1.2 μs of data after photolysis was heavily affected by noise associated with the excimer laser. To

address of these concerns, a simplified kinetic scheme was used to describe the time dependence of $[HO_2]$ as follows:

$$[HO_2] \underset{k_{-7}}{\overset{k_7 \cdot [CH_3OH]}{\rightleftharpoons}} [HO_2 \cdot CH_3OH] \qquad (15)$$

For such a scheme, the time dependence for $[HO_2]$ can be expressed as

$$[HO_2] = [HO_2]_o \left(\frac{k_7[CH_3OH]}{k_7[CH_3OH] + k_{-7}} \right) \left(1 - e^{-(k_7[CH_3OH] + k_{-7})} \right) \qquad (16)$$

where $[HO_2]_o$ represents $[HO_2]$ at time = 0. For equation (16) to be valid, loss of $[HO_2]$ and $[HO_2 \cdot CH_3OH]$ by reactions (8), (9), and (10) has to be insignificant and production of HO_2 via reactions (5) and (6) has to be complete before the signal was analyzed. The former condition was met by limiting the analysis to within 20 μs after photolysis. As discussed above for measurements of K_c, the decrease in the HO_2 signal between 20 μs and 50 μs was less than 5%. This indicated that loss of $[HO_2]$ and $[HO_2 \cdot CH_3OH]$ by reactions (8), (9), and (10) was insignificant. The time constant for HO_2 formation was calculated to be less than 1 μs for all individual experiments that qualified for analysis by equation (16). Because the start of fitting was at (1.6 ± 0.2) μs, that latter condition for analysis by equation (16) was met. The uncertainty in the time of fitting was due to the resolution of the measurements.

The values of k_7 and $[HO_2]_o$ were allowed to vary. The measured values of $[CH_3OH]$ and $[HO_2]_{eq}$ were held constant. The fitted value of $K_c(T)$ was used to replace

k_{-7} with k_7/K_c. This ensured that the fitting process was sensitive to k_7. Use of equation (16) removed errors associated with the sampling intervals that were much longer than the time for HO_2 formation. The value of $[HO_2]_o$ was not a meaningful quantity since it was an extrapolation. Fits were done between 1.6 μs and 20 μs. An example of a fit is shown in Figure 3.4 for 240 K, 100 Torr, and $[CH_3OH] = 9.1 \times 10^{16}$ molecules cm^{-3}. Measured values for k_7 at different pressures and temperatures are listed in Table 3.3. Errors due to uncertainty in the calibration of the IR signal were negligible because the calibration factor was ratioed out of equation (16).

3.5 Kinetic Measurements of k_{obs} as a Function of Methanol Concentration

In contrast to the measurements of K_c and k_7, conducted within the first 50 μs after photolysis, measurements of k_{obs} were done between 200 μs to 38 ms. In this time regime, HO_2, CH_3OH, and $HO_2 \cdot CH_3OH$ can be assumed to be in equilibrium because the time constant for the establishment of equilibrium was on the order of μs, as discussed in section 3.3, and the timescale of the observed HO_2 loss was on the order of milliseconds. Rate coefficients were obtained in both the UV and IR, and are denoted $k_{obs,ir}$ and $k_{obs,uv}$ respectively. Results for $k_{obs,uv}$ at 100 Torr and between 222 K and 298 K have been presented previously in Chapter 2. Comparisons between $k_{obs,ir}$ and $k_{obs,ir}$ are shown in Figure 3.5 for the temperatures 295 K and 241 K. Overall, it was observed that for $T \geq 241$ and $[CH_3OH] < 6 \times 10^{15}$ molecules cm^{-3}, $k_{obs,ir} \approx k_{obs,uv}$. It was observed that $k_{obs,ir}$ and $k_{obs,uv}$ were second-order under these same conditions. The criteria for being second-order was that the measured value of the rate coefficient not change by more than 10% between fits that were conducted from 250 μs to 10 ms and fits that were conducted from 250 μs

to 20 ms. Typical examples of data collected at 231 K and 100 Torr for both the IR and UV channels are shown in Figures 3.6.1 and 3.6.2. To aid in ascertaining the signal-to-noise, the span of the residual plots on the figures are 20% of the maximum signal acquired for each channel.

At 231 K, there were significant differences between the IR and UV measurements. As depicted in Figure 3.7, for $[CH_3OH] > 5 \times 10^{15}$ molecules cm^{-3}, the difference between $k_{obs,uv}$ and $k_{obs,ir}$ was greater than the scatter in the rate measurements, and $k_{obs,ir} > k_{obs,uv}$. It was observed that for $[CH_3OH] < 2 \times 10^{16}$ molecules cm^{-3}, $k_{obs,ir}$ met the criterion for second-order reactivity. However, at $[CH_3OH] \sim 5 \times 10^{15}$ molecules cm^{-3}, measurements of $k_{obs,uv}$ done over 10 ms were about 10% larger than those conducted over 20 ms. At $[CH_3OH] \sim 1 \times 10^{16}$ molecules cm^{-3}, measurements done over 10 ms were between 20% and 50% larger than those conducted over 20 ms. Figure 3.7 also indicates that $\frac{d^2 k_{obs,ir}}{d[CH_3OH]^2} > 0$ and $\frac{d^2 k_{obs,uv}}{d[CH_3OH]^2} < 0$.

As discussed in the above in the Experimental section, IR signal was assumed to measure only $[HO_2]$ while the UV measured $\{[HO_2] + [HO_2 \cdot CH_3OH]\}$. Previous investigators of the enhancement of the HO_2 self-reaction by NH_3 and H_2O have derived an expression for the dependence of $k_{obs,uv}$ on $[NH_3]$ and $[H_2O]$.[13] Following their example, $k_{obs,ir}$ and $k_{obs,uv}$ can be expressed as

$$k_{obs,ir} = \frac{k_{10} + k_8 \cdot K_c \cdot [CH_3OH] + k_9 \cdot K_c^{\,2} \cdot [CH_3OH]^2}{\left(1 + K_c \cdot [CH_3OH]\right)} \qquad (17)$$

$$k_{obs,uv} = \frac{k_{10} + k_8 \cdot K_c \cdot [CH_3OH] + k_9 \cdot K_c^{\,2} \cdot [CH_3OH]^2}{\left(1 + K_c \cdot [CH_3OH]\right)^2} \qquad (18)$$

The only difference between equations (17) and (18) is the exponent on the denominator. Equations (17) and (18) indicate that at low [CH_3OH], $k_{obs,ir} \approx k_{obs,uv} \approx k_{10} + k_8 \cdot K_c \cdot [CH_3OH]$. From Chapter 2, $k_8 \cdot K_c$ at 231K was determined to be approximately 1×10^{-27} cm^6 $molecule^{-2}$ s^{-1}.[14] In that chapter, $k_8 \cdot K_c$ was equivalent to k'. Using the value $K_c(231\ K) \approx 5 \times 10^{-17}$ cm^3 $molecule^{-1}$, determined in the present study, $k_8 \approx 2 \times 10^{-11}$ cm^3 $molecule^{-1}$ s^{-1}.

From equation (17), it can be shown that the observation $\frac{d^2 k_{obs,ir}}{d[CH_3OH]^2} > 0$, which is evident in Figure 3.7, implies that $k_9 > (k_8 - k_{10}) \approx 1.8 \times 10^{-11}$ cm^3 $molecule^{-1}$ s^{-1}. This indicates that the self-reaction of the complex occurs at a significant rate.

The data shown in Figure 3.7 was fit using equations (17) and (18) to determine values for k_8 and k_9. As stated above, the data was acquired at 231 K and 100 Torr. The values used for k_{10} and K_c were 2.2×10^{-12} cm^3 $molecule^{-1}$ s^{-1} and 4.8×10^{-17} cm^3 $molecule^{-1}$, respectively. The value of k_{10} was taken from Chapter 2 and the value of K_c taken from this work. The values of k_{10} and K_c were held constant during the fitting process. The fitted parameters for the IR data using equation (17) were: $k_8 = (2.3 \pm 0.2) \times 10^{-11}$ cm^3 $molecule^{-1}$ s^{-1} and $k_9 = (7.1 \pm 0.4) \times 10^{-11}$ cm^3 $molecule^{-1}$ s^{-1}. The fitted parameters for the UV data using equation (18) were: $k_8 = (3.1 \pm 0.5) \times 10^{-11}$ cm^3 $molecule^{-1}$ s^{-1} and $k_9 = (3.3 \pm 2.2) \times 10^{-11}$ cm^3 $molecule^{-1}$ s^{-1}.

The values acquired from fitting the IR data were considered more accurate than the values acquired in the UV. This judgement was based on the high degree of uncertainty in the individual UV measured rate coefficients due to poor signal-to-noise as

well as the fact that the UV signal departed significantly from second-order at high concentrations of methanol. Further, the assumption that HO_2 and $HO_2{\cdot}CH_3OH$ absorb identically has not yet been experimentally verified.

3.6 Discussion

Aloisio et al.[15] measured $\Delta H = (-36 \pm 16)$ kJ mol^{-1} for $HO_2 + H_2O \underset{M}{\overset{M}{\rightleftharpoons}} HO_2{\cdot}H_2O$. In the present study, $\Delta H = (-36 \pm 3)$ kJ mol^{-1} for $HO_2 + CH_3OH \underset{M}{\overset{M}{\rightleftharpoons}} HO_2{\cdot}CH_3OH$. However, Aloisio et al. measured ΔS to be (-85 ± 40) J mol^{-1} K^{-1} whereas we determined ΔS = (-96 ± 96) J mol^{-1} K^{-1}. The values of equilibrium constants they measured for $H_2O \underset{M}{\overset{M}{\rightleftharpoons}} HO_2{\cdot}H_2O$ were a factor of 3.5 larger than K_c measured in the present study.

Our calculations indicated that ΔH = -37 kJ mol^{-1} which is very similar to what we measured from experiment. However, the experimental values for K_c were a factor of 16 to 18 higher than what was calculated.

As stated above, $k_8 = (2.3 \pm 0.2) \times 10^{-11}$ cm^3 molecule^{-1} s^{-1} and $k_9 = (7.1 \pm 0.4) \times 10^{-11}$ cm^3 molecule^{-1} s^{-1}. The observation of a fast rate coefficient for reaction (8) is not unexpected. However, the observation of a fast rate coefficient for reaction (9) is an important finding. Hamilton and Lii[13] argued, based on experimental evidence, that the rate coefficient for reaction (9) was negligibly small. Bloss et al.[16] measured k_9 to be $(3.2 \pm 0.5) \times 10^{-11}$ cm^3 molecule^{-1} s^{-1}.

3.7 Conclusions

We measured the value of K_c for $HO_2 + CH_3OH \leftrightarrow HO_2{\cdot}CH_3OH$ and the rate coefficient for the forward process. From these measurements, we inferred the dissociation rate for $HO_2{\cdot}CH_3OH$. We compared measured values of K_c to theoretical calculations. We also measured the observed rate of the HO_2 self-reaction in the presence of methanol and determined, indirectly, the rate coefficients for $HO_2 + HO_2{\cdot}CH_3OH$ and the $HO_2{\cdot}CH_3OH$ self-reaction. Our results confirm that the mechanism responsible for the observed rate enhancement is due to the formation of a hydrogen-bonded complex.

3.8 References

1. Chapter 1.

2. Hamilton, E. J., Jr. "Water Vapor Dependence of the Kinetics of the Self-reaction of HO_2 in the Gas Phase." J. Chem. Phys. 63: 3682-3683 (1975).

3. Lii, R.-R., R. A. Gorse, Jr. , et al. "Temperature Dependence of the Gas-Phase Self-Reaction of HO_2 in the Presence of NH_3." J. Phys. Chem. 84: 813-817 (1980).

4. Lii, R.-R., M. C. Sauer, Jr., et al. J. Phys. Chem. 85: 2833-2834 (1981).

5. Kircher, C. C. and S. P. Sander "Kinetics and Mechanism of HO_2 and DO_2 Disproportionations." J. Phys. Chem. 88: 2082-91 (1984).

6. Andersson, B. Y., R. A. Cox, et al. "The Effect of Methanol on the Self Reaction of HO_2 Radicals." Int. J. Chem. Kinetics 20: 283-295 (1988).

7. Hansen, J. C. "Private communication."

8. Pimentel, G. C. and A. L. McClellan (1960). The Hydrogen Bond. San Francisco and London, W. H. Freeman and Company.

9. Aloisio, S. and J. S. Francisco "Existence of a Hydroperoxy and Water ($HO_2 \cdot H_2O$) Radical Complex." J. Phys. Chem. A 102: 1899-1902 (1998).

10. Aloisio, S., Y. Li, et al. "Complete Active Space Self-Consistent Field and Multireference Configuration Interaction Studies of the Differences Between the Low-Lying Excited States of HO_2 and HO_2 –H_2O." Journal of Chemical Physics 110: 9017-9019 (1999).

11. Curtis, A. R. and W. P. Sweetenham (1987). FACSIMILE/CHEKMAT, H015 ed. Harwell: Oxfordshire (UK).

12. DeMore, W. B., S. P. Sander, et al. (1997). Chemical Kinetics and Photochemical Data for Use in Stratospheric Modeling, Evaluation Number 12. Pasadena, CA, Jet Propulsion Laboratory, California Institute of Technology.

13. Hamilton, E. J., Jr. and R.-R. Lii "The Dependence on H_2O and on NH_3 of the Kinetics of the Self-Reaction of HO_2 in the Gas-Phase Formation of $HO_2 \cdot H_2O$ and $HO_2 \cdot NH_3$ Complexes." Int. J. Chem. Kinet. 9: 875-885 (1977).

14. "Chapter 2."

15. Aloisio, S., J. S. Francisco, et al. "Experimental Evidence for the Existence of the HO_2-H_2O Complex." J. Phys. Chem. 104: 6597-6601 (2000).

16. Bloss, W. J., D. M. Rowley, et al. "Rate Coefficient for BrO + HO_2 Reaction at 298 K." Phys. Chem. Chem. Phys. 4: 3639-3647 (2002).

Table 3.1. Relevant reactions.

# in text	Reaction		Ref.
2	$F + H_2 \rightarrow HF + H$	$1.4 \cdot 10^{-10} \cdot \exp^{(-500/T)}$	NASA
3	$H + O_2 + M \rightarrow HO_2 + M$	$k_o = 5.7 \times 10^{-32} \cdot (T/300)^{-1.6}$, $k_\infty = 7.5 \times 10^{-11}$	NASA
5	$Cl + CH_3OH \rightarrow HCl + CH_2OH$	$5.4 \cdot 10^{-11}$	NASA
6	$CH_2OH + O_2 \rightarrow HO_2 + CH_2O$	9.1×10^{-12}	NASA
7	$HO_2 + CH_3OH + M \rightarrow HO_2 \cdot CH_3OH + M$	4.0×10^{-12} at 231 K, 100 Torr	this work
-7	$HO_2 \cdot CH_3OH + M \rightarrow HO_2 + CH_3OH + M$	8.5×10^{4} s^{-1} at 231 K, 100 Torr	this work
8	$HO_2 + HO_2 \cdot CH_3OH \rightarrow$ Products	2.3×10^{-11} at 231 K, 100 Torr	this work
9	$HO_2 \cdot CH_3OH + HO_2 \cdot CH_3OH \rightarrow$ Products	7.1×10^{-11} at 231 K, 100 Torr	this work
10	$HO_2 + HO_2 \rightarrow H_2O_2 + O_2$	$1.5 \cdot 10^{-12} \exp^{(19/T)} + 1.7 \cdot 10^{-33} \cdot [M] \cdot \exp^{(1000/T)}$	Chap. 2

Table 3.2. Experimental conditions.

Measurements of K_{eq}, k_7 and k_{-7}						
Temp K	[M] Torr	[Cl_2] 10^{14} cm^{-3}	[O_2] 10^{18} cm^{-3}	[CH_3OH] 10^{16} cm^{-3}	[N_2] 10^{18} cm^{-3}	
231	50	30 - 33	0.9 - 1.5	0.5-2.4	0.9 –1 .5	
231	100	5.4 - 7.1	1.6	0.3-2.2	1.6	
240	100	4.3 - 9.1	2.7 - 3.5	1.4-9.1	0 – 0.8	
251	100	6.1 - 9.6	2.2 - 3.4	5.1-28	0 – 1.2	
261	100	4.3 - 14	2.2 - 3.3	4.5-33	0 - 1.1	
Measurements of k_{obs} at 100 Torr						
HO_2 source	[F_2] 10^{16}	[Cl_2] 10^{15} cm^{-3}	[O_2] 10^{18} cm^{-3}	[CH_3OH] 10^{14} cm^{-3}	[H_2] 10^{17} cm^{-3}	[N_2] 10^{18} cm^{-3}
Cl_2 + $h\nu$		5-11	1-2	2-200		1.8-2
F_2 + $h\nu$	2-8		0.3-1		3-10	0.5-1.5
gas purity	97%	99.5%	99.996%	HPLC	99.999%	99.9993%

Table 3.3. Values of K_{eq}, k_7, and k_{-7}.

T (K)	P (Torr)	K_{eq} [a]	SD [a]	# of runs	k_7 [b]	SD [b]	$(k_7/K_{eq}) = k_{-7}$ [c]	# of runs
231	50	4.9×10^{-17}	5×10^{-18}	5	2.5	0.6	5.2×10^{4}	2
231	100	4.9×10^{-17}	5×10^{-18}	10	4.0	0.8	8.5×10^{4}	2
240	100	2.2×10^{-17}	5×10^{-18}	12	4.8	1.5	1.9×10^{5}	5
251	100	1.1×10^{-17}	2×10^{-18}	15	3.2	1.8	2.8×10^{5}	4
261	100	6.8×10^{-18}	1×10^{-18}	15	2.6	1.4	4.0×10^{5}	2

[a] in units of cm^3 $molecule^{-1}$

[b] in units of 10^{-12} cm^3 $molecule^{-1}$ s^{-1}

[c] in units of s^{-1}

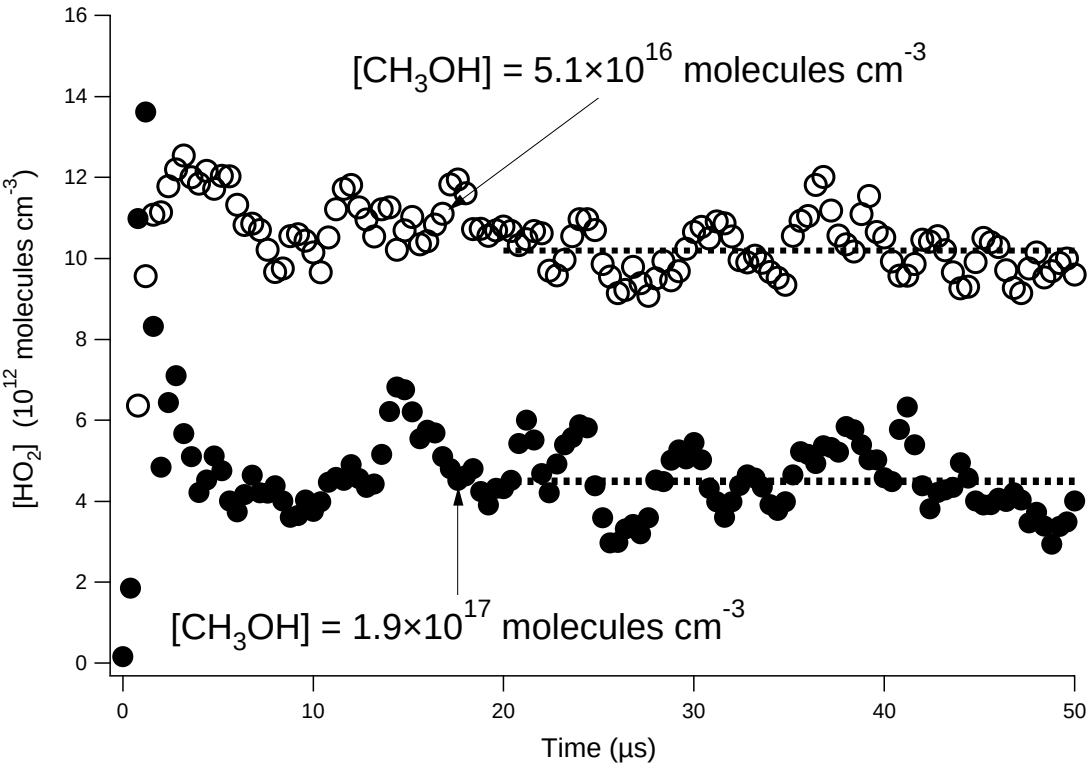

Figure 3.1. Time dependence of HO_2 signal at different methanol concentrations at 251 K, 100 Torr. As the figure shows, there is a fast rise then drop in the HO_2 signal. The rise is due to the formation of HO_2 via Cl + CH_3OH consecutive CH_2OH + O_2 reactions. The decrease is due to $HO_2 + CH_3OH \xrightarrow{M} HO_2 \cdot CH_3OH$.

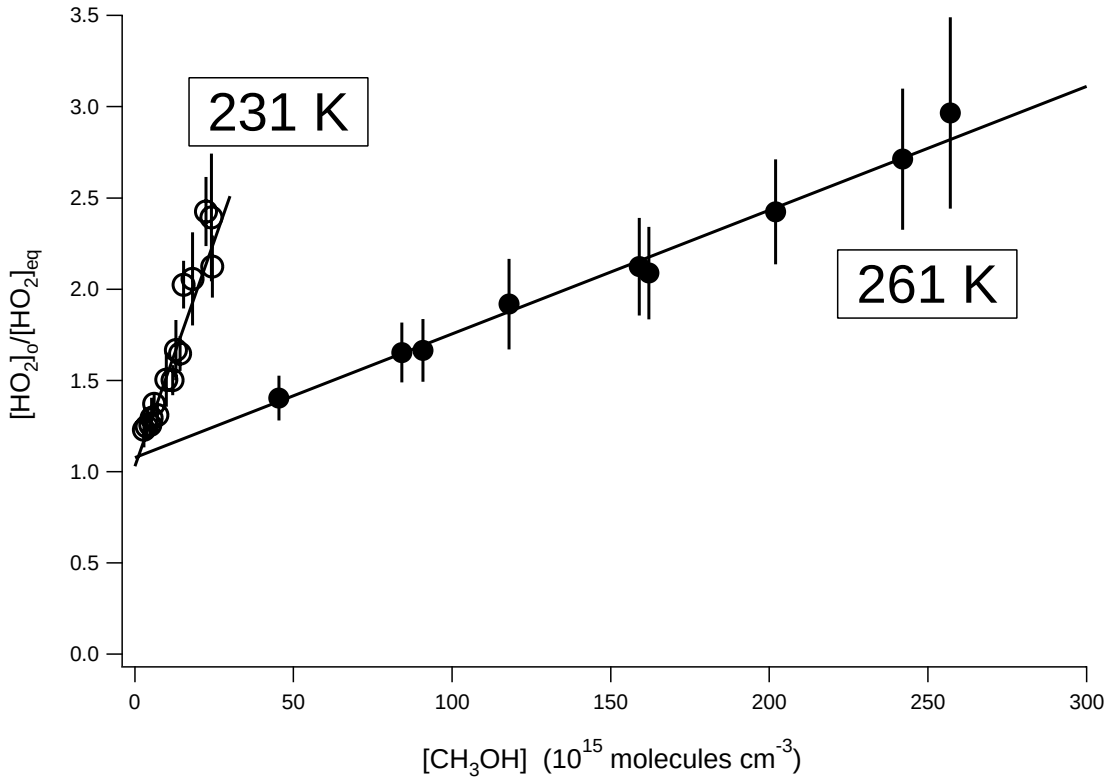

Figure 3.2. The dependence of $[HO_2]_o/[HO_2]_{eq}$ on methanol concentration at 231 K and 261 K. The slope of the line is equivalent to K_{eq}. The vapor pressure concentration of CH_3OH at 231 K is approximately 4.6×10^{16} molecules cm^{-3}. All measurements were conducted at less than have the vapor pressure concentration at each temperature.

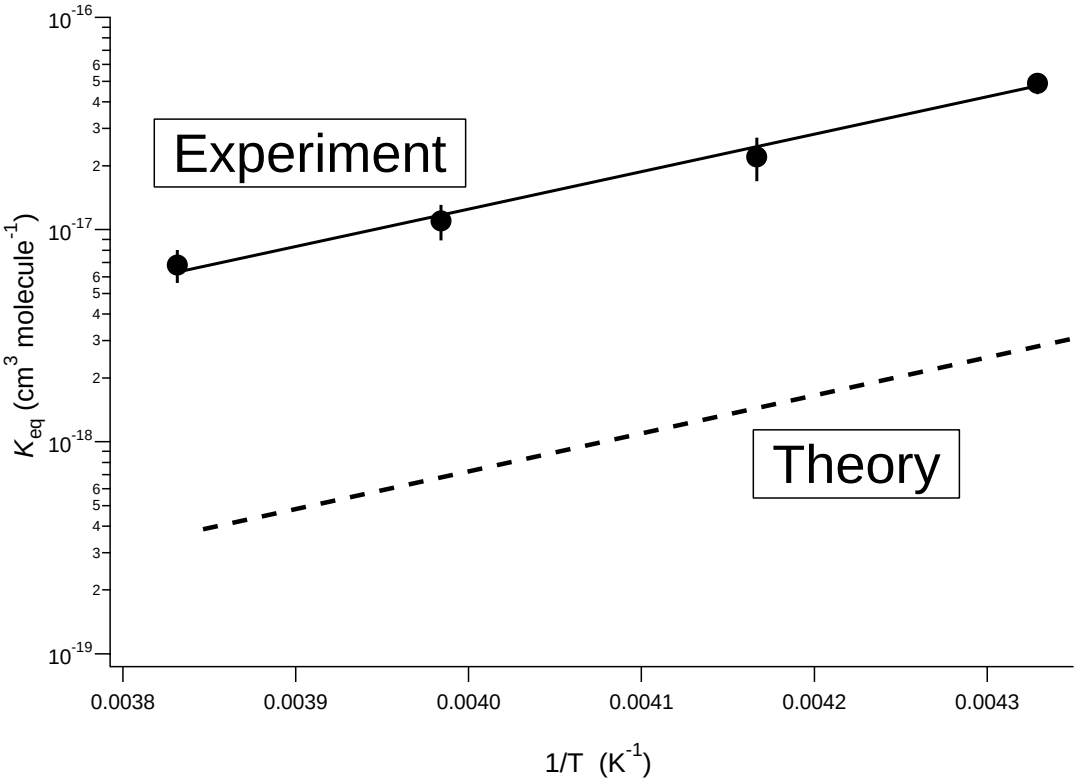

Figure 3.3. Comparisons of experimentally measured and theoretically calculated K_c. Between 231 K and 261 K, the experimentally measured K_c was between a factor of 16 and 18 higher than the calculated values.

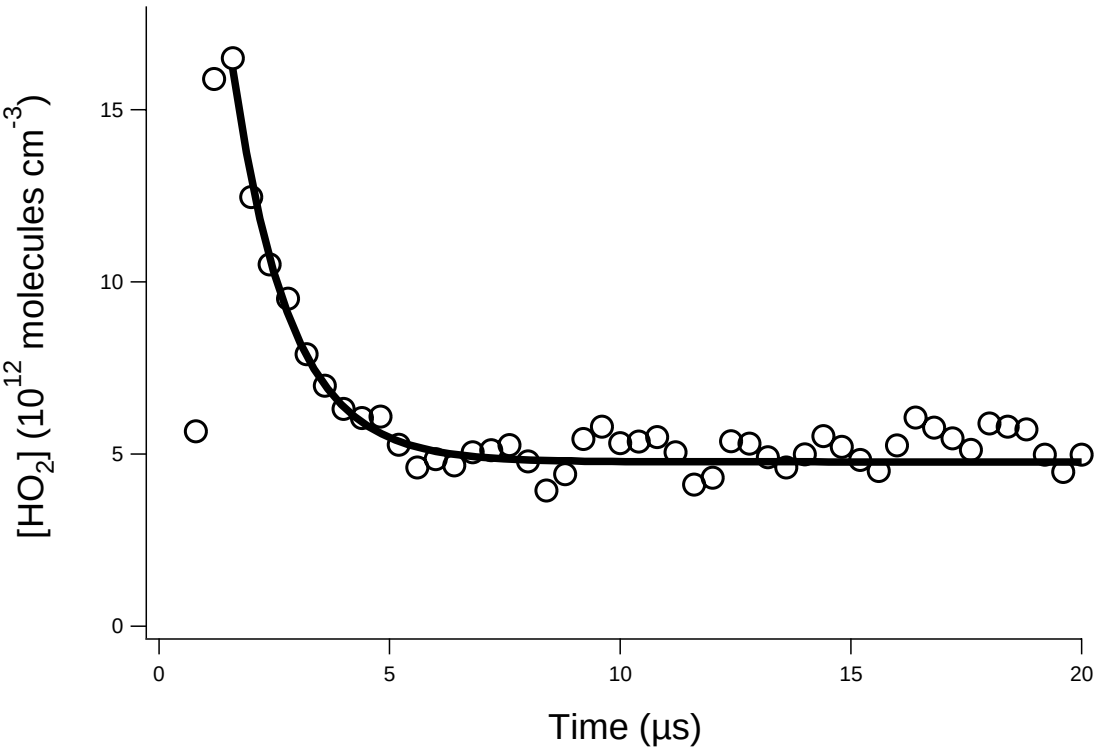

Figure 3.4. Decay of $[HO_2]$ from the reaction $HO_2 + CH_3OH \xrightarrow{M} HO_2 \cdot CH_3OH$ at 240 K, 100 Torr.

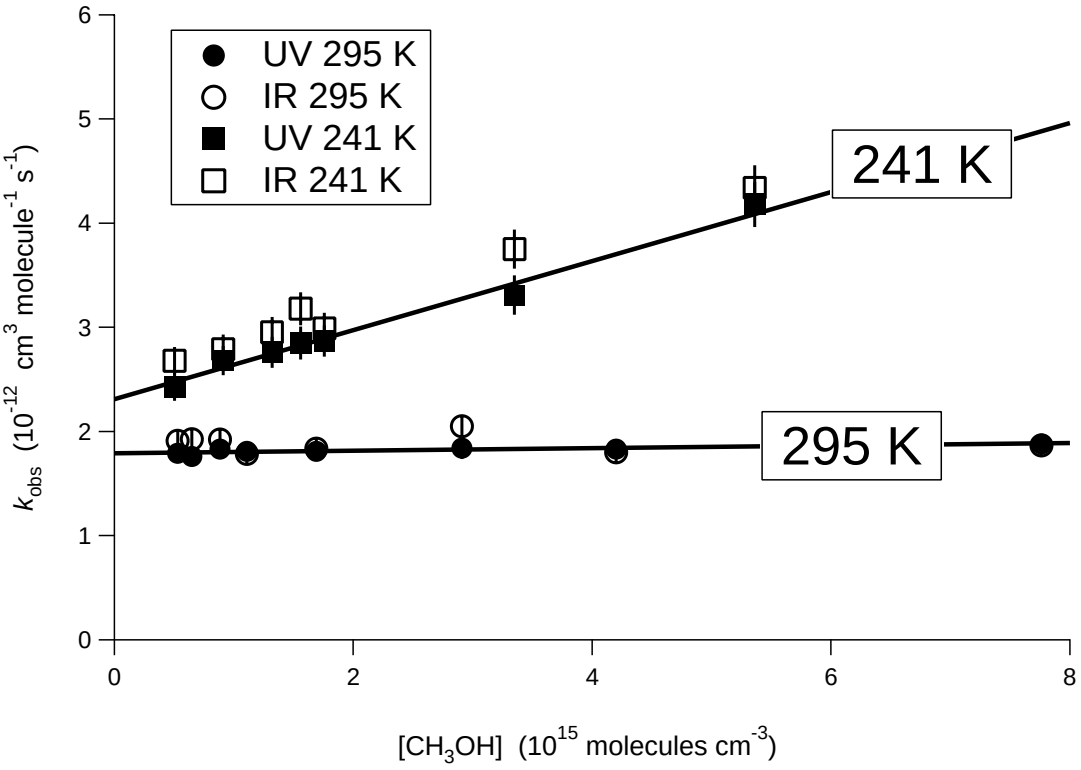

Figure 3.5. Comparisons of the observed rate coefficient for the HO_2 self-reaction between the IR and UV detection channels at two different temperatures. The error bars are 1σ.

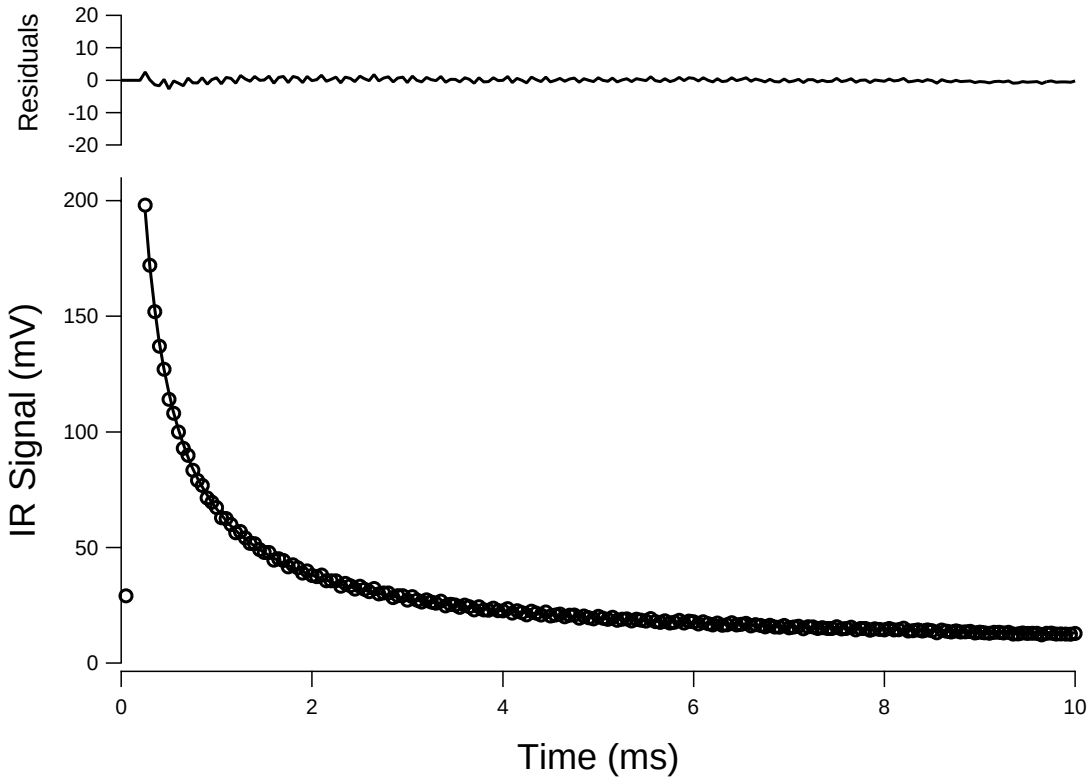

Figure 3.6.1. Typical example of the IR signal at 231 K, 100 Torr. The data was acquired at $[CH_3OH] = 1.3 \times 10^{16}$ molecules cm^{-3}.

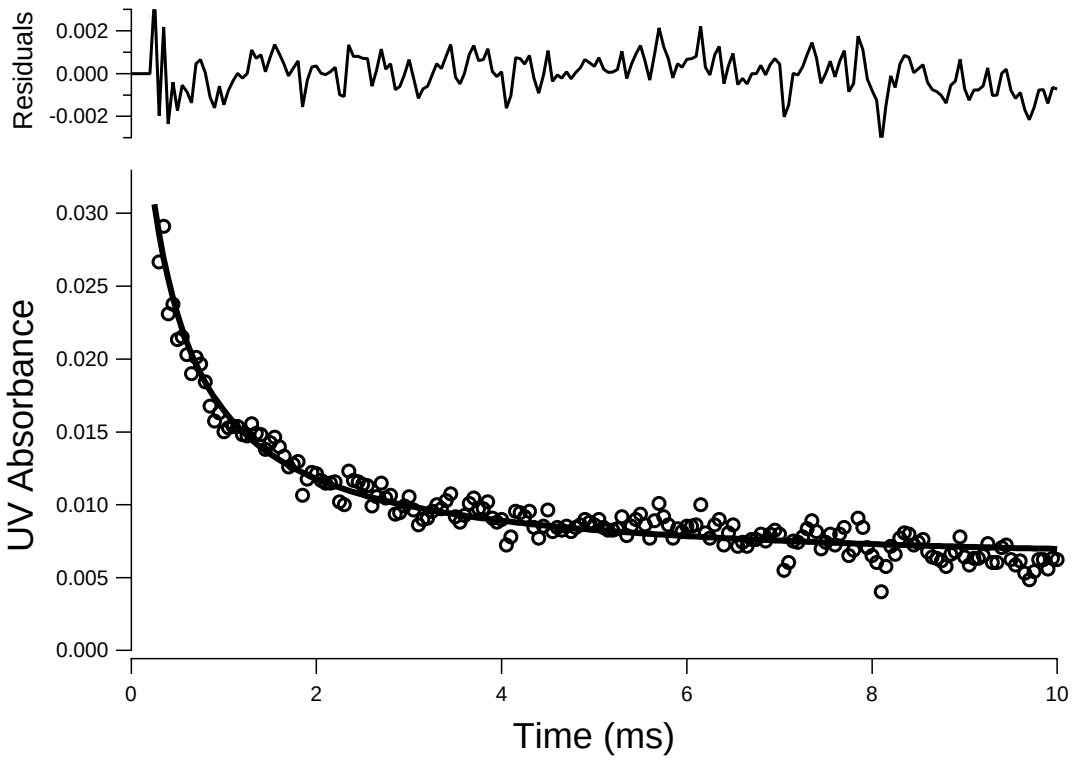

Figure 3.6.2. Typical example of the UV signal at 231 K, 100 Torr. The data was acquired at $[CH_3OH] = 1.3 \times 10^{16}$ molecules cm^{-3}.

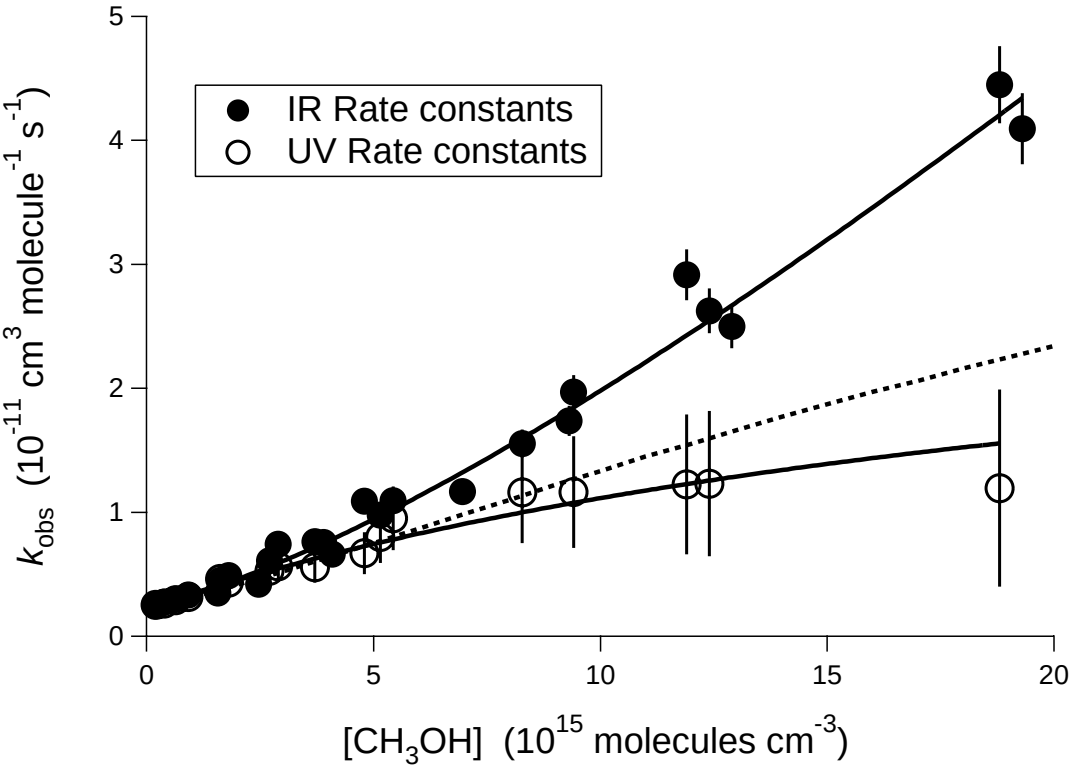

Figure 3.7. $k_{obs,ir}$ and $k_{obs,uv}$ versus methanol concentration at 231 K, 100 Torr. The solid lines are fits to each spectral channel independently. The dotted line is what is expected for $k_{obs,uv}$ using the fitted parameters from the IR data.

Chapter 4: Kinetics of CH_3O_2 Reactions

4.1 Introduction

Reactions between peroxy radicals are an important class of reactions in atmospheric and combustion chemistry. In the troposphere, peroxy radicals are intermediates in the oxidation of alkane. Under conditions of low NO_x (< 30 ppt), which occur in the unpolluted troposphere, reactions between peroxy radicals are significant and are an important consideration when determining local ozone production rates. Overall, the reactions

$$CH_3O_2 + CH_3O_2 \rightarrow CH_3O + CH_3O + O_2 \quad (1a)$$

$$\rightarrow CH_3OH + CH_2O + O_2 \quad (1b)$$

$$\rightarrow CH_3OOCH_3 + O_2 \quad (1c)$$

$$HO_2 + CH_3O_2 \rightarrow CH_3OOH + O_2 \quad (2a)$$

$$\rightarrow CH_2O + H_2O + O_2 \quad (2b)$$

remove peroxy species that would otherwise react with NO to eventually form ozone.

Recently, field measurements of OH, HO_2, H_2O_2, and CH_3OOH in the upper troposphere have led researchers to propose that the rate of reaction (2) might be substantially faster than that suggested by the current NASA data evaluation at temperatures applicable to the upper troposphere, below 273 K.[1] Field measurements of

ozone production rates in polluted air masses in the lower troposphere have suggested that near 298 K, the rate NASA recommended coefficient for reaction (2) may be nearly a factor of 10 too large.[2]

There is significant disagreement between previous measurements of the rate coefficients and product branching ratios for reactions (1) and (2). Separate studies of reaction (1) have measured significantly different temperature dependences for product branching ratios.[3,4] Measured rate coefficients for reaction (2) differ substantially between studies that examined the reaction below 273 K.[5,6]

This chapter describes measurements of the rate coefficient of reaction (2) and the product branching ratio for reaction (1). Our measurements utilized IR heterodyne spectroscopy to monitor the time-dependence of HO_2 and UV spectroscopy to monitor the time-dependence of CH_3O_2. The use of IR spectroscopy is a major experimental difference between our measurements and previous studies. We conducted our studies under conditions in which there were low levels of chemical species that could form hydrogen-bonded complexes with HO_2 such as methanol. This differs from previous low temperature studies of reaction (2) that utilized CH_3OH as a pre-cursor for HO_2.[5,6]

4.2 Experimental

Much of the experimental technique has been described in Chapter 1. Briefly, an excimer laser was used to photolyze F_2 in gas-mixtures of H_2-CH_4-O_2-N_2. Subsequent reactions produced HO_2 and CH_3O_2 via the reaction sequence

$$F_2 \xrightarrow{h\nu} 2\,F \qquad (3)$$

$$F + H_2 \longrightarrow HF + H \quad (4)$$

$$H + O_2 \xrightarrow{M} HO_2 \quad (5)$$

$$F + CH_4 \longrightarrow HF + CH_3 \quad (6)$$

$$CH_3 + O_2 \xrightarrow{M} CH_3O_2 \quad (7)$$

Gas concentrations and purities are listed in Table 4.1. Kinetic modeling using the rates listed in Table 4.2 indicated that CH_3O_2 and HO_2 formation occurred between 5 μs and 30 μs for both species.

It was important to consider the reaction

$$CH_3O + O_2 \longrightarrow HO_2 + CH_2O \quad (8)$$

The rate coefficient at 298 K for reaction (8) is approximately 2×10^{-15} cm^3 $molecule^{-1}$ s^{-1}, according to the 1997 NASA evaluation.[7] Since typical O_2 concentrations were around 1×10^{18} molecules cm^{-3}, the time constant for HO_2 formation from the CH_3O + O_2 reaction was approximately 500 μs at 298 K. Because no measurements of the rate coefficient for reaction (8) have been done below 298 K, the recommended values are extrapolated for temperatures below 298 K. Thus, there is some uncertainty in k_8 below 298 K. The recommended value at 231 K is approximately 8×10^{-16} cm^3 $molecule^{-1}$ s^{-1} and the time constant for HO_2 formation from reaction (8) is expected to be around 1.3 ms. Because this rate of HO_2 formation is relatively slow in comparison to the timescale of measurements, the time dependence of the HO_2 concentration is dependent

on the concentration of O_2. Also, there is a high degree of uncertainty in the values of the rate coefficients of $CH_3O + HO_2$ and $CH_3O + CH_3O_2$. In a literature review conducted by Tsang and Hampson,[8] they suggested that the rate coefficients for these reactions was between (5×10^{-12} and 5×10^{-14}) cm^3 $molecule^{-1}$ s^{-1}. However, Pilling and Smith have suggested that the rate of $CH_3O + CH_3O_2$ was on the order of 1×10^{-11} cm^3 $molecule^{-1}$ s^{-1} at 298 K. If the rate coefficients for these reactions are greater than 5×10^{-12} cm^3 $molecule^{-1}$ s^{-1}, then the $CH_3O + HO_2$ and $CH_3O + CH_3O_2$ reactions would provide another loss mechanism for CH_3O other than reaction by O_2. This would result in an incorrect interpretation of CH_3O production from reaction (1).[9]

Photolysis of F_2 was chosen over photolysis of Cl_2 in CH_3OH-CH_4-O_2-N_2 gas-mixtures because of two reasons. First, the $Cl + CH_4$ reaction is relatively slow, resulting in a relatively long lifetime for Cl. The $Cl + CH_3O_2 \rightarrow HCl + CH_3O$ reaction becomes a significant experimental concern. Subsequent HO_2 production from the $CH_3O + O_2$ reaction would complicate our kinetic analysis. Second, it has been shown in Chapters 1, 2, and 3 that CH_3OH can hydrogen-bond with HO_2 and that this can lead to significant enhancements of the $HO_2 + HO_2$ and $HO_2 + NO_2 + M$ reactions at low temperatures and high methanol concentrations.[1014] A similar enhancement of the $HO_2 + CH_3O_2$ reaction might also occur. The two previous low temperature studies of reaction (2) utilized CH_3OH at temperatures below 273 K,[5,6] which may have resulted in higher measured rate coefficients than applicable in the atmosphere.

4.3 Rate Coefficient for the $CH_3O_2 + HO_2$ Reaction

Reaction (2) was studied between 296 K and 231 K at 100 Torr. Figures 4.1.1 and 4.1.2 show IR and UV data taken at 231 K at various $[H_2]/[CH_4]$ ratios. The ratio $[HO_2]_o/[CH_3O_2]_o$ is nearly equivalent to the ratio $\{k_4[H_2]\}/\{k_6[CH_4]\}$. The observed $[HO_2]_o/[CH_3O_2]_o$ ratio was consistent with the expected ratio using the measured values for $[H_2]$ and $[CH_4]$ and recommended values of k_4 and k_6.

We elected to determine k_2 by subtracting out the $[HO_2]$ time dependence at $[H_2]/[CH_4] = 0$ from the $[HO_2]$ time dependence recorded at $[H_2]/[CH_4] < 0.5$. For examination of reaction (2), $\{[HO_2]_o + [CH_3O_2]_o\}$ was between (8 to 10) $\times 10^{13}$ molecules cm^{-3}. At $[H_2]/[CH_4] = 0.5$, the decrease in $[CH_3O_2]_o$ in comparison to its value at $[H_2]/[CH_4] = 0$ was between 10% and 15%. Despite this decrease in $[CH_3O_2]_o$ as $[H_2]/[CH_4]$ increased, measurements of k_2 were not adversely affected, as demonstrated below.

Fitting of the subtracted $[HO_2]$ time profiles utilized a first-order expression

$$S(t) = B + S_o e^{-kt} \qquad (9)$$

where $S(t)$ is the signal at time = t, S_o is the signal at time = 0, and B accounts for a baseline offset. Fits to data were done over approximately 3 e^{-1} times, which was 10 ms at 296 K and 5 ms at 231 K.

The manner of measuring k_2 outlined above was selected because it separates the measurement of the branching ratio of the CH_3O_2 self-reaction from the measurement of k_2. For describing the time dependence of $[HO_2]$, these two kinetic parameters are

strongly correlated. Moreover, the uncertainty in the rate coefficient of the $CH_3O + O_2$ reaction at low temperatures, as well as complications from the possible $CH_3O + CH_3O_2$ and $CH_3O + HO_2$ reactions, results in significant uncertainty in determining kinetic parameters from the $[HO_2]$ time dependence. Further, it will be shown below that currently suggested products and the branching ratio of reaction (1), and perhaps k_8, were not consistent with the present results at low temperatures. The abstraction of kinetic information regarding k_2 and the branching ratio is thus highly subject to error if each fit was analyzed by fitting the time dependence of $[HO_2]$ by fitting k_2, the branching ratio, and k_8 all at once.

There are several problems associated with the measurement of k_2 in the manner outlined above. First, the concentration of CH_3O_2 changes during the course of the fit. This means that the time dependence of $[HO_2]$ is not truly first-order. Second, as $[H_2]/[CH_4]$ increases, the HO_2 formed by the CH_3O_2 self-reaction decreases. This means that the decays have been "overly" corrected for HO_2 produced by the CH_3O_2 self-reaction.

Kinetic modeling was done using the rate coefficients listed in Table 4.2 and the FACSIMILE kinetic modeling program.[15] The simulated signal at $[H_2]/[CH_4] = 0$ was subtracted from simulated signals where $[H_2]/[CH_4]$ was varied between 0.05 and 0.5. First-order fits over 5 ms to 10 ms were performed after subtraction and rate coefficients were obtained. These rate-coefficients were then divided by $[CH_3O_2]_o$. At 296 K, at $[H_2]/[CH_4] = 0.5$, the measured rate was 6% larger than the rate used in the model (ideal rate) and at $[H_2]/[CH_4] = 0.05$, the measured rate was 1% larger than the ideal rate. At 231 K, at $[H_2]/[CH_4] = 0.5$, the measured rate was equal to the ideal rate and at

$[H_2]/[CH_4]$ = 0.05, the measured rate was 4% lower than the ideal rate. Since the reported rates were averaged from data acquired at $[H_2]/[CH_4]$ between 0.05 and 0.5, the overall systematic error was that the measured rate coefficient was 4% high at 296 K. Reported values have not been corrected for these systematic errors. Figure 4.2 shows natural log plots of data that had been adjusted in above manner. The linearity of the plots indicates that the approximation of first-order type behavior is valid.

The measured values of k_2 versus T were fit to the equation $k_2(T) = A \cdot \exp(-E_a/(RT))$. The fitted values were $A = (7.6 \pm 3.0) \times 10^{-13}$ cm^3 molecule^{-1} s^{-1} and $E_a/R = (-560 \pm 70)$ K. The latter value translates into (-4.7 ± 0.6) kJ mol^{-1}. Figure 4.3 is an Arrhenius plot of the measured values of k_2 versus T^{-1}. The measured values from the present study were very similar the NASA recommended values at 298 K but were approximately 50% lower than the recommended values at 231 K. They are listed in Table 4.3.

4.4 Product Branching Ratio for the $CH_3O_2 + CH_3O_2$ Reaction

The three reaction pathways that have been listed above for reaction (1) are based on FTIR[16,3,17] and kinetic studies.[4]

$CH_3O_2 + CH_3O_2$

$\rightarrow CH_3O + CH_3O + O_2$ $\quad \Delta H = (0 \pm 13)$ kJ mol^{-1} (1a)

$\rightarrow CH_3OH + CH_2O + O_2$ $\quad \Delta H = (-344 \pm 12)$ kJ mol^{-1} (1b)

$\rightarrow CH_3OOCH_3 + O_2$ $\quad \Delta H = (-159 \pm 12)$ kJ mol^{-1} (1c)

The values for the change of enthalpy are from the 1997 NASA recommendation. Using the values of k_2 determined from the procedure outlined above, the measurements of $[HO_2]$ and $[CH_3O_2]$ time dependences at $[H_2]/[CH_4] = 0$, were used to fit the kinetic model using the rates listed in Table 4.2. The value of the branching ratio was allowed to vary and reaction (1c) was assumed not to occur. The fits were conducted over the first 10 ms of data.

Over the course of 10 ms, the kinetic model reproduced the experimental $[HO_2]$ and $[CH_3O_2]$ time dependences reasonably well at 296 K but poorly at 231 K. At temperatures in between, the fits became progressively worse as the temperature approached 231 K. Figures 4.4.1 and 4.4.2 are experimental data acquired at 296 K and 231 K, respectively, and the fits from using FACSIMILE. Figure 4.4.3 depicts the $[HO_2]$ measurements at 296 K and 231 K. For the measurement at 296 K, $[CH_3O_2]_o$ was approximately 7.9×10^{13} molecules cm^{-3} and at 231 K, it was 8.4×10^{13} molecules cm^{-3}. The values of $k_{1a}/(k_{1a}+k_{1b})$, denoted α, are listed in Table 4.3. The value of k_{1c} was assumed to be 0.

The rate coefficient for the observed rate of the CH_3O_2 self-reaction was measured as a function of temperature. The observed rate coefficient is assumed to be larger than k_1 because CH_3O from branching channel (1a) either reacts quickly with O_2 to form HO_2 which in turn reacts with CH_3O_2, or CH_3O reacts directly with CH_3O_2. The measured values of the observed rate coefficient for the CH_3O_2 self-reaction are tabulated in Table 4.4. At 296 K, our measured values were approximately 25% lower than the NASA recommendations if the branching ratio for channel (1a) was 30%. At 231 K, our values were approximately 20% lower than the recommendations at a branching ratio of

10%, as suggested by FTIR studies of the CH_3O_2 self-reaction.[3] The recommended error in the rate constant given by the recommendation was 50% at 296 K and 80% at 231 K.

4.5 Results and Discussion

As Figure 4.4.3 indicates, the rise time in $[HO_2]$ is faster at 231 K than at 296 K. This is despite the fact that the values of $[CH_3O_2]_o$ and k_1 at the two temperature are nearly equivalent. Moreover, there is no delay in HO_2 formation as expected for the $CH_3O + O_2$ reaction. To date, the $CH_3O + O_2$ (8) reaction has only been studied above 298 K. Work by Wantuck et al.[18] revealed that the rate coefficient displayed non-Arrhenius-type behavior above 500 K. The rate of reaction (8) would have to be greater than 10^{-13} cm^3 $molecule^{-1}$ s^{-1} at 231 K to explain the rapid rise in HO_2 signal. This is a significant departure from expected temperature dependence and not likely to occur.

A more likely explanation is that another product is formed from reaction (1). Figure 4.5 shows a possible reaction pathway that accounts for the formation of CH_3O, CH_3OH, and CH_2O products. One possible explanation for the quick formation of HO_2 is depicted in Figure 4.6.

Our measurements of the rate coefficient for reaction (2) are lower than previous measurements. This can be partly explained by the use of methanol in previous experiments.

4.5 Conclusions

The rate coefficient for $HO_2 + CH_3O_2$ was measured at 100 Torr between 231 K and 296 K and was found to be lower than the NASA recommended rate. Branching ratio

studies of the CH_3O_2 + CH_3O_2 reaction indicated the possibility of a change in reaction products at low temperatures.

4.5 References

1. Ravetta, F., D. J. Jacob, et al. "Experimental Evidence for the Importance of Convected Methylhydroperoxide as a source of Hydrogen Oxide (HO_x) Radicals in the Tropical Upper Troposphere." Journal of Geophysical Research-Atmospheres 106: 32709-32716 (2001).
2. Thornton, J. A. Submitted to JGR.
3. Horie, O., J. N. Crowley, et al. J. Phys. Chem. 94: 8198-8203 (1990).
4. Lightfoot, P. D., R. Lesclaux, et al. "Flash Photolysis Study of the CH_3O_2 + CH_3O_2 Reaction: Rate Constants and Branching Ratios from 248 to 573 K." Journal of Physical Chemistry 94: 700-707 (1990).
5. Dagaut, P., T. J. Wallington, et al. "Temperature Dependence of the Rate Constant for the HO_2 + CH_3O_2 Gas-Phase Reaction." J. Phys. Chem. 92: 3833-3836 (1988).
6. Lightfoot, P. D., B. Veyret, et al. "Flash Photolysis Study of the CH_3O_2 + HO_2 Reaction between 248 and 573 K." J. Phys. Chem. 94: 708-714 (1990).
7. DeMore, W. B., S. P. Sander, et al. (1997). Chemical Kinetics and Photochemical Data for Use in Stratospheric Modeling, Evaluation Number 12. Pasadena, CA, Jet Propulsion Laboratory, California Institute of Technology.
8. Tsang, W. and R. F. Hampson "Chemical Kinetic Database For Combustion Chemistry.1. Methane and Related-Compounds." Journal of Physical and Chemical Reference Data 15: 1087-1279 (1986).

9. Pilling, M. J. and M. J. C. Smith "A Laser Flash Photolysis Study of the Reaction $CH_3 + O_2 => CH_3O_2$ at 298 K." Journal of Physical Chemistry 89: 4713-4720 (1985).

10. Hamilton, E. J., Jr. "Water Vapor Dependence of the Kinetics of the Self-reaction of HO_2 in the Gas Phase." J. Chem. Phys. 63: 3682-3683 (1975).

11. Hamilton, E. J., Jr. and R.-R. Lii "The Dependence on H_2O and on NH_3 of the Kinetics of the Self-Reaction of HO_2 in the Gas-Phase Formation of $HO_2 \cdot H_2O$ and $HO_2 \cdot NH_3$ Complexes." Int. J. Chem. Kinet. 9: 875-885 (1977).

12. Lii, R.-R., R. A. Gorse, Jr. , et al. "Temperature Dependence of the Gas-Phase Self-Reaction of HO_2 in the Presence of NH_3." J. Phys. Chem. 84: 813-817 (1980).

13. Andersson, B. Y., R. A. Cox, et al. "The Effect of Methanol on the Self-Reaction of HO_2 Radicals." Int. J. Chem. Kinetics 20: 283-295 (1988).

14. Chapter 3.

15. Curtis, A. R. and W. P. Sweetenham (1987). FACSIMILE/CHEKMAT, H015 ed. Harwell: Oxfordshire (UK).

16. Kan, C. S., J. G. Calvert, et al. "Reactive Channels of the CH_3O_2-CH_3O_2 Reaction." Journal of Physical Chemistry 84: 3411-3417 (1980).

17. Tyndall, G. S., T. J. Wallington, et al. "FTIR Product Study of the Reactions $CH_3O_2 + CH_3O_2$ and $CH_3O_2 + O_3$." Journal of Physical Chemistry A 102: 2547-2554 (1998).

18. Wantuck, P. J., R. C. Oldenborg, et al. "Removal Rate-Constant Measurements for CH_3O by O_2 Over the 298-973-K Range." J. Phys. Chem 91: 4653-4655 (1987).

Table 4.1. Experimental conditions.

Gas:	$[N_2]$	$[H_2]$	$[CH_4]$	$[F_2]$	$[O_2]$
	10^{18} cm^{-3}	10^{18} cm^{-3}	10^{17} cm^{-3}	10^{16} cm^{-3}	10^{18} cm^{-3}
concentration: (molecules cm^{-3})	0.8 - 2	0 - 1	4 - 7	3 - 4	0.9 – 1.2
Gas purity: (AirProducts)	99.9993%	99.999%		97%	99.996%

Table 4.2. Reaction mechanism.

Reaction	Reference
$F + H_2 \rightarrow HF + H$	NASA
$CH_3 + O_2 \rightarrow CH_3O_2$	NASA
$CH_3O_2 + CH_3O_2 \rightarrow$ Products [a]	NASA
$HO_2 + CH_3O_2 \rightarrow CH_3OOH + O_2$	This chapter
$HO_2 + HO_2 \rightarrow H_2O_2 + O_2$	Chapter 2
$CH_3O + HO_2 \rightarrow CH_2O + H_2O_2$	ref. b below
$H + O_2 + M \rightarrow HO_2 + M$	NASA
$H + F_2 \rightarrow HF + F$	ref. c below
$HO_2 + CH_2O \rightarrow HCO + H_2O_2$	ref. b below
$HO_2 + CH_2O \rightarrow HOCH_2O_2$	NASA
$HO_2 + HOCH_2O_2 \rightarrow$ PRODUCTS	IUPAC
$F + CH_4 \rightarrow HF + CH_3$	NASA
$F + O_2 + M \rightarrow FO_2 + M$	NASA
$FO_2 + M \rightarrow F + O_2 + M$	NASA
$FO_2 + HO_2 \rightarrow$ PRODUCTS	ref. d below
$CH_3O + CH_3O_2 \rightarrow$ PRODUCTS	ref. b below

[a] Total rate including the three branching channels listed in the text

[b] Tsang and Hampson, J. Phys. Chem. Ref. Data, v.15, p.1087, 1986

[c] Sung et al., J. Phys. Chem, v. 83, p.1007, 1979

[d] Sehested et al., Int. J. Chem. Kin., v. 29, p.673, 1997

Table 4.3. Values of k_2 and α.

T (K)	k_2 [a]	sd [a]	α	sd
296	5.0	0.5	0.16	0.03
282	5.5	0.6	0.17	0.03
267	5.6	0.6	0.16	0.03
252	7.5	0.8	0.15	0.03
239	7.7	0.8	0.13	0.03
231	8.3	0.8	0.15	0.03

[a] units in 10^{-12} cm^3 $molecule^{-1}$ s^{-1}

Table 4.4. Measurements of k_1.

T (K)	k_1 [a]	SD [a]
296	4.5	0.5
282	4.9	0.5
267	5.0	0.5
252	5.0	0.5
239	4.8	0.5
231	5.1	0.5

[a] units are 10^{-13} cm^3 molecule s^{-1}

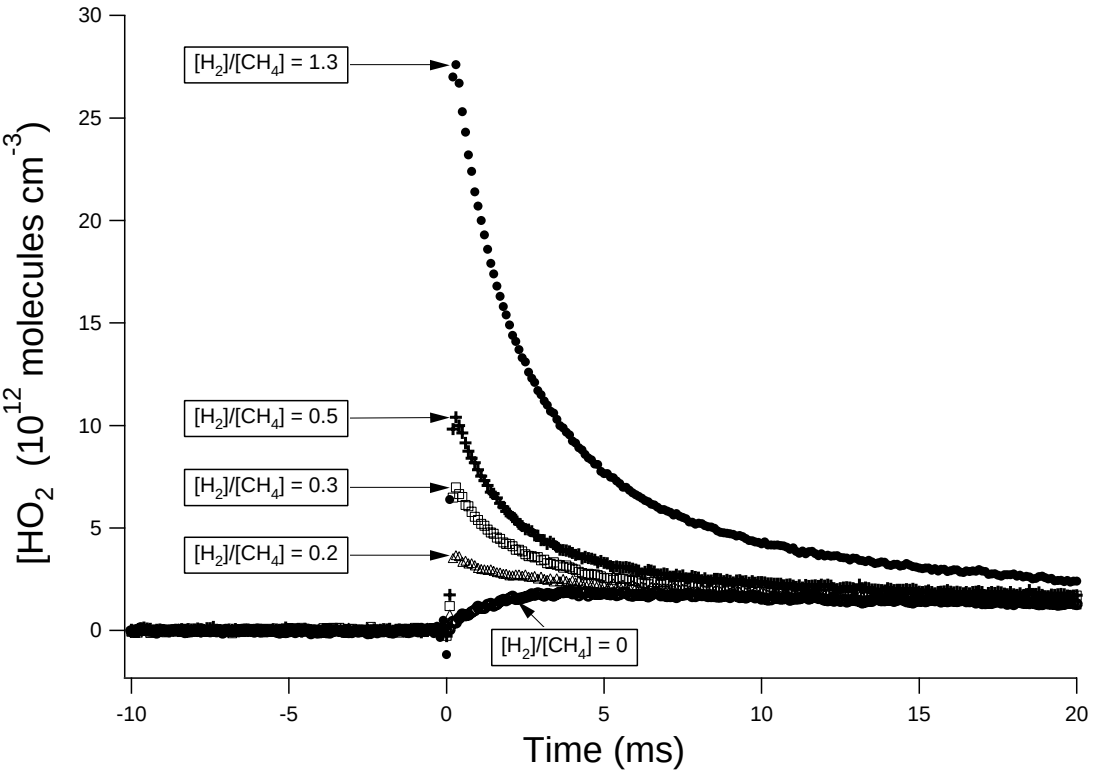

Figure 4.1.1. Time dependence of the $[HO_2]$ at different $[H_2]/[CH_4]$ at 231 K, 100 Torr. Five separate experiments are shown above for various $[H_2]/[CH_4]$. As $[H_2]/[CH_4]$ increases, $[HO_2]_o$ increases. The main processes determining the $[HO_2]$ time dependence are the $HO_2 + CH_3O_2$ reaction, which accounts for the loss of HO_2, and the formation of HO_2 due to the oxidation of products formed from the CH_3O_2 self-reaction.

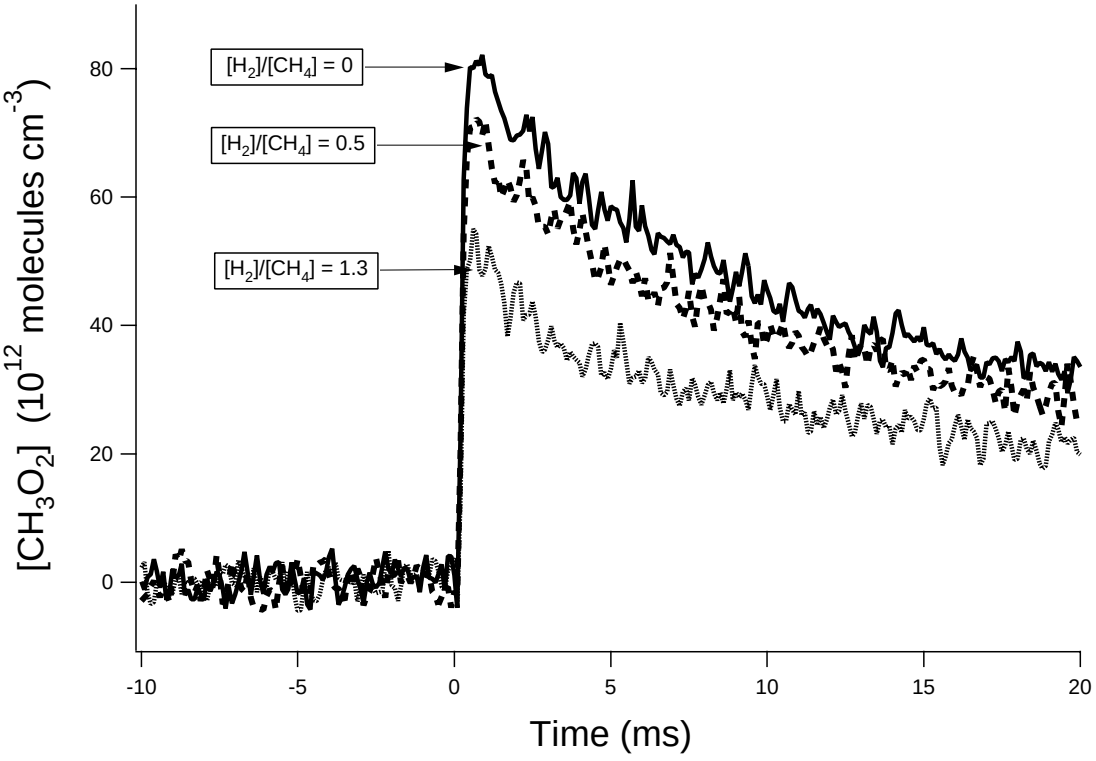

Figure 4.1.2. Time dependence of $[CH_3O_2]$ at different $[H_2]/[CH_4]$ at 231 K, 100 Torr. The signals were acquired at 250 nm. Three separate experiments are shown above for various $[H_2]/[CH_4]$. As $[H_2]/[CH_4]$ increases, $[CH_3O_2]_o$ decreases. Only three experiments are shown here, as opposed to five in Figure 1a, because of the poorer signal-to-noise of the UV data. The main processes determining the $[CH_3O_2]$ time dependence are the CH_3O_2 self-reaction and the $HO_2 + CH_3O_2$ reaction.

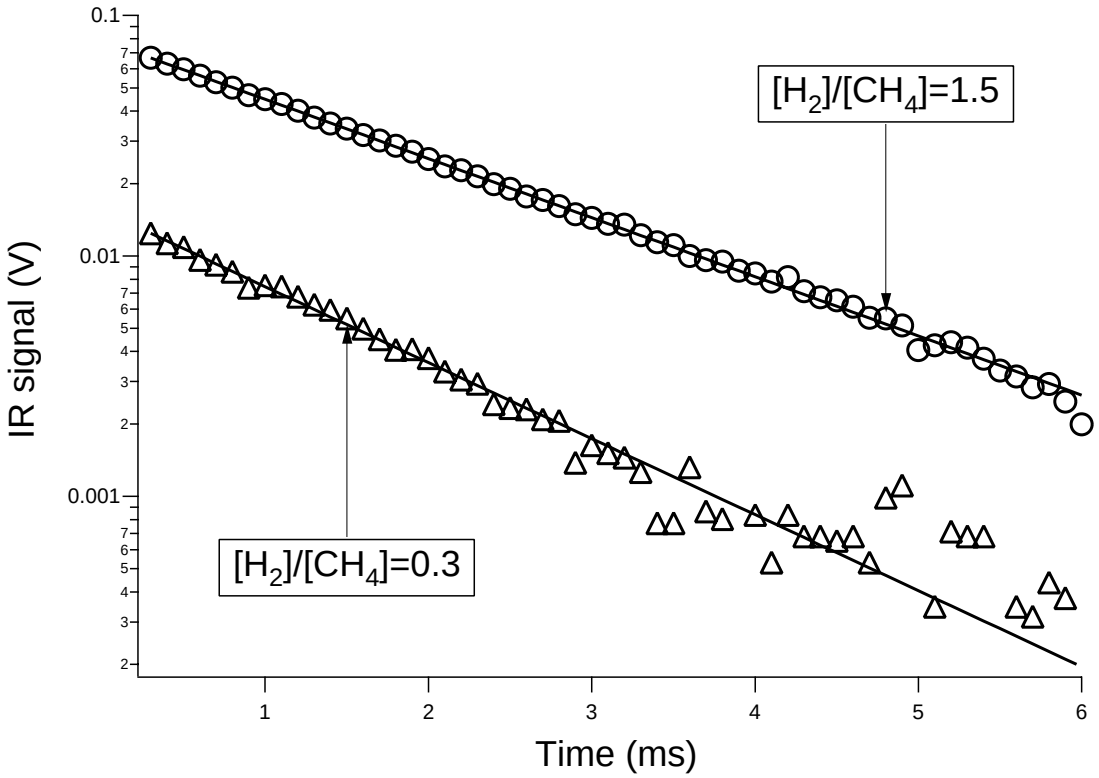

Figure 4.2. Natural log plots of data acquired at 252 K, 100 Torr in which the time dependence at $[H_2]/[CH_4]=0$ have been subtracted. The lines are fits to the data. The differences in slope are partially due to the differences in $[CH_3O_2]_0$. For conversion purposes, the scalar for converting the signal in Volts to $[HO_2]$ is 2.0×10^{14} molecules cm^{-3} V^{-1}.

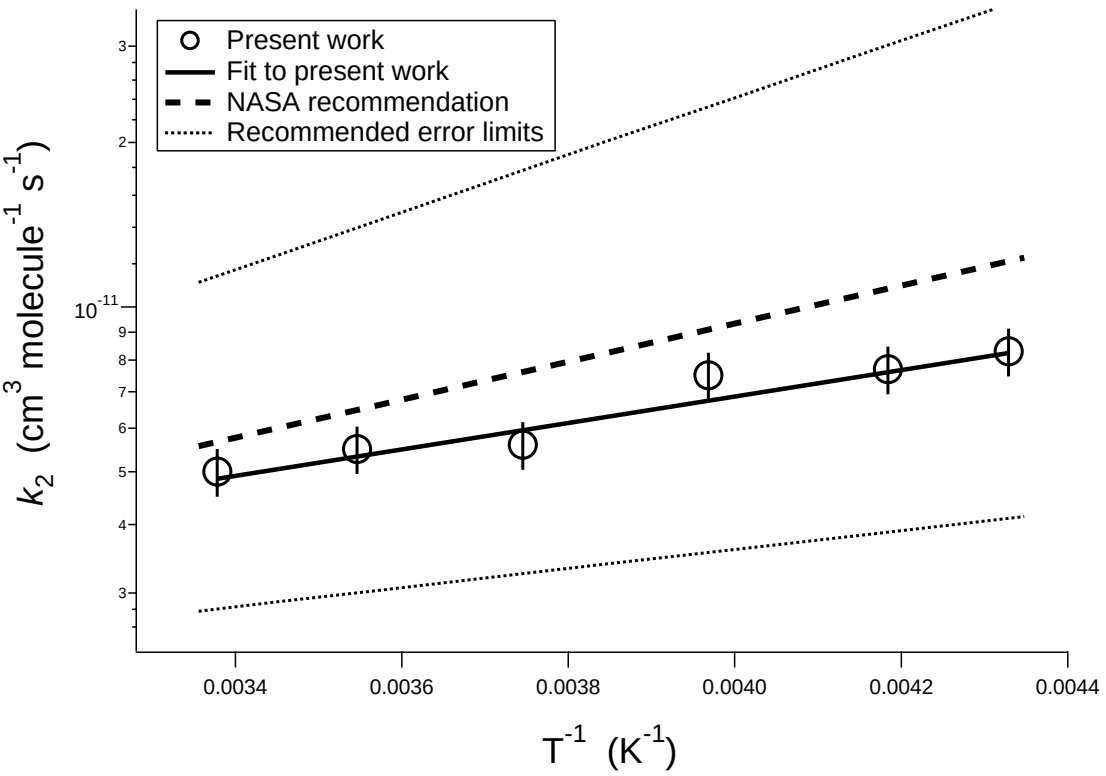

Figure 4.3. Arrhenius Plot of k_2 Versus T^{-1}. The displayed uncertainties are 1σ.

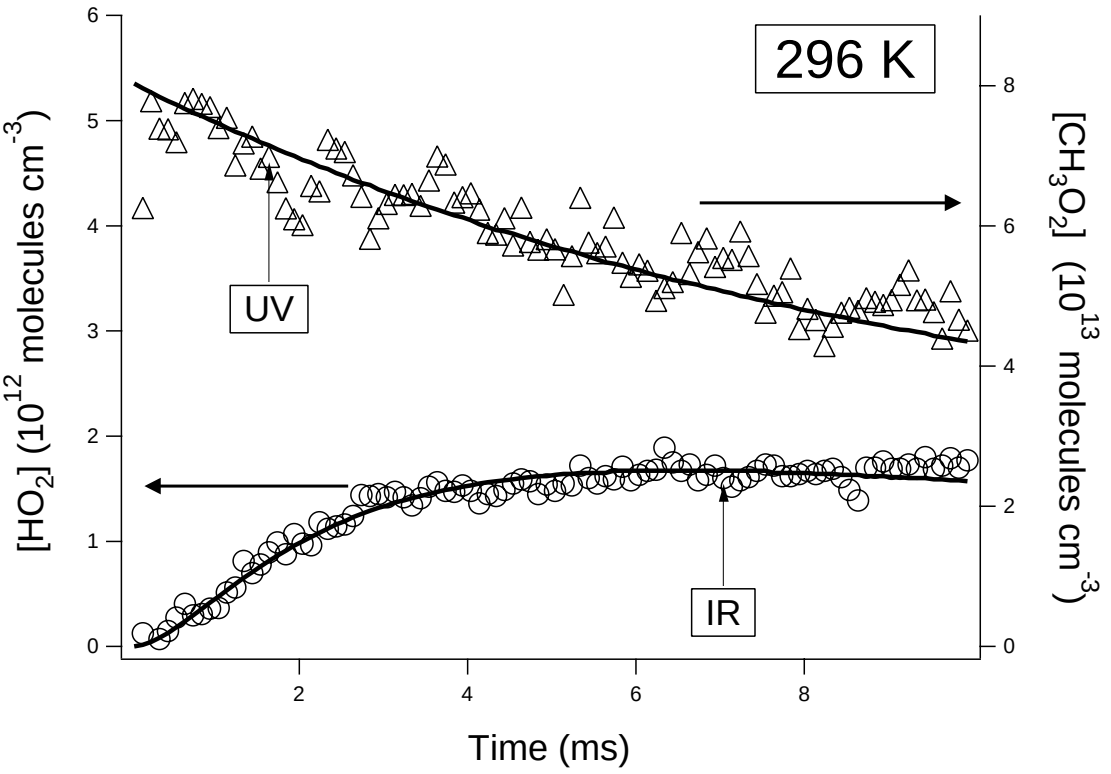

Figure 4.4.1. Fits using FACSIMILE to the time dependences of $[HO_2]$ and $[CH_3O_2]$ at 296 K.

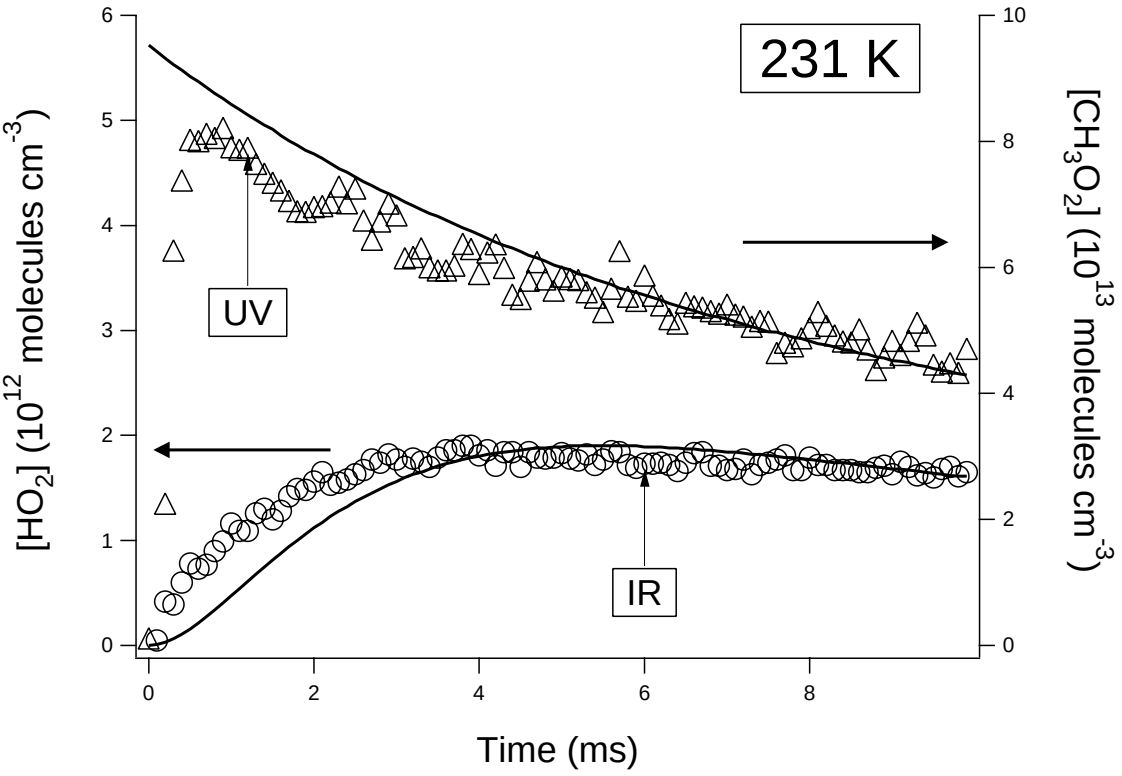

Figure 4.4.2. Fits using FACSIMILE to the time dependences of $[HO_2]$ and $[CH_3O_2]$ at 231 K.

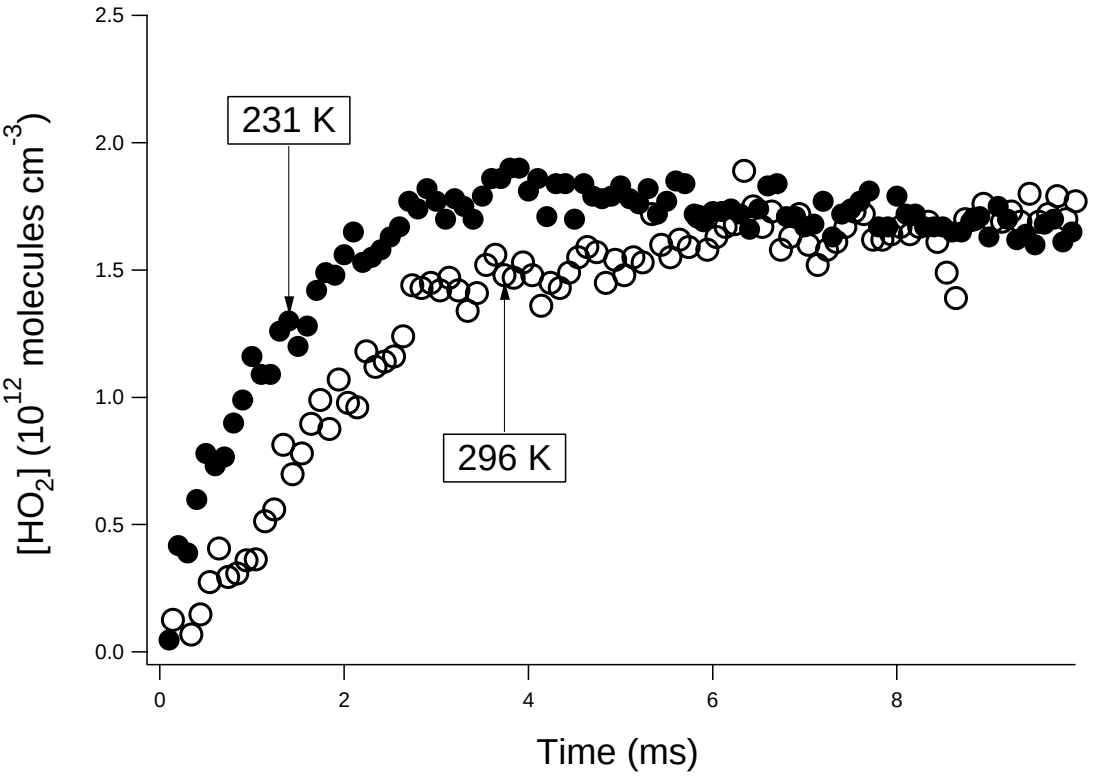

Figure 4.4.3. Comparisons of $[HO_2]$ from the CH_3O_2 self-reaction at 296 K and 231 K.

Figure 4.5. Possible reaction pathways.

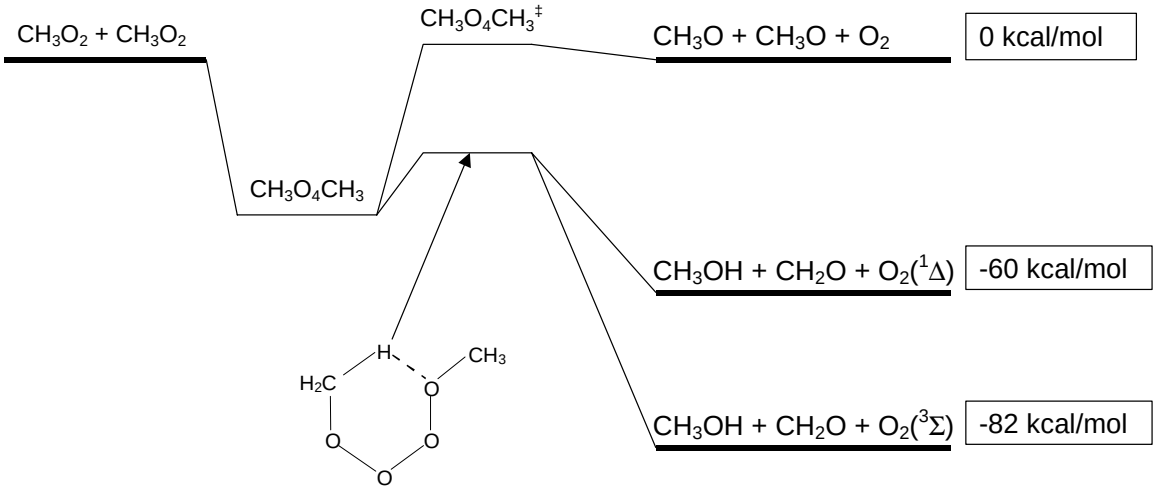

Figure 4.6. Possible pathway for formation of HO_2.

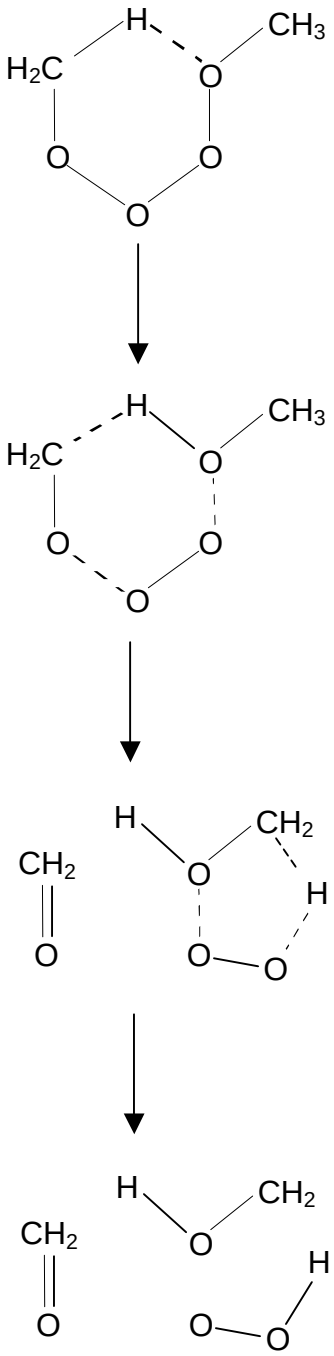

Chapter 5: Experimental Details

5.1 Introduction

The infra-red kinetic spectroscopy apparatus (IRKS) consisted of a photolysis laser, temperature controlled reaction cell connected to the gas manifold, the IR spectral probe and the UV spectral probe. This chapter explains the experimental details of the IRKS apparatus.

5.2 The Photolysis Laser

The photolysis laser was a XeCl Lambda Physik EMG-101 excimer laser that emitted at 308 nm and utilized an unstable resonator in order to decrease beam divergence. The pulse energy ranged between 50 mJ and 150 mJ. The specifications given by Lambda Physik were the following: typical power of 120 mJ, nominal pulse width of 20 ns, beam divergence of about 0.5 mrad for the unstable configuration. The excimer pulse passed through a 10 mm × 20 mm (vertical × horizontal) aperture before entering the reaction cell. At a distance of 200 cm away from the aperture, two overlapping rectangular profiles of the excimer pulse observed, a bright profile and a profile increased in size by approximately 2 mm in both directions as expected, given the specified divergence. However, the weak profile was much more divergent in the horizontal direction, approximately 2 mrad, and slightly more divergent in the vertical direction, approximately 0.8 mrad. The excimer pulse power was measured at different locations within the reaction cell. These measurements revealed that the effects of

divergence decreased the power by less than 5% the length of the reaction cell. This was assumed to have a negligible affect on experimental measurements of reaction rates.

Bright regions were scattered throughout the excimer beam profile. This phenomenon was attributed to "whispering gallery" modes formed within the resonator cavity by reflections from the capacitors. These effects were considered insignificant for kinetic studies because they were evenly scattered throughout the excimer beam profile and because they made up less than 10% of the total cross-sectional area of the excimer pulse.

The fan inside the laser cavity, which was intended to mix the gases, did not work. After consulting with workers at JPSA (Hollis, NH, ph: 603-595-7048), it was recommended that the fan not be fixed and the cooling water be removed from the pipes inside the laser to prevent corrosion problems. At the typical repetition rates employed for the kinetic experiments on the IRKS apparatus (0.3 Hz to 0.07 Hz), problems associated with the lack of gas mixing within the laser cavity were minimal – there was little change in the average power and the shot-to-shot variance in power when employing repetition rates slower than 0.3 Hz.

Typically, the voltage across the capacitors was between 20 kV and 22 kV. The possibility of increasing the output power was discussed with workers at JPSA. They suggested an upper limit of 24 kV for voltages employed. At this voltage, the pressure inside the laser cavity would have to be raised to between 3000 mbarr and 3500 mbarr to maintain proper impedance across the capacitors. However, at such voltages, the lifetime of the capacitors decreases.

5.3 The Reaction Cell and Gas Flow Manifold

The reaction cell is shown in Figure 5.1. The reaction cell was made of pyrex. It was 165 cm long and had an inner diameter of approximately 5 cm. It was held in place by two aluminum blocks. The excimer pulse and the probe beams extended the length of the reaction cell.

The two aluminum blocks that held it in place are shown in Figures 5.2 and 5.3. One end of the main cell was inserted into the "Probe input block." The other side of the reaction cell was joined onto the "Excimer input block" by two aluminum parts depicted in Figure 5.4.

The second 1-inch diameter port, denoted port 2 on Figure 5.1 was connected to the pre-cooling side-arm. The pre-cooling side-arm is shown in Figure 5.5. A pressure gauge was connected to port 3. The other two ports lead to a Welch pump, model 1396 (dual stage, 2000 L min^{-1} pumping speed). Gas from the pre-cooling side arm and the two aluminum blocks flowed towards these exit ports.

Dry nitrogen gas was flown into the two aluminum blocks through openings in conflat flanges on the side of the aluminum blocks. This purge gas was at room temperature. The purge gas served to protect the mirrors from caustic gases. The purge gas also confined the region in which there were reagent gases. The region where there was overlap between the photolysis pulse and reagent gas is denoted the photolysis volume. The photolysis volume and flow scheme are depicted in Figure 5.6.

To verify that the reagent gases were confined between the two exit ports, three different tests were employed. First, gas mixtures in which the concentration of Cl_2 was determined by flow meters were flown into the reaction cell. The pathlength was

determined using the cross section for Cl_2 given in the NASA 1997 data evaluation.[1] Second, NO_2 gas mixtures were flown into the cell and visual inspection determined whether the reagent gases were confined between the two exit ports. Third, kinetic experiments of $HO_2 + NO_2 + M$ (1) were performed in which reagent gases were flown through one of the purge ports and pumped away from the other purge port. The pathlength in this case was known because the reagent gas was confined, homogeneously, within the whole apparatus. In these studies, no purge gas was employed. Under conditions where $[HO_2]_o >> [NO_2]$, pseudo-first-order conditions are established in which k_1 is proportional to $[NO_2]$. NO_2 absorbs in the UV and its cross section has been measured previously.[2,3] Measurements of k_1 using this gas flow configuration were compared to measurements of k_1 using the gas flow configuration described above in which purge gas confined the region of the reaction cell in which there was reagent gas. The comparison indicated that the measurements of k_1 were the same if the pathlength was equivalent to the spacing between the center of the two ports, 137 cm, when the purge flow was 15% of the main (reagent) flow. An estimated error of ± 1 cm was determined from visual inspection of NO_2 absorbance and Cl_2 absorbance measurements that correlated measured pathlength with the ratio of purge flow to main flow. It was observed that a purge flow 10% of the main flow resulted in measured pathlengths of 140 cm. At a purge flow that was 20% of the main flow, the measured pathlength was about 130 cm. At 50 Torr total pressure, the purge flow needed to be between 2% and 4% of the main flow.

When not conducting experiments, it was useful to maintain a small purge flow (~ 10 sccm) of N_2 gas through both aluminum blocks to prevent caustic chemicals adsorbed in the reaction cell from attacking the mirrors when they outgassed.

Thermocouples were inserted through all four 1-inch diameter ports on the main cell. The inlets for these thermocouples were on the attachments to the main cell. The thermocouples were placed so that they did not block light from the diode laser, UV probe, or excimer laser. This forced the placement of the thermocouples towards the side of the reaction cell rather than in the middle where the probes and photolysis volume were located.

5.4 Mass Transport within the Reaction Cell

The photolysis region was centrally located within the reaction cell. While this removed possibilities of wall reactions, transport of gas to and from the photolysis region during the course of a measurement was a concern. The diffusion constant of O_2 in air at 295 K, 100 Torr is approximately 1.3 cm^2 s^{-1}.[4] Using this as an approximation for diffusion of HO_2, the effects of diffusion can be calculated using Fick's second law of diffusion

$$\frac{\partial C_i}{\partial t} = D_i \nabla^2 C_i \qquad (2)$$

where C represents the concentration of HO_2 within the reaction cell after a photolysis event. The one-dimensional solution for the boundary conditions $C(z,0) = C_o$ for $z < 0$ and $C(z,0) = 0$ for $z > 0$ is

$$C(z,t) = \frac{C_o}{2}\left[1 - erf\left(\frac{z}{\sqrt{4Dt}}\right)\right] \qquad (3)$$

From the above equation, the concentration profile, as time progresses, is depicted in Figure 5.7 for D = 1.3 cm^2 s^{-1}. Most measurements were conducted within 20 ms. For the measurements of the HO_2 self-reaction, the effects of diffusion on measured second-order-rate coefficients over the course of 40 ms were shown, by experiment, to be insignificant for sufficiently high initial HO_2 concentrations.

Diffusion was not the major source of mass transport when residence times less than 15 s were employed. The observed second-order rate coefficient measurement of the HO_2 self-reaction was dependent on the flow rate of the system as is shown in Figure 5.8 for the HO_2 self-reaction at sufficiently low concentrations of HO_2. In the figure, k_{obs} is the measured second-order rate coefficient for HO_2 self-reaction as measured by the IR source over the course of 40 ms. The rate of HO_2 loss by chemical reaction decreases as $[HO_2]_o$ decreases, and loss by mass transit out of the probe region becomes the more predominant loss mechanism for HO_2. Kinetic modeling using the FACSIMILE program[5] indicated that the loss due to mass transport could be approximated by a first-order loss process. The first-order rate of this loss process was a function of the flow rate (residence time) of the main flow. Because less than 1% of the reagent gas was removed by the pumping system over the course of 40 ms, it was believed that turbulent mixing was the cause.

To determine the effect of mass transport on the UV signal, the rate coefficient for the $C_2H_5O_2$ self-reaction was measured. The rate coefficient for the $C_2H_5O_2$ self-reaction

is relatively small at room temperature, approximately 1.1×10^{-13} cm^3 molecule^{-1} s^{-1} for the overall observed rate (which includes the contribution from the radical branching channel). The results were similar to those obtained in the IR channel for the HO_2 self-reaction.

The flow characteristics of the reaction cell were analyzed. The Reynolds number (*Re*) is an indicator of the flow characteristics of a flowing liquid or gas system. The Reynolds equation is

$$Re = \frac{4\rho}{\pi}\left(\frac{Q}{D}\right) \tag{4}$$

where ρ is the gas density (g cm^{-3}), Q is the flow rate (cm^3 s^{-1}), D is the diameter of pipe (cm), and μ is the gas viscosity (g cm^{-1} s^{-1}). $\mu = \mu_o(T/298)^{0.5}$. For the present system, the following values were used: μ_o = 1.8 g cm^{-1} s^{-1} (air), D = 5.66 cm. Table 1 lists *Re* versus Q at 100 Torr for various flow rates and two temperatures, 298 K and 231 K. As an approximation, the flow can be described as laminar when *Re* < 2000 and turbulent when *Re* > 3000. In between, it is mixed.

Table 1. Calculated Reynolds number for kinetic experiments.

flow (sccm)	Q (cm^3 s^{-1})	residence time (s) [a]	*Re*(298 K)	*Re*(231 K)
2000	250	14	50	70
4000	510	6.8	100	150
8000	1000	3.4	200	290

[a] volume of reaction cell between the two exit ports is 3470 cm^3

From the above calculations, it appeared that flow within the reaction cell was laminar. However, the above calculation was done for the gas once it was inside the main reaction cell and was flowing towards the exit ports. At the interfaces between the pre-cooling side-arm and main cell and the exit ports and the main cell, local mixing may occur. This was considered the most likely cause for the dependence of observed rate coefficients on the flow rate.

5.5 IR Detection

5.5.1 Herriott resonator

Figure 5.9 shows the Herriott mirrors. There were two different mirrors used in the cell, an input mirror and a back mirror. The input mirror had a 1/8-inch diameter input hole for the diode laser beam. The typical substrate was Pyrex. There was a bonding coat that allowed the gold coating to adhere adequately to the substrate that was applied onto the Pyrex substrate. Typically, it was either a mixture of chromium and silver or inconel. A protective layer was coated onto the gold.

Figure 5.10 shows the placement of the first three reflected spots from the diode laser beam with respect to the Herriott mirrors. The mirrors had a radius of curvature (R) of 2032 mm. The length (l) between the mirrors was approximately 1820 mm apart. This resulted in 30 passes back and forth through the photolysis region. For reference, to obtain 28 passes back and forth, the mirrors should be spaced 1786 mm apart. For 32 passes, the spacing is 1844 mm.

For the two identical mirrors, the resonator g parameter is defined as[6,7]

$$g = 1 - \frac{l}{R} \tag{5}$$

The cavity was considered a stable resonator because $0 \leq g^2 = 0.01 \leq 1$.[6,7] The dashed lines on Figure 5.10 indicate where subsequent reflections were located on each mirror. Much of the consideration of the design of the Herriott resonator had to do with the distance between adjacent reflections. The beam diameter of the diode laser was approximately 2 mm. To prevent overlap between the input hole and the adjacent reflections on either side of the input hole, it was determined that a spacing larger than 6 mm was necessary between adjacent reflections. The ellipse formed by subsequent reflections on each mirror had the following parameters: major axis radius a = 15 mm, minor axis radius b = 7.5 mm. The placement of the input hole was along the minor axis of the ellipse. In this configuration, the distance, d, between successive reflections was

$$d = \sqrt{a^2 \sin(\theta)^2 + b^2 (1 - \cos(\theta))^2} \tag{6}$$

where θ was the angle between successive reflections on an individual mirror defined as

$$\theta = \cos^{-1}(2g^2 - 1) \tag{7}.$$

The value of θ was calculated to be 24º and d was calculated to be ~ 6.1 mm using equations (5), (6), (7) and the values for l, R, a, and b given above. To obtain a condition in which reflection sizes remained constant for each reflection, the required beam

diameter on each of the mirrors needed to be approximately 1.5 mm, as calculated from the following equation[6,7]

$$\text{beam diameter} = 2\left(\frac{l\lambda}{\pi}\right)^{1/2}\left(\frac{1}{1-g}\right)^{1/4} \tag{8}$$

where λ is the wavelength of light (1.51 μm). The actual beam diameter was approximately 2 mm and slight periodic focusing and de-focusing was observed. However, none of the laser light fell off either of the mirrors. For the final transit back through the input hole, the beam diameter was nearly 2 mm.

5.5.2 The Modulation and Detection Electronics for IR channel

The modulation and detection electronics are shown in Figure 5.11. The system was made up of discrete elements. The manufacturer of each element is listed in Figure 5.11. Essentially, the system was a high-frequency lock-in detector operated on second-harmonic mode. The detection was phase-sensitive.

The system was designed to operate at a modulation frequency of 6.80 MHz because of several reasons. First, this was a frequency region where commercial phase shifters were available. Second, the de-modulated signal from the detector needed to be fully averaged by the low-pass bandwidth of the detection elements after the mixer so that the signal did not contain the initial modulation imposed on the diode laser. The SRS pre-amplifier had an inherent bandwidth of approximately 1.5 MHz at a gain of 1000, the value employed for most experiments. This was sufficient for full averaging of the de-modulated signal. The third reason the system was operated at 6.80 MHz was because the

diode laser 1/f intensity noise was minimized by detecting signals at 13.6 MHz. Under conditions where the diode laser beam went straight into a detector without passing through the Herriott cell, the dominant noise at 13.6 MHz was the quadrature sum of the detector (Johnson noise) and shot noise of the diode laser, as measured by a spectrum analyzer. In an actual experiment, there were significant contributions to the total noise of the signal from etalon effects within the Herriott resonator. The etalons were equivalent to absorptions of approximately 10^{-4}, approximately the same order of magnitude as the absorptions due to HO_2. The absorptions due to etalons were frequency dependent, and because they were non-linear in nature, the etalons translated some of the 6.80 MHz modulation into 13.6 MHz modulation. Further, the diode laser intensity output (L-I characteristic) was highly non-linear with respect to input current. This non-linearity translated diode laser intensity noise into noise at 13.6 MHz.

Pickup of electromagnetic field (EMF) noise was an issue for the diode laser channel. The shielded cable from the ILX current driver to the bias tee was observed to act as an antenna for EMF pickup. This was greatly reduced by properly grounding both ends. It was observed that the warning light outside the laboratory caused significant noise due to discharge of electricity from the brushes of the motor that turned the warning light. This problem was solved by not using the motor. A further source of noise was the charging up of the capacitor banks that provided charge to the capacitors in the excimer laser. After the excimer fired, the thyratron circuit immediately (within a tens of μs) began to re-charge the capacitor banks. This emitted an EMF with a frequency of around 60 kHz that persisted for several milliseconds. The time it persisted was dependent on the

voltage setting of the thyratron. This problem was mitigated by using the inhibit circuit of the thyratron after the trigger pulse was sent to fire the laser.

5.5.3 The HO_2 signal at 6638.2 cm^{-1}

A scan of the HO_2 signal as a function of current was obtained for the HO_2 transition that was employed for most of the experiments. The diode laser temperature was held at about 297.5 K (11.0 kΩ thermistor resistance on the plate holding the diode laser inside the diode laser housing). The current was ramped from 43 mA to 63 mA using a sawtooth voltage function on the input to the current controller. The spectrum in Figure 5.12 was obtained. The negative slope of signal versus current was to the non-linearity of the diode laser L-I characteristic as well as etalons in the diode laser beam path. The concentration of HO_2 for the scan was approximately 3×10^{13} molecules cm^{-3}.

To calibrate the spectral position of the HO_2 signal near 6638.2 cm^{-1}, spectral scans of water were conducted. Water was flown into the reaction cell at 295 K and 10 Torr total pressure. The concentration of water in the cell was approximately 3×10^{16} molecules cm^{-3}. The pathlength of the IR beam through the region with water was approximately 137 cm × 30 passes = 4100 cm. As depicted in Figure 5.13, two water transitions were observed. Using the HITRAN database,[8] the two water lines were positions were established. Line A was at 6636.85 cm^{-1} and Line B was at 6636.60 cm^{-1}. The spectral distance between the peaks was 0.25 cm^{-1}, and the current distance was 11 mA. The current tuning was thus approximately -0.023 cm^{-1}/mA. At 8.2 kΩ, the frequency of emission at 49.60 mA was estimated to be 6634.2 cm^{-1} (from measurements made the same day). The temperature tuning was approximately 1 cm^{-1}/kΩ. Line A was

approximately at 49.60 mA. The line used for HO_2 studies was at 33.80 mA, 11.7 kΩ. The combined temperature and current tuning places the HO_2 line at ~ 6638.0 ± 0.5 cm^{-1}. The uncertainty is based on the observation that diode laser current tuning was non-linear. It was more efficient at lower currents (i.e., the frequency response was greater per unit current at). Also, the temperature tuning has been observed to be slightly non-linear, becoming more efficient at lower temperatures (higher values of thermistor resistance).

Through private conversation, I obtained an emission spectrum of HO_2 between 6570.0 cm^{-1} and 6700.0 cm^{-1}. The work was done by E. Fink and D. Ramsay. To date, it has not been published. It was done at the same time work was done on the emission spectrum of the $A^2A' \rightarrow X^2A''$ band of HO_2 which was published in 1997 by these same workers.[9] I have not been authorized to publish this work so I will only document my observation based on their work. There is a strong emission line at 6638.20 ± 0.05 cm^{-1} given an arbitrary strength of approximately 1.9. There are also an emission lines at 6638.10 ± 0.05 cm^{-1} and 6638.35 ± 0.05 cm^{-1} with strengths of approximately 1. None of the lines are labeled and could be due to O_2 emission. Tuckett et al.[10] also studied the emission spectrum of HO_2 in this spectral region and assigned many of the transitions. Based on the above considerations, the maximum HO_2 signal has been associated with a frequency of 6638.2 cm^{-1} and the assignment $^qQ_2$. A supporting piece of evidence is that the observed HO_2 transition strengths diminished as the frequency of the diode laser was increased from the HO_2 transition at 6625.80 cm^{-1}, a transition given the nominal assignment $^qP_0(10)$.[10] It was assumed that this was due to the decrease in the degeneracy as $J \rightarrow 0$. Despite this trend, the line at 6638.2 cm^{-1} was observed to be stronger than all

the previous lines. These observations support the theory that the transition is a Q-branch band-head.

5.5.4 Comparisons of linestrengths between $Q_{1,2}(12)_{0\text{-}1}$ $A^2A' \leftarrow X^2A''$ and $^qP_0(10)$ $2\nu_1$ transitions

For kinetic studies of the $HO_2 + NO_2 + M$ reaction, described in Chapter 1, two lasers were used, one that emitted at 1.43 microns and one that emitted at 1.51 microns. The former investigated $A^2A' \leftarrow X^2A''$ electronic transitions, the latter investigated ro-vibrational transitions associated with the O-H overtone. The $Q_{1,2}(12)_{0\text{-}1}$ $A^2A' \leftarrow X^2A''$ transition occurs[9] at 6998.403 cm^{-1} and the $^qP_0(10)$ O-H stretch overtone transition ($2\nu_1$) occurs[10] at 6625.80 cm^{-1}. Both assignments were made using emission measurements.[9] Linestrengths for $A^2A' \leftarrow X^2A''$ transitions have not been published to date. Linestrength measurements for only one transition of $2\nu_1$ has been published. This was for the $^qP_0(10)$ line and its value was reported to be 2.4×10^{-21} cm^2 $molecule^{-1}$ cm^{-1}.[11]

Daniel B. Oh and I conducted measurements in 1999 to compare linestrengths between the overtone and electronic transition. At that time, Dr. Oh was a researcher at Southwest Sciences Inc. in Santa Fe, NM. The apparatus used was a discharge flow apparatus. A microwave discharge dissociated O_2 into O atoms that then reacted with allyl alcohol.

$$CH_2{=}CH\text{-}CH_2OH + O \longrightarrow HO_2 + CH_2{=}CH\text{-}CH_2 \qquad (9)$$

After mixing O atoms with allyl alcohol, the gas mixture (mostly He) flowed into an analysis region, which consisted of two diode laser beams folded by two Herriott mirrors, making 64 passes through the gas mixture. The pressure of the cell was approximately 200 mTorr. The temperature was 293 K.

Figure 5.14 are the direct absorption signals acquired with the JPL diode laser and the SWS diode laser. To abstract a linestrength, proper accounting of the drift of JPL and SWS diode laser had to be taken account as well as the convolution of the linewidth of the lasers and the spectral transition. The measurements were conducted below 100 mTorr where most of the broadening was due to Doppler broadening. The correction for convolution was approximate 5% (the JPL diode laser had a linewidth of approximately 40 MHz). The correction for diode laser drift, which results in a lower cross-section at line center and a larger FWHM was determined from previous scans of water using the JPL diode laser. This correction was to enhance the overall linestrength by a factor of 1.12. Using these corrections and the ratio of the strengths of the $^{q}P_0(10)$ transition measured with the SWS laser, the linestrength of the $Q_{1,2}(12)_{0\text{-}1}$ $A^2A' \leftarrow X^2A''$ was calculated to be $(2.0 \pm 0.5) \times 10^{-21}$ cm^2 molecule^{-1} cm^{-1}.

5.6 UV Measurements

Figure 5.15 shows the UV spectrum for HO_2, CH_3O_2, $C_2H_5O_2$. The HO_2 transition near 202 nm and the CH_3O_2 transition centered near 238 nm have been determined, from ab initio calculations, to be due to $2^2A'' \leftarrow X^2A''$ electronic transitions,[12,13] assuming a C_s symmetry for CH_3O_2. For the $C_2H_5O_2$ transition centered near 240 nm, a similar transition is excited. For the ground state, the unpaired e^- is in an Π-type orbital. The

calculated dipole moment functions of X^2A'' and $2^2A''$ are a factor of 2 different, thus there should be a strong transition due to the accompanying charge transfer.[12,13]

5.7 References

1. DeMore, W. B., S. P. Sander, et al. (1997). Chemical Kinetics and Photochemical Data for Use in Stratospheric Modeling, Evaluation Number 12. Pasadena, CA, Jet Propulsion Laboratory, California Institute of Technology.
2. Bass, A. M., A. E. Ledford, et al. J. Res. NBS 80A: 143-166 (1976).
3. Davidson, J. A., C. A. Cantrell, et al. J. Geophys. Res. 93: 7105-7112 (1988).
4. C., R. R. and T. K. Sherwood (1958). The Properties of Gases and Liquids, Chap. 8. New York, McGraw-Hill Book Company.
5. Curtis, A. R. and W. P. Sweetenham (1987). FACSIMILE/CHEKMAT, H015 ed. Harwell: Oxfordshire (UK).
6. Siegman, A. E. (1971). An Introduction to Lasers and Masers. New York, McGraw-Hill.
7. Trutna, W. and R. Byer "Multiple-pass Raman gain cell." Appl. Optics 19: 301-312 (1980).
8. Rothman, L. S., C. P. Rinsland, et al. "The HITRAN Molecular Spectroscopic Database and HAWKS (HITRAN Atmospheric Workstation): 1996 Edition." Journal of Quantitative Spectroscopy & Radiative Transfer 60: 665-710 (1998).
9. Fink, E. H. and D. A. Ramsay J. Mol. Spectrosc. 185: 304-324 (1997).

10. Tuckett, R. P., P. A. Freedman, et al. "The Emission Bands of HO_2 between 1.43 and 1.51 Microns." Molecular Physics 37: 379-401 (1979).

11. Taatjes, C. A. and D. B. Oh Appl. Optics 36: 5817-5821 (1997).

12. Shih, S.-K., S. D. Peyerimhoff, et al. "MRD-CI Calculations for the Vertical Electronic Spectrum of the Hydroperoxyl Radical." Chemical Physics 28: 299-304 (1978).

13. Jafri, J. A. and D. H. Phillips "Ground and Lower Excited States of Methyl Peroxy, CH_3O_2, Radical: A Computational Investigation." J. Am. Chem. Soc. 112: 2586-2590 (1990).

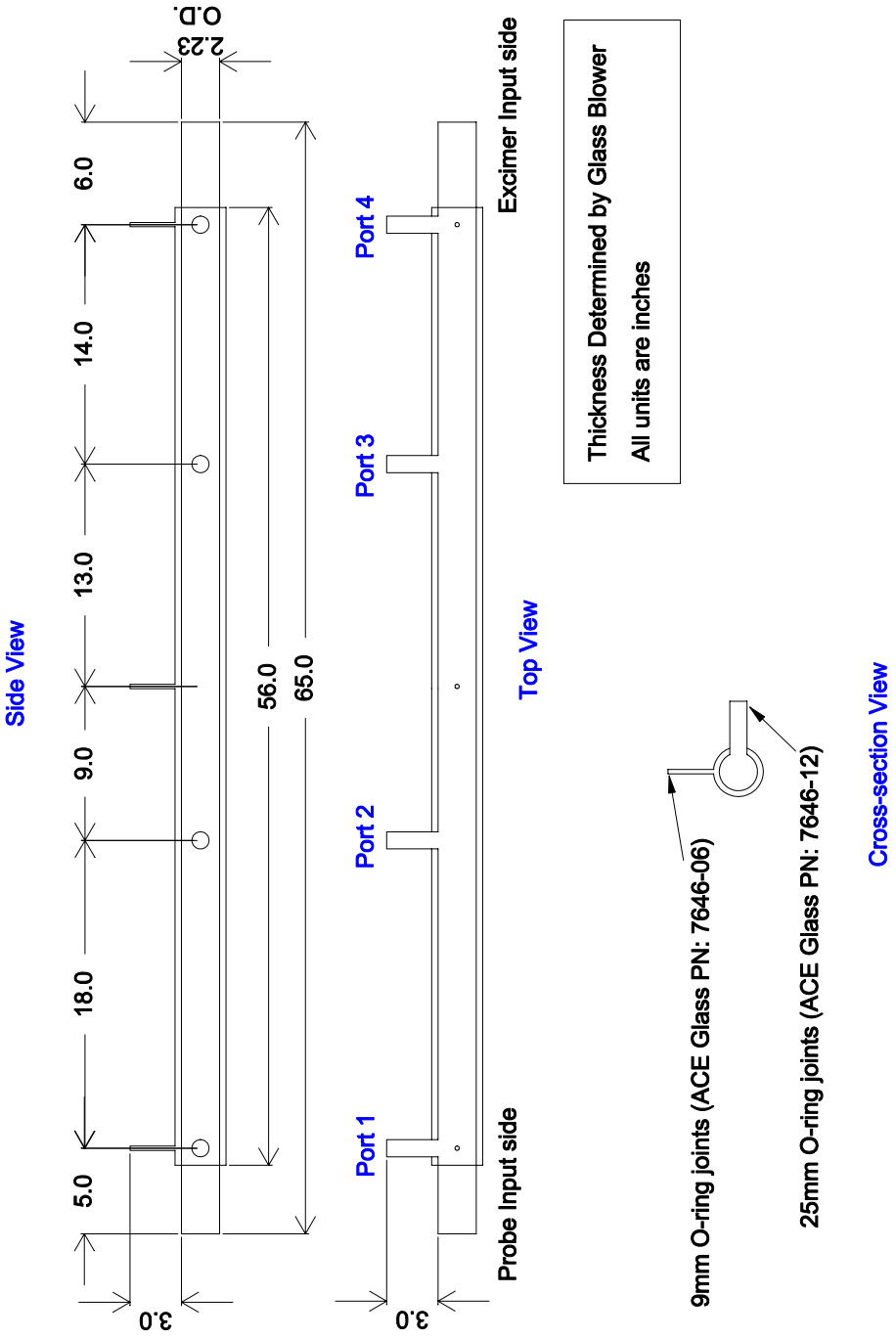

Figure 5.1. Main reaction cell

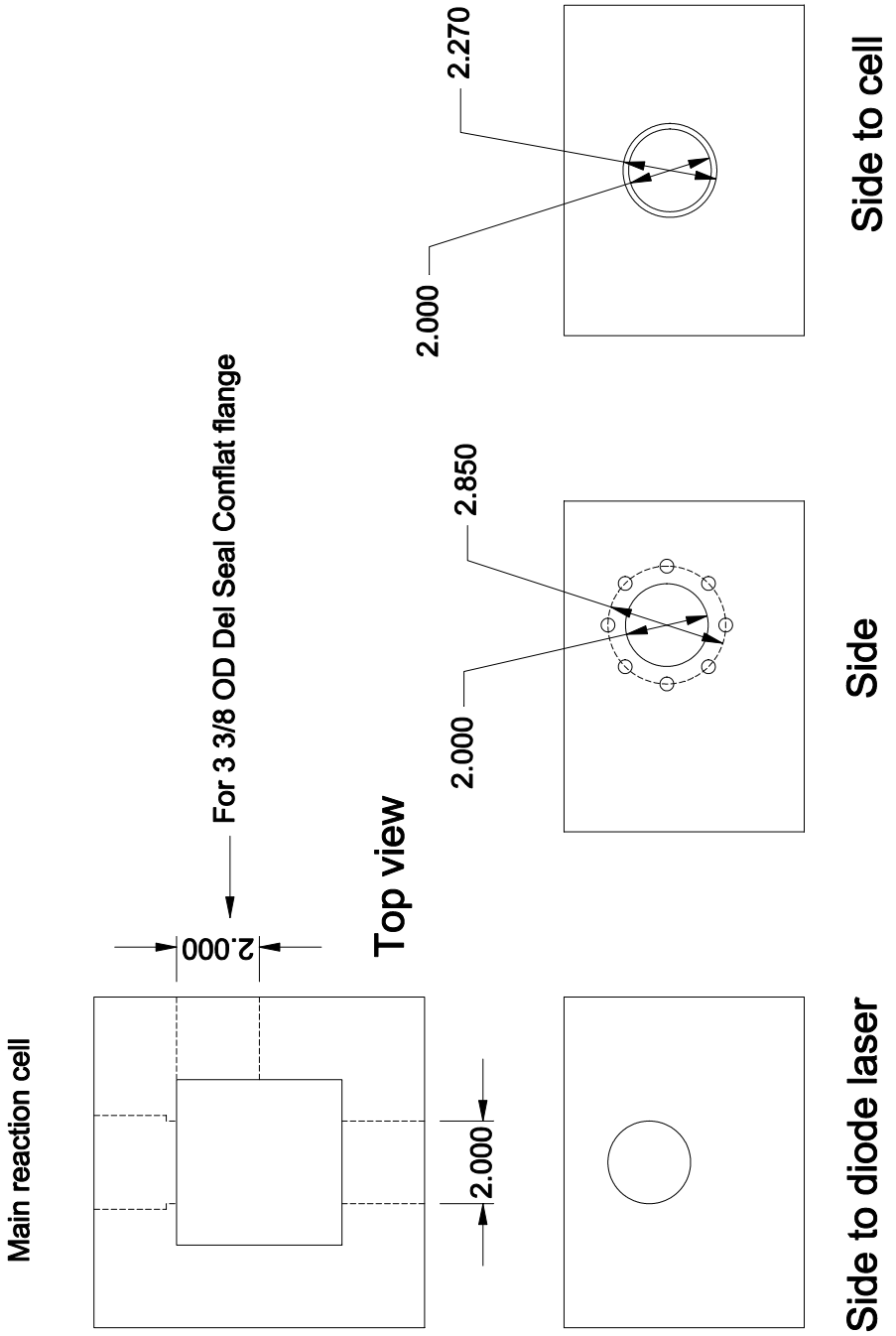

Figure 5.2. Probe input and aluminum block

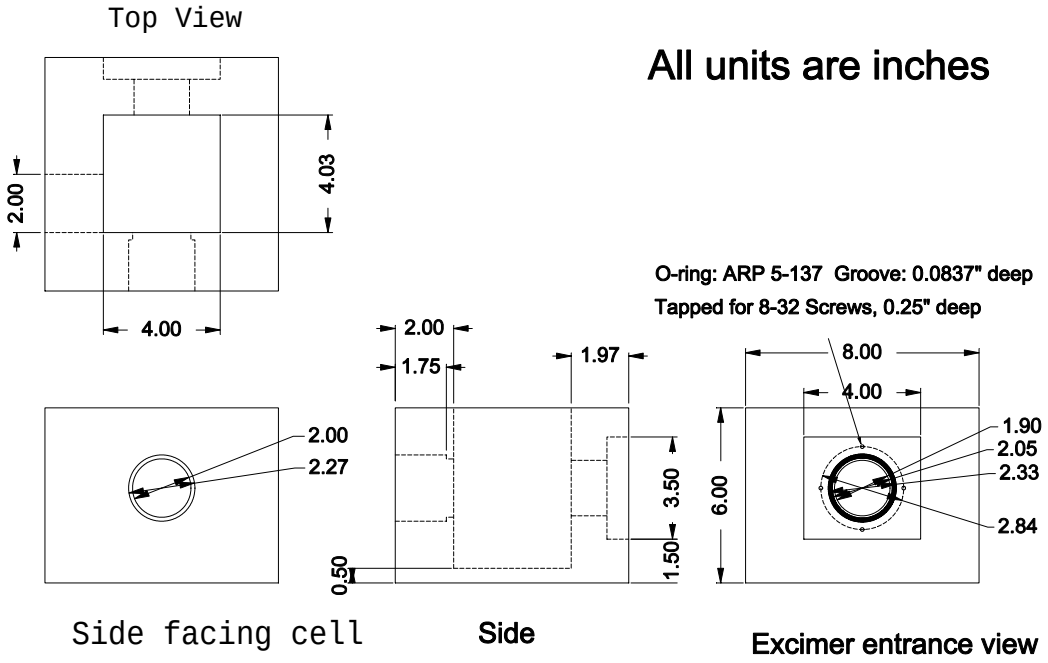

Figure 5.3. Excimer input and aluminum block.

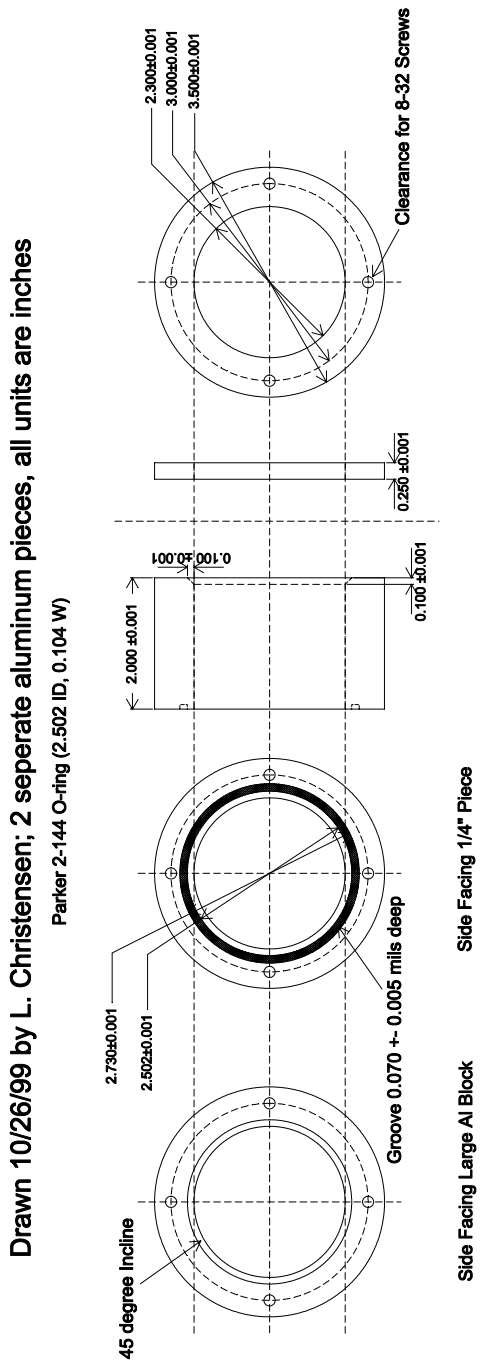

Figure 5.4. Joiner for reaction cell and excimer input aluminum block.

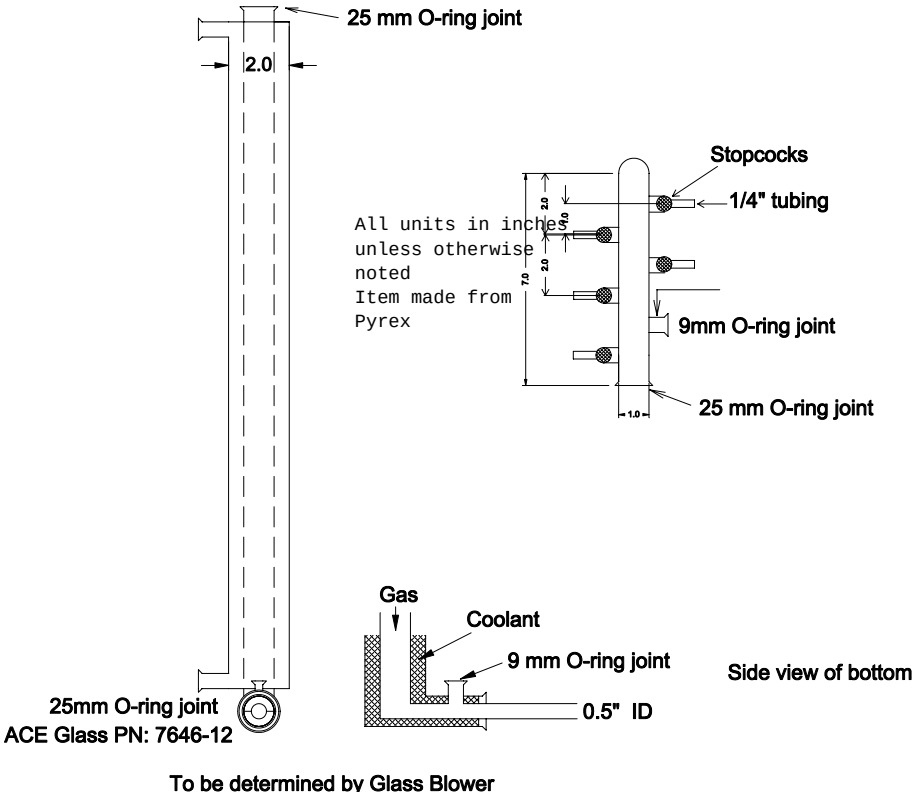

Figure 5.5. Pre-cooling cell.

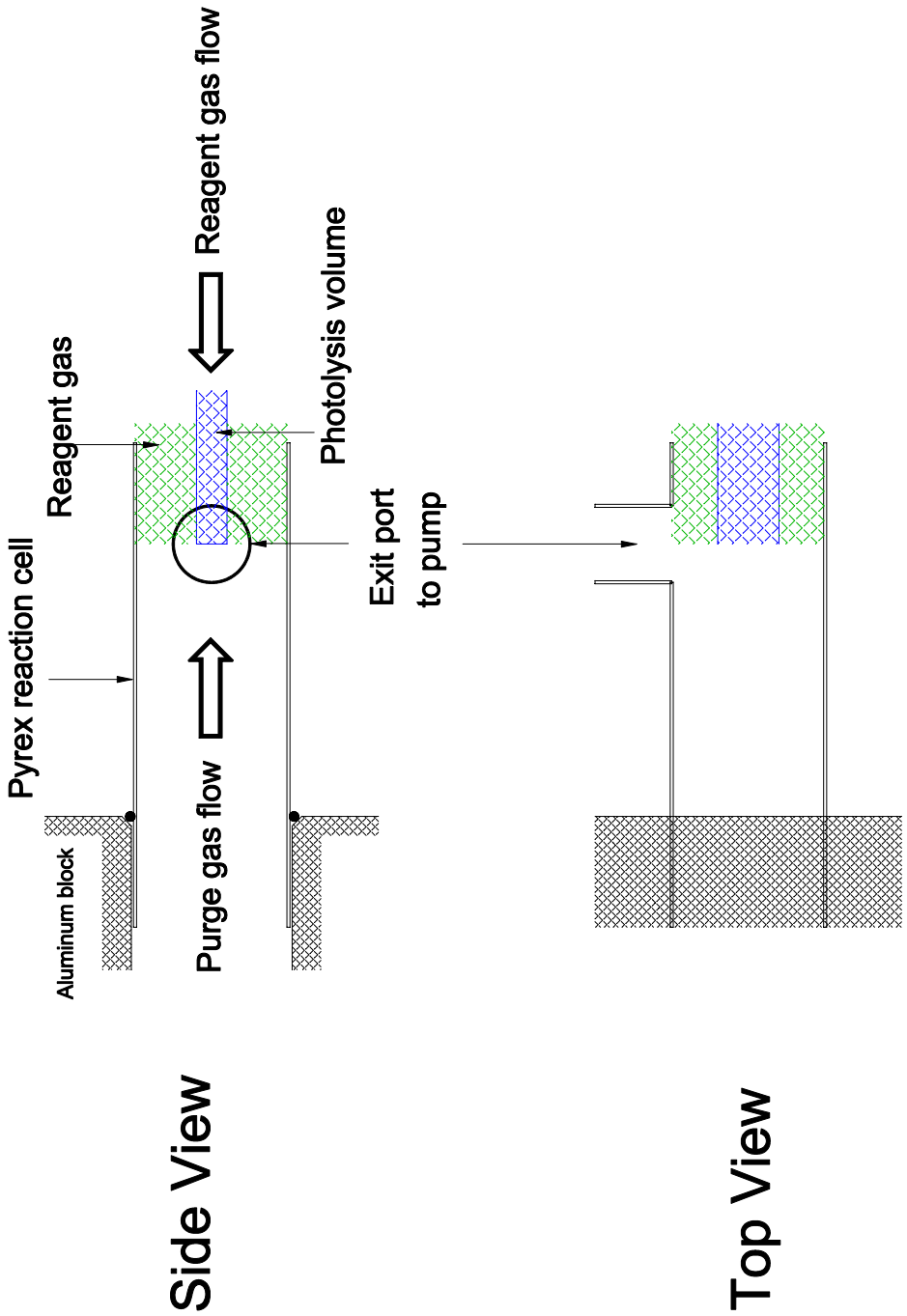

Figure 5.6. Photolysis volume.

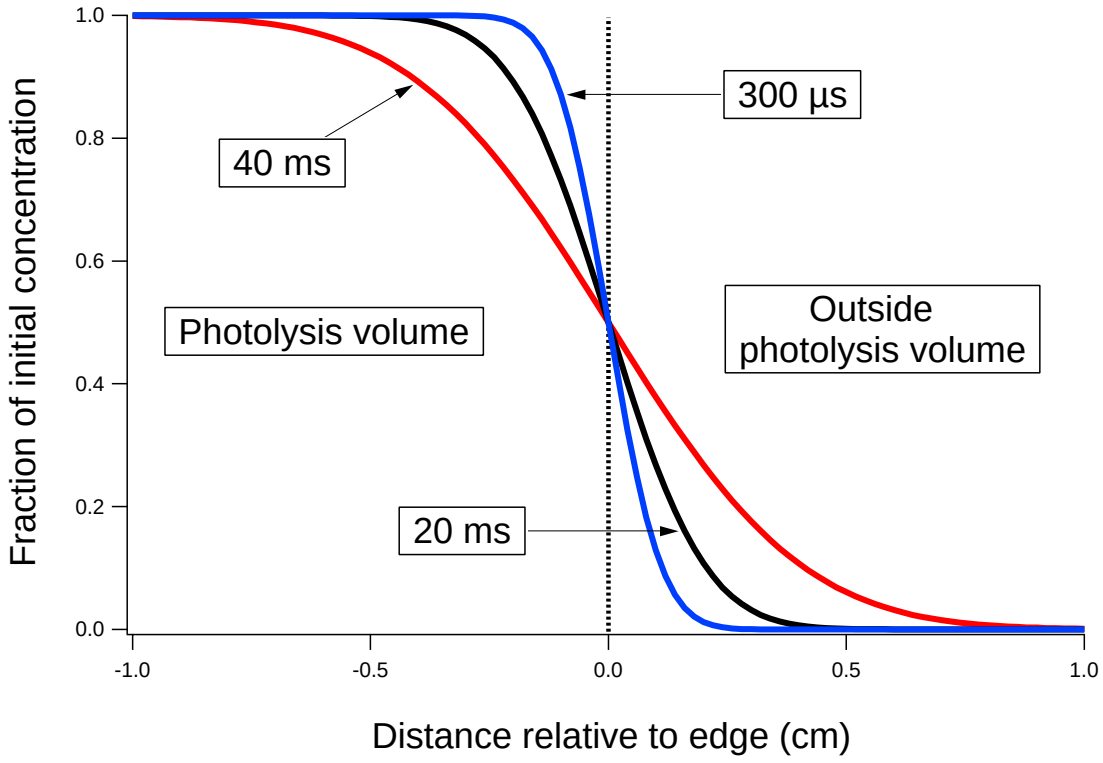

Figure 5.7. Calculated HO_2 concentration profiles at 100 Torr, 298 K at different times after the photolysis event.

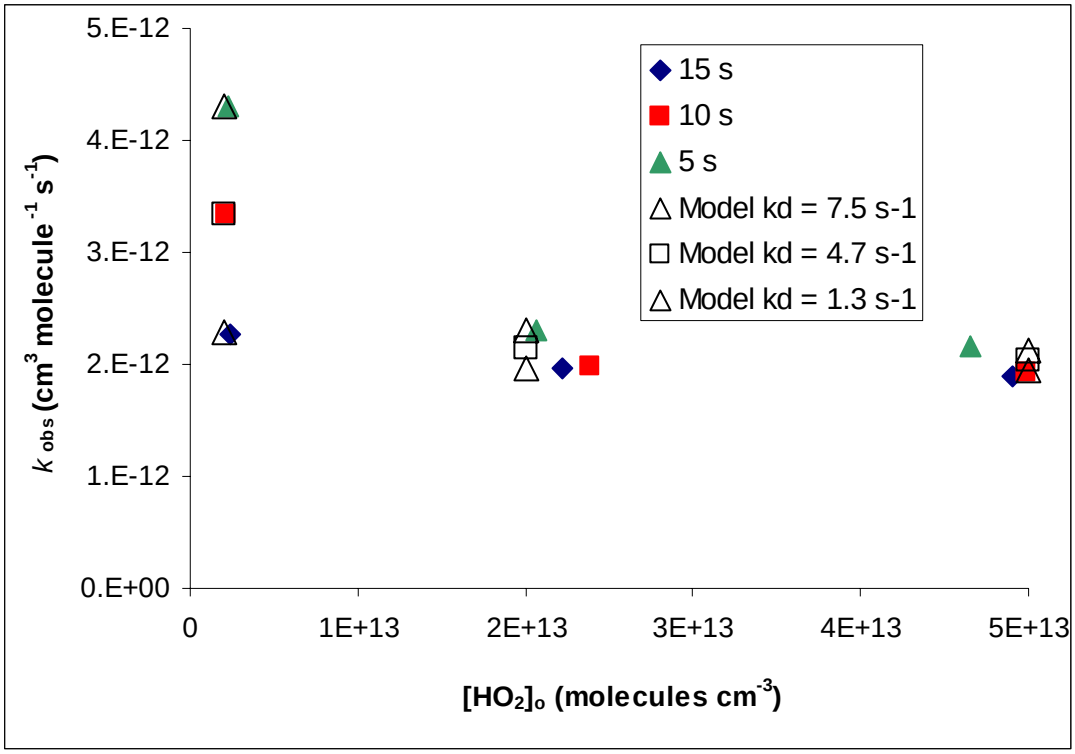

Figure 5.8. Modeled mass transport rates. The filled-in symbols are rate measurements of the HO_2 + HO_2 reaction using the IR source at 100 Torr, 298 K. The open symbols are modeled rates for the HO_2 + HO_2 system with an added first-order loss process for HO_2 described by a k_d. The figure demonstrates that at high residence times, the measured rate of HO_2 + HO_2 remains constant – i.e. other processes affecting the rate are diminished in comparison with the bimolecular loss by reaction.

Figure 5.9. Herriott mirrors.

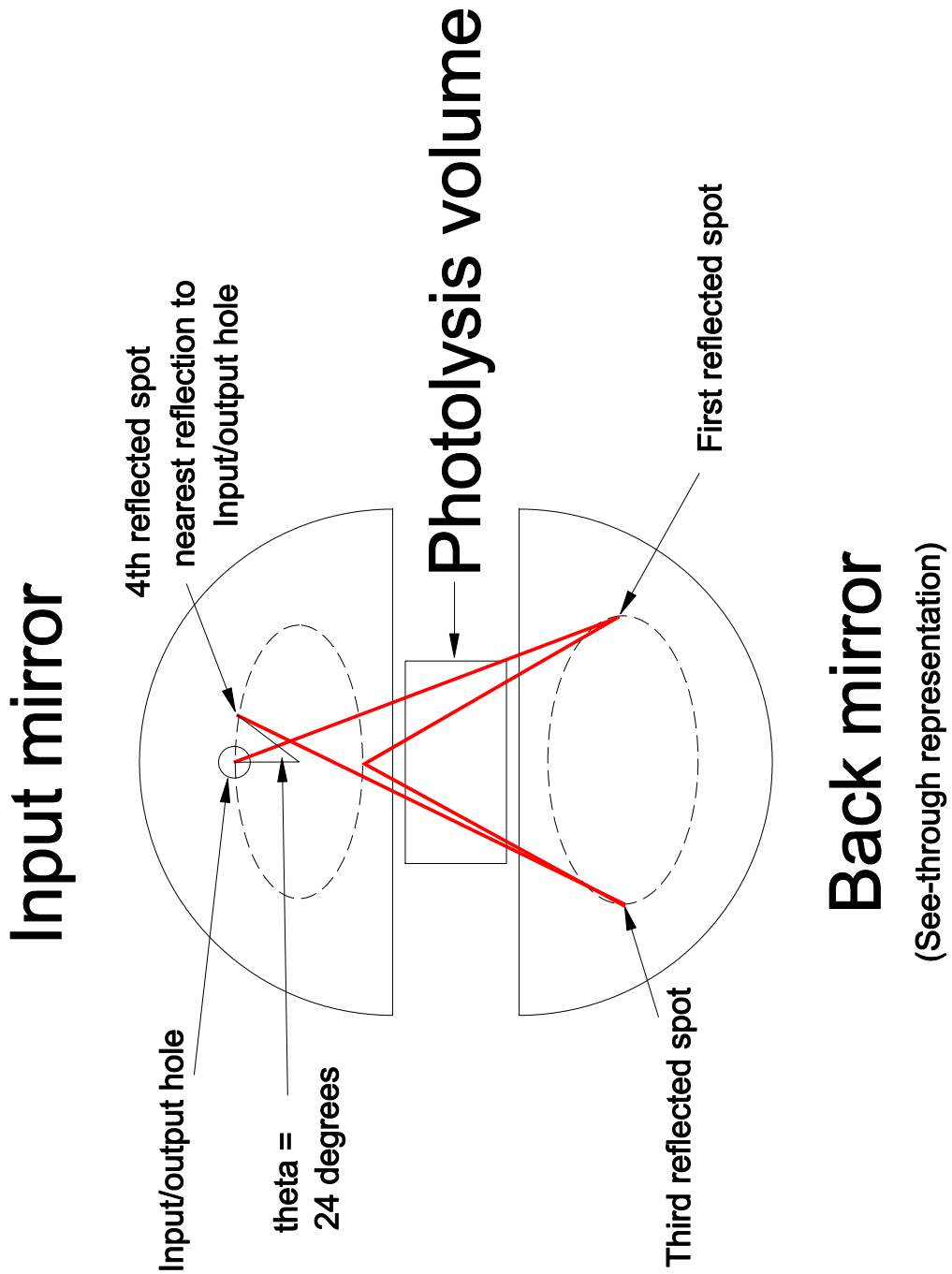

Figure 5.10. Diode laser beam placement on Herriott mirrors.

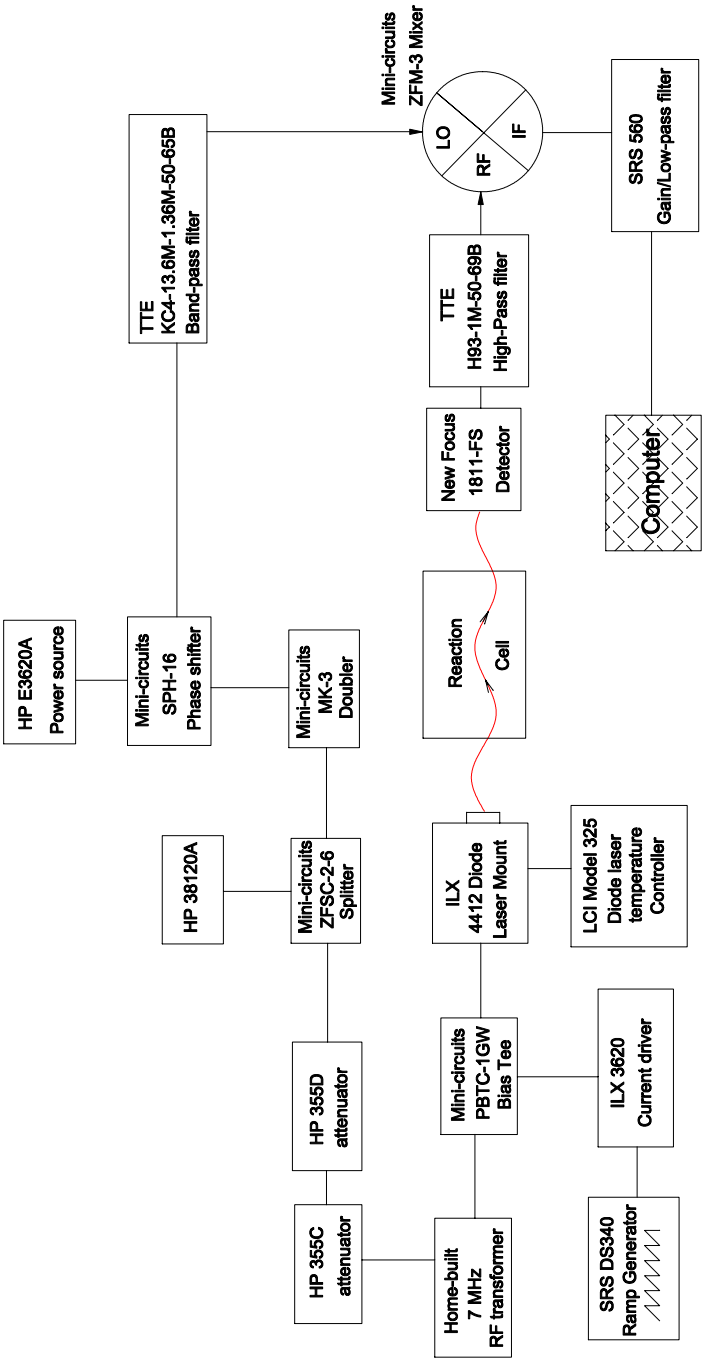

Figure 5.11. Modulation and detection electronics.

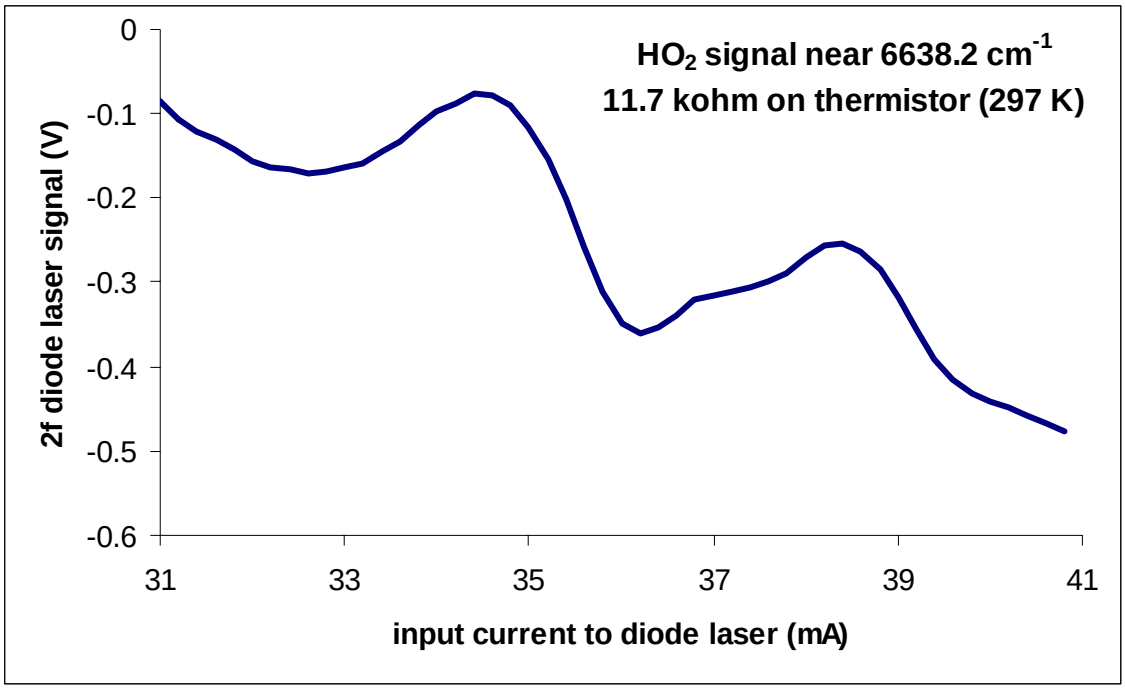

Figure 5.12. HO_2 spectrum near 6638.2 cm^{-1} as a function of input current to the diode laser. The signal is the 2f signal. The span of 10 mA corresponds to about 0.23 cm^{-1} in frequency.

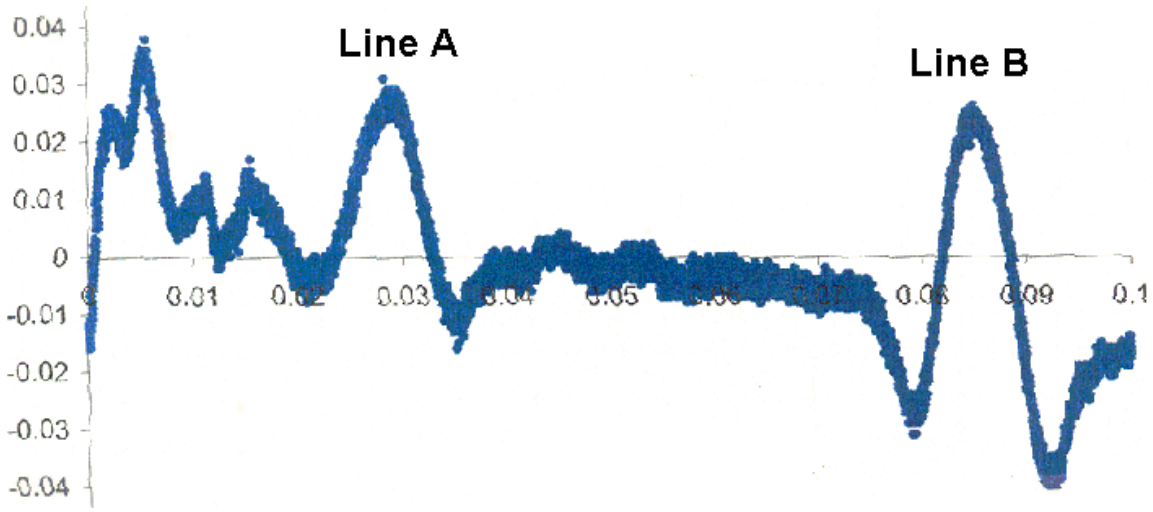

Figure 5.13. Two water lines acquired by a DFB diode laser acquired from the Microdevices laboratory at JPL. Line A is at 6636.85 cm^{-1} and Line B is at 6636.60 cm^{-1}. The scan was acquired by varying the current from 43 mA (0 on the x-axis) to 53 mA (0.1 on the x-axis) at a thermistor setting of 11.0 kΩ. The y-axis is in units of arbitrary signal in volts.

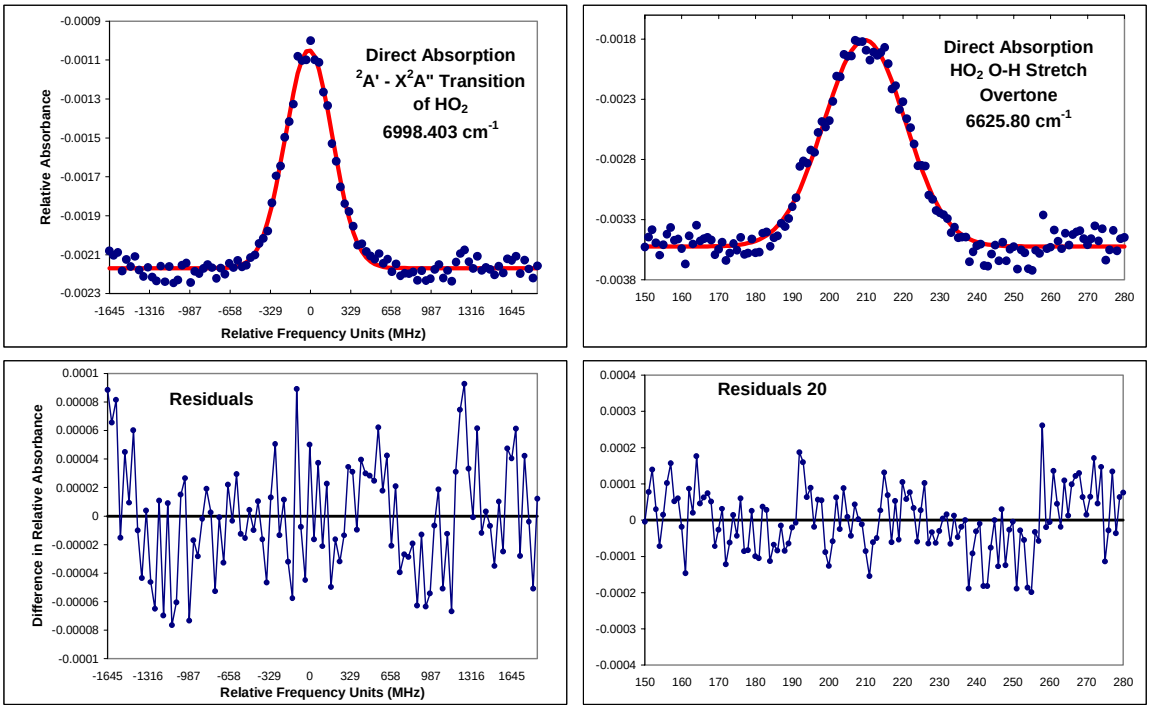

Figure 5.14. Comparison of HO_2 $1^2A' \leftarrow X^2A''$ and O-H overtone transitions.

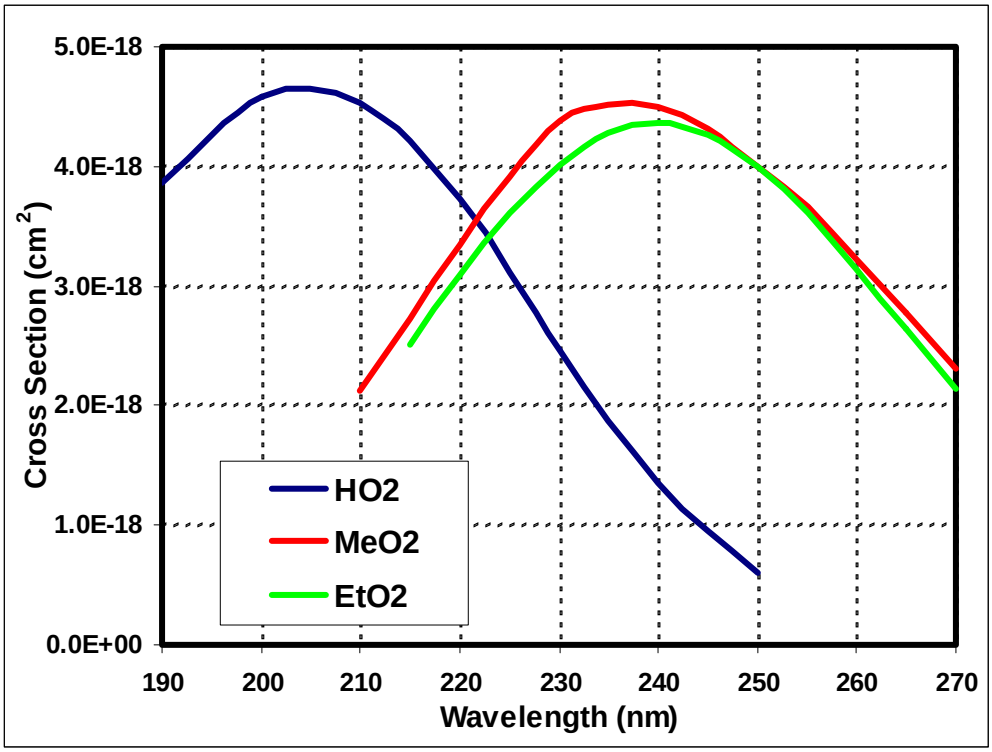

Figure 5.15. UV spectrum of HO_2, CH_3O_2, and $C_2H_5O_2$.